Towards a search for the electric dipole moment of the muon at the Fermilab Muon $g-2$ experiment

Samuel Paul Grant

Submitted in fulfilment of the requirements
for the award of the degree of
Doctor of Philosophy

Department of Physics and Astronomy
University College London

December 9, 2022

Declaration

I, Samuel Paul Grant, confirm that the work presented in this thesis is my own. Where information has been derived from other sources, I confirm that this has been indicated in the text.

Acknowledgements

Firstly, I would like to express my gratitude to my supervisor, Gavin Hesketh, without whom none of this would have been possible. Your unwavering encouragement and calmness in face of challenging problems, technical or otherwise, has made you a pleasure to work for – thank you!

The Fermilab Muon $g-2$ experiment is not only an impressive magnet and a large pile of interesting data, but a community of wonderful people which I have been honoured to be a part of. I would ideally thank every one of you, but I must offer particular thanks to Rebecca Chislett, Joe Price, and James Mott. The three of you are a genuine inspiration to me, not only because of your remarkable physics skills, but also because of your patience and generosity. Your support and guidance meant – and continues to mean – a great deal to me, and I sincerely doubt that this thesis would exist without it. I am also deeply grateful to Mark Lancaster, Chris Polly, Brendan Casey, Saskia Charity, Alex Keshavarzi, Sophie Middleton, and Nick Kinnaird for making me feel so welcome at Fermilab during my two years there, even after we were locked down due to COVID-19. I am also deeply indebted to every member, past and present, of the outstanding Europa ω_a, tracker, and EDM groups, for their invaluable advice and support through the years. Special thanks also to Simon Corrodi, for your great help with the radial magnetic field measurements, as well as to Fred Gray, for giving me the opportunity to step out out of the office and into the lab to work on the fibre harps with you, and to Rene Fatemi, for lending me your expertise with simulation on more than one occasion. I would also like to express my sincere gratitude to Barry King, who sadly passed away during my postgraduate studies, for giving me my first opportunity to work on $g-2$ as an undergraduate summer student at Liverpool.

This acknowledgements section would be woefully incomplete with thanking my close friends and fellow UCL $g-2$ students, Gleb Lukicov and Dominika Vasilkova, for many interesting discussions, for the camaraderie, and for this making this experience so much fun. Thanks also to Cathal Sweeney, for preserving my sanity during the several months we were locked down together, as well as to Aidan Kelly, Raif Bin Norisam, Simeon Bash,

Will Quinn, and Jamie McGowan, for being such great friends to me throughout my time at UCL. To Vincenzo Monachello, thank you for bringing so much optimism and hilarity into office D25, especially during those turbulent final weeks while writing this thesis.

Finally, to my family: Mum, Dad, James, Joey, Izzy, Momo, and Grandpa. Thank you all for the unconditional love and support, without which I would certainly not be where I am today, and for listening to me ramble about physics for the past decade or so. To Savanah, you are a source of endless inspiration to me; thank you for making these past few years the best of my life, and for reminding me what all this is supposed to be about.

Abstract

The Fermilab Muon $g-2$ experiment aims to measure the anomalous magnetic moment of the muon, a_μ, to a precision of 140 parts-per-billion (ppb), and conduct a world-leading search for the electric dipole moment (EDM) of the muon, d_μ. At the time of writing, the combination of the first result for a_μ from Fermilab, published in 2021 [1], and the final result from the Muon $g-2$ experiment at Brookhaven National Laboratory (BNL) [2], presents a 4.2σ tension with the Standard Model (SM) prediction [3]. If this discrepancy persists, it will require a resolution in the form of the discovery of new physics beyond the SM (BSM). Alongside this, any observation of a muon EDM would constitute a discovery of new physics outright, and would provide a new source of charge-parity (CP) violation from outside the SM. Fermilab aims to improve upon the current muon EDM upper limit of $|d_\mu| < 1.8 \times 10^{-19}\, e \cdot \text{cm}$ (95% C.L.), set by BNL [4], by at least an order of magnitude.

In this thesis, a blinded search for d_μ in E989 Run-1 is presented. In support of this, the development and execution of a novel technique for measuring the radial component of the storage ring magnetic field to a precision of ≤ 1 parts-per-million (ppm) is described. The work ensures that the radial magnetic field, which can mimic a signal from a non-vanishing muon EDM, does not present a limiting source of systematic uncertainty in the overall search for d_μ at E989. The production and analysis of large-scale Monte Carlo simulation is also outlined, which is essential for the characterisation of sources of systematic uncertainty in the EDM search, and, critically, the observed dilution of the EDM signal. Finally, blinded results from the search for d_μ using data from straw tracker detectors in the four datasets comprising E989 Run-1 are presented, with an estimated total uncertainty of $\pm 1.04 \times 10^{-19}\, e \cdot \text{cm}$. This uncertainty is used to derive the expected upper limit on the muon EDM of $|d_\mu| < 2.0 \times 10^{-19}\, e \cdot \text{cm}$ (95% C.L.), which improves upon the upper limit from the equivalent traceback detector analysis performed at the BNL Muon $g-2$ experiment [4].

Contents

List of Figures

List of Tables

Chapter 1

Introduction

As a theory of elementary particles and their interactions, the Standard Model of particle physics (SM) is both extremely impressive and notably incomplete. While capable of extremely precise predictions, which have been extensively verified by experimental observation, it does not account for a number of phenomena such as dark matter, dark energy, particle mass differences, gravity, and the abundance of matter over antimatter in the universe. These omissions in the theory must ultimately be resolved with the discovery of new physics beyond the SM (BSM).

Searches for new physics employ various strategies: some looking for evidence of exotic processes or particles by use of high energy colliders or low background experiments, and others relying on high precision measurements of SM predicted parameters, looking for evidence of new physics at the point where theory and experiment diverge.

The Fermilab Muon $g-2$ experiment (E989) takes the latter approach, aiming to measure the anomalous magnetic moment of the muon, a_μ, to a precision of 140 parts-per-billion (ppb). At the time of writing, the combination of first result for a_μ from E989 [1], with a precision of 460 ppb, and the final result of previous iteration of the Muon $g-2$ experiment at Brookhaven National Laboratory (BNL E821) [2] presents 4.2σ tension with the SM [3]. If the discrepancy persists beyond 5σ, and if no inaccuracies are discovered in the theoretical calculation of a_μ, then new physics will be required to explain the anomaly. Additionally, E989 will conduct a world-leading search for the electric dipole moment (EDM) of the muon, d_μ, projecting to improve on the current experimental upper limit of $|d_\mu| < 1.8\times10^{-19}$ e·cm, set by E821 [4], by at least an order of magnitude. While the SM predicts a muon EDM of $\mathcal{O}(10^{-36})$ e·cm[1], which is far beyond the reach of current experimental sensitivity, a large muon EDM is allowed by certain

[1]This estimate is based on the upper limit for the electron EDM [5], and is discussed further in Chapter 1 Section 2.

well-motivated extensions to the SM; some of which can simultaneously accommodate the observed discrepancy in a_μ. If a muon EDM is discovered at E989, it would signal a BSM source of combined charge conjugation and parity (CP) violation in the lepton sector, which may be critical in explaining the matter-antimatter asymmetry of the universe.

This thesis will focus on efforts towards a muon EDM search at E989. In this introductory chapter, the theory of lepton dipole moments will be outlined and the muon EDM search will be motivated in the context of new physics models. Chapter 2 will introduce the essential physics principles of the experiment, while Chapter 3 will discuss the specific techniques and hardware that comprise E989. Chapter 4 will detail the development and execution of a novel technique for measuring the radial component of the E989 storage ring magnetic field to a precision of < 1 parts-per-million (ppm). This work ensures that the radial magnetic field, which can mimic an EDM signal, does not present a limiting source of systematic uncertainty in search for d_μ in Run-1, and beyond. Chapter 5 describes the large-scale simulation efforts which are essential to the characterisation of sources of systematic uncertainty in the measurement, and, critically, the momentum dependent dilution of the EDM signal. In Chapter 6, a blinded search for d_μ in Run-1 using data from straw tracker detectors is presented, including an assessment of sources of systematic uncertainty, which is concluded with an estimation of a preliminary upper limit on $|d_\mu|$. Finally, Chapter 7 concludes this thesis, providing a summary of results and discussion as to the outlook of the search for a muon EDM at Fermilab.

1 The anomalous magnetic moment of the muon, a_μ

The magnetic dipole moment, $\vec{\mu}$, of a subatomic particle with mass m, charge e, and spin $\vec{s}$ is described by the expression

$$\vec{\mu} = g\left(\frac{Qe}{2m}\right)\vec{s}, \tag{1.1}$$

where $Q = \pm 1$. g is the g-factor: a dimensionless quantity which characterises the strength of the coupling between the magnetic moment and the spin. Classically, where the spin angular momentum may be compared to the total orbital angular momentum of a rotating distribution of charges, the g-factor would be equal to one [6]. For particles

on the subatomic scale, however, it has been extensively proven that $g \neq 1$. The origin of this deviation arises in part from relativistic effects, which may be reconciled with quantum mechanics via the Dirac equation: giving the prediction that $g = 2$ for spin 1/2 particles (fermions). While this prediction holds at leading order, the interaction between the fermion and an external magnetic field includes contributions to the g-factor from higher order virtual particle loop diagrams at the fermion-photon vertex, known as radiative corrections, so that $g \neq 2$. In the case of the electron and the muon, g is slightly greater than 2. This deviation is the anomalous magnetic moment, a, which is defined as

$$a = \frac{g-2}{2}, \tag{1.2}$$

allowing Equation 1.1 to rewritten in the form

$$\vec{\mu} = (1+a)\frac{e\hbar}{2m}, \tag{1.3}$$

separating the magnetic moment into two parts: the Dirac moment and the *anomaly* (the Pauli moment) [7].

The anomalous magnetic moment of the electron, a_e, was first measured by Kusch and Foley in 1947 [8], with the leading order quantum electrodynamics (QED) radiative correction being famously calculated by Swinger soon after [9]. Since then, a_e has become the most precisely predicted [10] and measured [11] physical quantity ever: a stringent test of QED and a resounding success for the SM.

The anomalous magnetic moment of the muon, a_μ, while not as suitable for probing QED as the electron, presents a far more promising avenue in the search for new physics [12]. Quantitatively, the reason for this is that a particle with mass M, where $M >> m$ (with m being the elementary fermion mass), makes a contribution to the anomaly a on

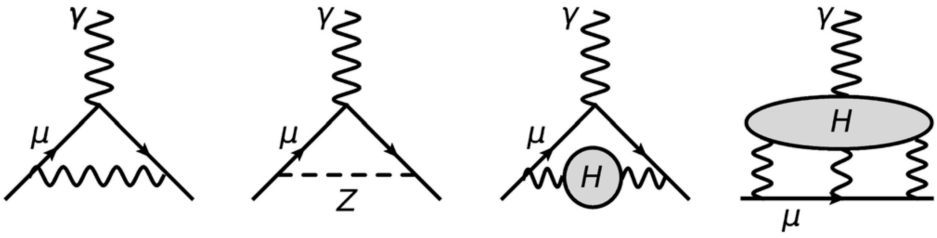

Figure 1.1: SM contributions to a_μ. From left to right: leading order QED (Swinger), leading order electroweak, hadronic vacuum polarisation, and hadronic light-by-light scattering. Image reproduced from [1].

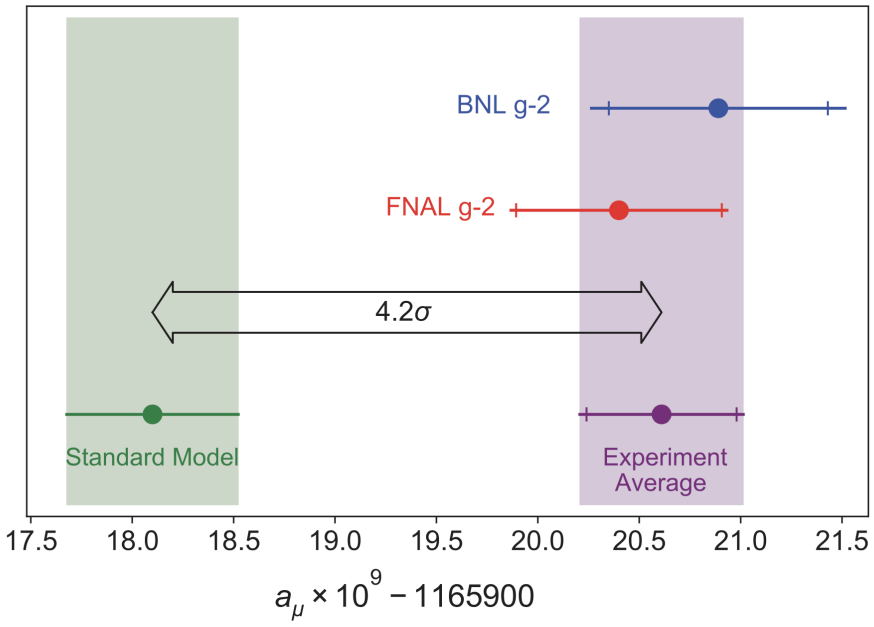

Figure 1.2: Current experimental values of a_μ from Brookhaven E821 and Fermilab E989, as well as the experimental average, compared with the SM prediction. Image reproduced from [1].

the scale of

$$\delta a \sim C \cdot \left(\frac{m}{M}\right)^2, \tag{1.4}$$

where $C = \delta m/m$, δm being the new physics contribution to the fermion mass, which is highly dependent on the details of the new physics model in question (discussed further in Chapter 1 Section 3). Given that the muon is ~ 200 times more massive than the electron, this implies that the muon magnetic anomaly is $\sim 4 \times 10^4$ times more sensitive to the higher mass-energy scales where BSM physics is most likely to reside.

Within the SM, a_μ is composed of contributions from all sectors: the electromagnetic (QED), electroweak (EW), and hadronic (had), so that

$$a_\mu^{\mathrm{SM}} = a_\mu^{\mathrm{QED}} + a_\mu^{\mathrm{EW}} + a_\mu^{\mathrm{had}}, \tag{1.5}$$

where Feynman diagrams summarising the classes of SM contributions to a_μ are shown in Figure 1.1. If there exists a discrepancy between experiment and the SM, $\Delta a_\mu = a_\mu^{\mathrm{Exp}} - a_\mu^{\mathrm{SM}}$, then a fourth (BSM) contribution must included, so that

$$a_\mu^{\mathrm{Exp}} = a_\mu^{\mathrm{SM}} + a_\mu^{\mathrm{BSM}}. \tag{1.6}$$

At present, the SM prediction for the muon magnetic anomaly is $a_\mu^{\mathrm{SM}} = (116591810 \pm 43) \times 10^{-11}$ [3], while the current combined experimental value, which includes input from the first result from Fermilab E989 [1] and the final result from Brookhaven E821 [2], is $a_\mu^{\mathrm{Exp}} = (116592061 \pm 41) \times 10^{-11}$; so that the discrepancy stands at $\Delta a_\mu = (251 \pm 59) \times 10^{-11}$. As illustrated in Figure 1.2, this presents a 4.2σ tension between theory and experiment which, while not yet conclusive, indicates that new physics extensions to the SM may be required to account for the anomaly. The topic of new physics is expanded upon in Section 3.

2 The electric dipole moment of the muon, d_μ

In addition to a magnetic dipole moment, Dirac's theory predicts that subatomic particles may also possess an electric dipole moment (EDM), $\vec{d}$ [7]. Classically, an EDM is a measure of the permanent polarisation of a system of electric charges. For the simplest case of two opposing point charges, $\pm q$, separated by a distance $\vec{r}$, the EDM is given by $\vec{d} = q\vec{r}$. More generally, $\vec{d}$ is equal to the integral of the charge density, $\rho(\vec{r})$, over the charge volume, so that

$$\vec{d} = \int \vec{r}\rho(\vec{r})\, d^3r, \tag{1.7}$$

where $\vec{r}$ has it's origin at the centre of charge distribution [6]. In the case of elementary fermions, which are treated as point-particles of no spatial extent within the SM, the classical argument would follow that such particles must have a EDM of zero. In quantum mechanics, however, a non-vanishing EDM is allowed by polarisation of the vacuum field around the particle. Like the magnetic moment, the EDM must be directed along the spin vector, the only vector-like property associated with an elementary particle, and is expressed in form similar to Equation 1.1:

$$\vec{d} = \eta \left(\frac{Qe}{2mc} \right) \vec{s}, \tag{1.8}$$

where c is the speed of light in a vacuum. η is a dimensionless quantity, analogous to the magnetic g-factor, which describes the strength of the coupling between the EDM and the spin. η may be expressed in terms of fundamental constants, so that

$$\eta = \frac{4dmc}{Qe\hbar}, \tag{1.9}$$

where d assumes the convention

$$\vec{d} = d \cdot \hat{s}. \tag{1.10}$$

Unlike its magnetic counterpart, the EDM of the muon and other subatomic particles breaks the symmetries parity, P, where $(t, x) \rightarrow (t, -x)$, and time reversal, T, where $(t, x) \rightarrow (-t, x)$. This P and T symmetry breaking arises from the differing properties of axial vectors and polar vectors under P and T transformations [7]. Axial vectors, which describe a rotation about an axis, are even under P (they do not change sign) and polar vectors are odd. Magnetic field vectors, $\vec{B}$, are axial and electric field vectors, $\vec{E}$, are polar. Spin is an axial vector, making the dipole moments $\vec{\mu}$ and $\vec{d}$ axial vectors by Equations 1.1 and 1.8. The third symmetry is charge conjugation, C, where $q \rightarrow -q$, under which all quantities mentioned here are odd. The combined symmetry CPT is expected to hold, so it follows that if $\vec{B}$ is even under P then it must be odd under T. The same logic applies for $\vec{E}$ and $\vec{s}$. The various transformation properties of $\vec{E}$, $\vec{B}$, $\vec{\mu}$, and $\vec{d}$, are given in Table 1.1.

	$\vec{E}$	$\vec{B}$	$\vec{\mu}$ or $\vec{d}$
C	$-$	$-$	$-$
P	$-$	$+$	$+$
T	$+$	$-$	$-$

Table 1.1: The transformation properties of $\vec{E}$, $\vec{B}$, $\vec{\mu}$, and $\vec{d}$.

The external magnetic and electric fields, $\vec{B}$ and $\vec{E}$ may be related to their corresponding dipole moments by the interaction Hamiltonian

$$\mathcal{H} = -\vec{\mu} \cdot \vec{B} - \vec{d} \cdot \vec{E}, \tag{1.11}$$

from which it can be deduced that the magnetic part of the interaction is CP even and the electric part, the EDM, is CP odd. This means that subatomic particle EDMs violate CP symmetry: one part of Sakharov's criteria [13] for a universe dominated by matter rather than antimatter.

Clearly, particle EDMs provide a unique insight into fundamental physics, and have been considered as such since Purcell and Ramsey first proposed a search for the neutron EDM as a means of testing P symmetry in 1950 [14]. Since then, however, no permanent EDM has been observed for any particle or atom [15]. Moreover, the SM predictions for

Particle	EDM upper limit [e·cm]	SM prediction [e·cm]	References
Proton	2.0×10^{-26} (95% C.L.)	$\mathcal{O}(10^{-32})$	[16], [17]
Neutron	1.6×10^{-26} (95% C.L.)	$\mathcal{O}(10^{-32})$	[16], [17]
Electron	1.1×10^{-29} (90% C.L.)	$\mathcal{O}(10^{-38})$	[5], [18]
Muon	1.8×10^{-19} (95% C.L.)	$\mathcal{O}(10^{-36})$	[4], [18]

Table 1.2: The upper limits for the EDM of the proton, neutron, electron, and muon, along with their SM predicted values and corresponding references.

the magnitude of particle EDMs are vanishingly small, well below their current upper limits and out of reach of today's experiments. This is demonstrated Table 1.2, where the upper limits for the EDM of the proton, neutron, electron, and muon are presented; along with their SM predicted values and corresponding references.

The SM prediction for the magnitude of the muon EDM in Table 1.2 is estimated based on the electron EDM upper limit, under the assumption of minimal flavour violation (MFV) [19] which requires that EDMs scale linearly with mass across generations of leptons, as follows

$$d_\mu \approx d_e \frac{m_\mu}{m_e}. \tag{1.12}$$

If this assumption holds, then the muon EDM is inaccessible by current experiments, and will remain so for the foreseeable future. However, MFV scaling is called into question by the observation of flavour anomalies in B-decays, such as the recent result from the LHCb experiment [20], lending support to SM extensions which could allow for a muon EDM within reach of E989. Further discussion on this topic is given in the following section.

3 New physics

The discovery of a large muon EDM would signal a significant departure from the SM. In particular, it would necessitate a BSM model involving a new complex parameter with a large CP violating phase, far in excess of that allowed within the SM. It would also indicate a breakdown of the linear mass scaling of EDMs between lepton generations, making it incompatible with the assumption of MFV.

The discrepancy Δa_μ and the bounds on a muon EDM in BSM models are related: the effective field Hamiltonian for the $g-2$ interaction involves a complex Wilson coefficient, $c_R^{\mu\mu}$, which has a real part relating to the magnetic anomaly and an imaginary part

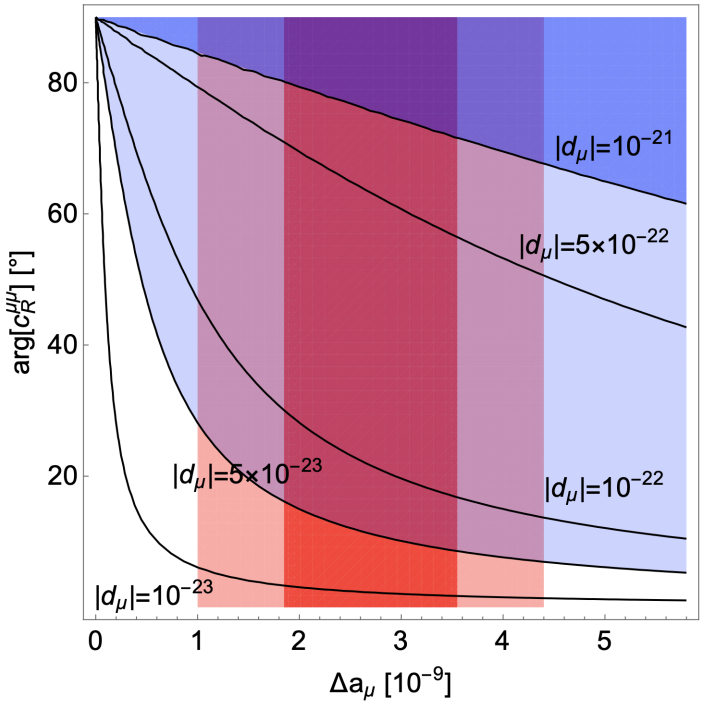

Figure 1.3: Contours of $|d_\mu|$ as a function of the Wilson coefficient phase and Δa_μ. The red bands indicating Δa_μ preferred from experiment (which does not include the most recent Fermilab result [1]), the dark blue band indicating the projected sensitivity of the Fermilab muon EDM search, and the light blue indicating the sensitivity of a proposed experiment at PSI [23]. Image reproduced from [21].

to a non-vanishing EDM. In the various scenarios which resolve Δa_μ with the introduction of heavy TeV-scale particles, the parameter C in Equation 1.4 must be enhanced by allowing the chirality flip of the muon[2] to be provided by a new massive fermion. This so-called chiral enhancement automatically introduces an unconstrained CP violating phase in the imaginary part of $c_R^{\mu\mu}$, allowing for a large muon EDM. Contours of $|d_\mu|$ as a function of the Wilson coefficient phase and Δa_μ are shown in Figure 1.3 [21] [22], with red bands indicating Δa_μ preferred from experiment[3], a dark blue band indicating the projected sensitivity of the Fermilab muon EDM search, and a light blue indicating the same for a proposed search experiment at PSI [23]. From this, it may be inferred that a muon EDM may be measurable at Fermilab, assuming a contribution to Δa_μ from BSM models with chiral enhancement.

A well-known example of a model which can both provide chiral enhancement and accommodate Δa_μ, and violate MFV scaling, is the minimally supersymmetric SM

[2] In quantum field theory, the operator corresponding to a_μ connects left- and right-handed muons, making $g-2$ a chirality flipping interaction.

[3] Excluding the most recent result from Fermilab [1].

(MSSM). Supersymmetry (SUSY) involves the introduction of so-called superpartners to SM particles, which have values of spin offset by 1/2 from their SM counterparts, so that SM fermions have a bosonic superpartner and vice versa. In the MSSM, chiral enhancement is provided by the parameter $\tan\beta$, which is the ratio of vacuum expectation values of the two Higgs fields in the model. MSSM parameter space capable of resolving Δa_μ has been severely constrained by the persistent lack of evidence from the LHC and dark matter searches, with scenarios involving smuons and heavy charginos requiring unfavourably large values of $\tan\beta$. However, one scenario which could accommodate the discrepancy involves a Bino-like[4] lightest supersymmetric particle (LSP) and slepton loop contribution, allowing for a wide range of mass scales and $\tan\beta$ values [24].

A concrete alternative to the MSSM are models which introduce heavy scalar leptoquarks (LQ): BSM bosons which couple simultaneously to SM leptons and quarks, carrying both lepton and baryon number. Scalar LQ models are minimally single particle extensions to the SM, and can resolve Δa_μ via virtual loop interactions at the muon-photon vertex with a chiral enhancement factor of m_t/m_μ, where m_t is the top quark mass [24]. While many LQ models have been excluded, they remain well-motivated by both Δa_μ and the aforementioned flavour anomalies which also call MFV into question.

All considered, the muon EDM search at Fermilab is well motivated by the current landscape of new physics models, some of which allow for measurable values of d_μ while simultaneously accommodating the discrepancy Δa_μ. The discussion presented here is far from exhaustive, and further reading on this topic may be found in [21], [22], and [24].

[4]The B-boson superpartner.

Chapter 2

Experimental principles

Before describing the specific techniques and hardware of the Fermilab Muon $g-2$ experiment, this chapter will outline the underlying physics principles of the measurement of anomalous magnetic momentum of the muon, a_μ, and the search for the muon electric dipole moment.

1 Parity violation in weak interactions

The ability to track the orientation of the muon's polarisation as a function of time is critical to both the measurement of a_μ and the muon EDM search. This orientation, however, is not directly observable: it can only be inferred from an understanding of parity violation in weak nuclear force.

The notion that weak decays may not respect P-symmetry was first postulated by Lee and Yang in 1956 [25], and discovered soon after by Wu in 1957 [26]. Lee and Yang were also the first to notice that this phenomenon could provide a means of studying the orientation of the muon's spin through the decay of pions into muons and muons to electrons[1].

Positive pions, π^+, decay through the weak interaction into antimuons, μ^+, and muon-neutrinos, ν_μ, by

$$\pi^+ \to \mu^+ + \nu_\mu, \tag{2.1}$$

with a branching fraction of >99.9% [27]. The weak force exclusively couples to 'left-handed' (LH) particles and 'right-handed' (RH) antiparticles, where handedness refers to the particle's chirality. In the massless limit, chirality is equivalent to helicity: the component of a particle's spin along its direction of flight, $\hat{p}\cdot\hat{s}$. A massless particle with

[1] This section will hereafter exclusively refer to π^+, μ^+, and e^+ (positrons), as these are most relevant to E989.

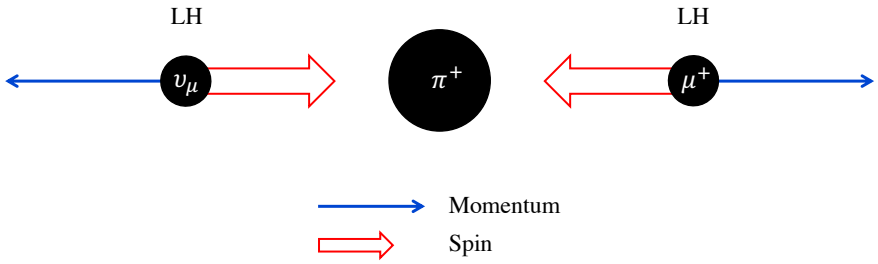

Figure 2.1: A cartoon of a π^+ decay to a μ^+ and a ν_μ, in the π^+ rest frame, illustrating the helicity configurations of the decay products. The effectively massless ν_μ must have a left-handed (LH) configuration within the SM (with its spin and momentum antiparallel), and conservation of angular momentum requires that the μ^+ is also produced with a LH configuration.

LH helicity is one whose spin and momentum vectors lie anti-parallel, while the reverse is true for a RH massless particle. Neutrinos may be treated as effectively massless within the SM, so the ν_μ produced in the π^+ decay has a LH helicity configuration. Pions are spin-0 particles, with no intrinsic angular momentum, so the μ^+ spin vector must have the opposite orientation to the ν_μ spin vector in order to conserve angular momentum. Since, in a two-body decay, the rest frame momentum vectors of the decay products oppose one another, the μ^+ is produced with its spin and momentum antiparallel (with LH helicity). Such decays are sometimes called 'backwards decays', illustrated in Figure 2.1. A π^- decay would produce a RH 'forwards' going μ^-.

Helicity is not Lorentz invariant, so, in the laboratory frame, muons are produced with a correlation between the orientation of their spin and momentum vectors, rather than with them perfectly antiparallel. Even so, this correlation makes it possible to produce a highly polarised muon beam by selecting those muons with the highest momentum (in the limit $v \to c$ the beam would be 100% polarised). In this way, the initial orientation of the spin polarisation vector may be known.

Following a rest frame lifetime of 2.2 µs, nearly 100% of the μ^+ will decay, again via the weak interaction, by

$$\mu^+ \to e^+ + \nu_e + \bar{\nu}_\mu, \tag{2.2}$$

where the ν_e and $\bar{\nu}_\mu$ have LH and RH helicity configurations respectively [27]. In the case

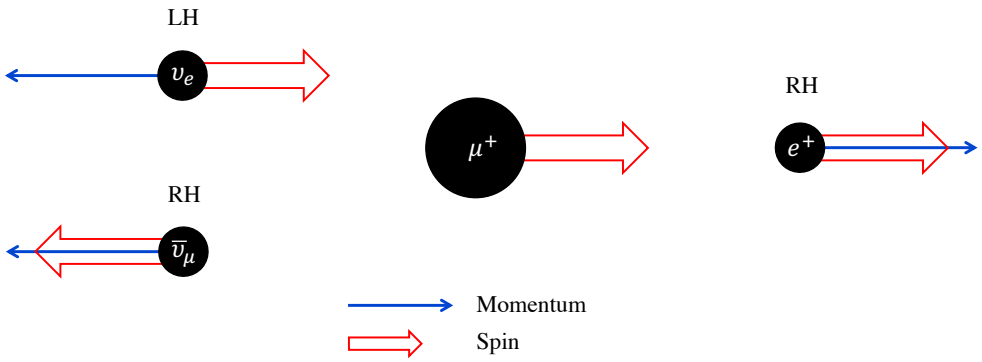

Figure 2.2: A diagram of muon decay in the case where the energy of the decay positron is maximised. Conservation of angular momentum results in a preference for the spin vector of high energy decay positrons to be aligned with that of the parent muon.

where the e^+ energy is maximised, with a rest frame energy of $m_\mu/2$, the two neutrinos carry the remaining energy in the opposite direction to the e^+ (so their momentum vectors are aligned). In this configuration, illustrated in Figure 2.2, the two neutrinos have antiparallel spin vectors with a net angular momentum of zero. In order to conserve the μ^+ angular momentum, the e^+ spin must be aligned with that of the parent μ^+, giving it a RH helicity. The reverse is true in the situation where e^+ energy is minimised, where in this case the e^+ spin must be antiparallel with that of the parent μ^+. Again, helicity is not Lorentz invariant, so the result in the laboratory frame is an energy dependent correlation between the direction the e^+ momentum and μ^+ spin. This means that energy of the decay positrons encodes information about the orientation of the muon spin vector at the time of decay.

2 Measuring a_μ

2.1 Larmor precession

A muon placed in an external magnetic field, $\vec{B}$, will experience a torque which depends on its magnetic moment, $\vec{\tau} = \vec{\mu} \times \vec{B}$, inducing a rotation of the spin vector about the magnetic field lines. In the muon rest frame, the angular frequency of spin-precession,

ω_s, is given by the Larmor frequency:

$$\vec{\omega}_s = g_\mu \frac{Qe}{2m}\vec{B}. \tag{2.3}$$

From this expression, it can be deduced that g_μ may be measured by injecting non-relativistic muons into a magnetic field and performing a simultaneous measurements of ω_s and B, where ω_s is determined by making use of the correlation between decay $e^{\pm}$ energy and spin orientation from the parity violation arguments outlined in the previous section.

2.2 The anomalous precession frequency, ω_a

A muon moving through a homogeneous magnetic field will not only undergo Larmor precession, at an angular frequency ω_s, but will also be subject to the Lorentz force; causing it to travel in a circle of constant radius. This is cyclotron motion, where the angular cyclotron frequency, ω_c, is defined by

$$\vec{\omega}_c = \frac{Qe}{m_\mu}\vec{B}. \tag{2.4}$$

Remarkably, the difference between ω_c and ω_s has a direct dependence on the muon magnetic anomaly, $a_\mu = (g_\mu - 2)/2$. This relative frequency is the anomaly frequency, ω_a, defined as follows:

$$\vec{\omega}_a = \vec{\omega}_s - \vec{\omega}_c = \left(\frac{g_\mu}{2} - 1\right)\frac{Qe}{m}\vec{B} = a_\mu \frac{Qe}{m}\vec{B}. \tag{2.5}$$

A illustration of a population of spin polarised muons undergoing both Larmor precession and cyclotron motion in a constant magnetic field, in the case where $g_\mu = 2$ ($\omega_a = 0$) and $g_\mu \neq 2$ ($\omega_a \neq 0$), is shown in Figure 2.3.

2.3 Measuring ω_a

The anomaly frequency is measured by making use of the parity violation arguments outlined in Section 1, which give a correlation between e^+ emission angle and μ^+ spin vector which depends on the e^+ energy. Because of this, the population of high energy e^+ will vary as a function of time with a frequency equal to ω_a, where the maxima of the oscillation will occur when the muon spin and momentum vectors are aligned, and the

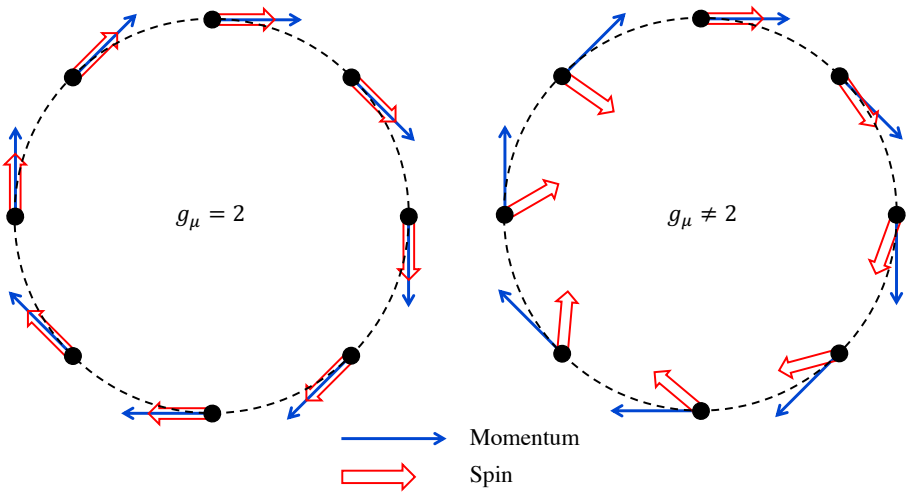

Figure 2.3: An illustration of the relative precession of the spin polarisation and momentum vectors of a muon traversing a constant magnetic field, where the magnetic field lines are directed out of the page and the muons are injected at 12 o'clock. If $g_\mu = 2$, then the two vectors will remain in phase; if $g_\mu \neq 2$ then they will move out of phase. The rate of precession of the spin vector relative to the momentum vector is the anomaly frequency, $\vec{\omega}_a$, enabling a direct measurement of a_μ.

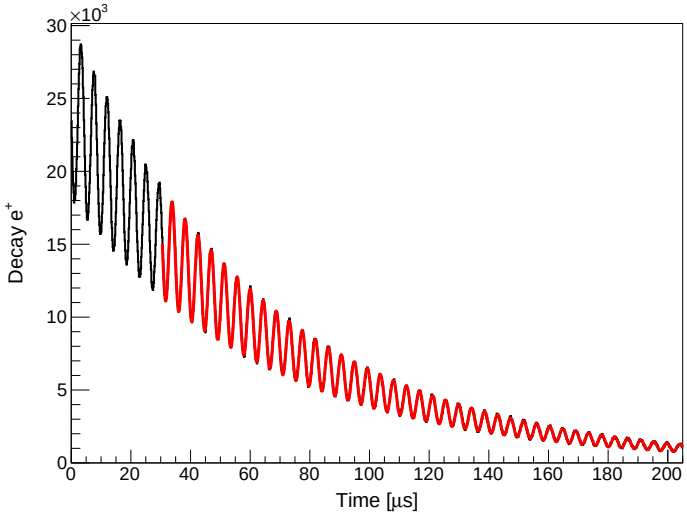

Figure 2.4: A toy model of the subset of high energy e^+ emitted from an exponentially decaying population of muons, varying at the anomaly frequency, ω_a, which is extracted from the data by use of a sinusoidal fit (illustrated by a red curve).

minima when they are antialigned. The choice of low energy threshold used to define 'high energy e^+' is discussed in Section 2.5. The anomalous precession oscillation may be fitted with a sinusoidal function in order to extract the frequency, which is illustrated by use of a toy model in Figure 2.4.

2.4 Corrections to ω_a

It is highly advantageous to use relativistic muons when conducting a measurement of a_μ, or the muon EDM, not least because this allows for a longer measurement period due to the dilation of laboratory frame muon lifetime by factor of γ (the Lorentz factor, $1/\sqrt{1-v^2/c^2}$). For relativistic muons, the Larmor precession angular frequency must be corrected to account for the relative rotation of the muon rest frame and the laboratory frame. This correction is known as Thomas precession [28], where the modified angular spin-precession frequency is given by

$$\vec{\omega}_s = g_\mu \frac{Qe}{2m_\mu} + (1-\gamma)\frac{Qe}{m_\mu \gamma}\vec{B}. \tag{2.6}$$

The cyclotron angular frequency also receives a relativistic correction, by

$$\vec{\omega}_c = g_\mu \frac{Qe}{\gamma m_\mu}\vec{B}, \tag{2.7}$$

resulting in a modified expression for ω_a:

$$\vec{\omega}_a = g_\mu \frac{Qe}{2m_\mu} + (1-\gamma)\frac{Qe}{m_\mu \gamma}\vec{B} - g_\mu \frac{Qe}{\gamma m_\mu}\vec{B}. \tag{2.8}$$

The relativistic parts of the above equation cancel, returning a simplified expression equal to the non-relativistic Equation 2.5.

As a further complication, the E989 storage ring employs electrostatic quadrupoles (ESQs) to provide vertical focusing to the beam – discussed in detail in Chapter 3 Section 3.3. The presence of an external electric field, $\vec{E}$, modifies both ω_s and ω_c again, so that ω_a is described by

$$\vec{\omega}_a = \frac{Qe}{m_\mu}\left[a_\mu \vec{B} - a_\mu \left(\frac{\gamma}{\gamma+1}\right)(\vec{\beta}\cdot\vec{B})\,\vec{\beta} - \left(a_\mu - \frac{\gamma}{1-\gamma^2}\right)(\vec{\beta}\times\vec{E})\right]. \tag{2.9}$$

Two steps can be taken to simplify Equation 2.9. The first is use the approximation $\beta\cdot\vec{B} \approx 0$, where the muon momentum vector is assumed to be orthogonal to the magnetic field lines, reducing the second term to zero. This assumption holds when averaging over the full orbit, but vertical betatron oscillations[2] introduce periodic changes in the 'pitch' of the muon momentum vector: necessitating a small correction to ω_a, known as the

[2]Discussed further in Chapter 3 Section 4.

pitch correction. The second step is to select a value of γ such that

$$\gamma = \sqrt{1 + \frac{1}{a_\mu}}, \tag{2.10}$$

which is often referred to as the 'magic' γ, corresponding to a momentum of 3.094 GeV[3], or the 'magic' momentum, which reduces the third term to zero. In practice, the muon momentum is distributed about the magic momentum with a width of $\pm 0.15\%$, so that an additional correction, termed the E-field correction, is required to accurately measure ω_a. Further reading on these corrections, as applied to E989 Run-1 data, can be found in [29] and [30].

2.5 Sensitivity to ω_a

As discussed previously, the ω_a signal arises from the energy dependent correlation between the orientation of the parent muon spin vector and the decay positron momentum vector. This relationship will be referred to here as the decay asymmetry, and it must be optimised with carefully selected energy cuts in order to maximise sensitivity to ω_a. If positrons across the full energy spectrum were counted, then all that would be observed would be a pure exponential from the decaying muon population; whereas if only positrons with maximum energy were counted, the decay asymmetry would be maximised, but the number of positrons collected would be extremely small and the statistical uncertainty very high. The correct approach is to choose a low energy threshold which gives the optimum balance between decay asymmetry and statistical sensitivity.

In the muon rest frame, hereafter indicated by asterisks, the differential probability of positron emission into a solid angle $d\Omega^*$ is given by

$$dP(\lambda^*, \theta^*) \propto N(\lambda^*)[1 - A(\lambda^*)\cos(\theta^*)]d\lambda^* d\Omega^*, \tag{2.11}$$

where $\lambda^* = E^*/E^*_{max}$ (the positron fractional energy), $N(\lambda^*)$ is the number distribution function (the number of positrons as a function of λ^*), $A(\lambda^*)$ is the decay asymmetry function, and θ^* is the angle between the muon spin and positron momentum at the time of decay. Assuming that $E^* >> m_e$, $N(\lambda^*)$ and $A(\lambda^*)$ are given by

$$N(\lambda^*) = 2\lambda^{*2}(3 - 2\lambda^*), \tag{2.12}$$

[3]Momentum will be expressed in natural units, where $\hbar = c = 1$, throughout this thesis.

and

$$A(\lambda^*) = \frac{2\lambda^* - 1}{3 - 2\lambda^*}, \tag{2.13}$$

which are illustrated in Figure 2.5a. Transforming into the laboratory frame and taking $\theta = \omega_a t + \phi$, where ω_a is the aforementioned anomalous spin precession angular frequency, t is the time since injection discussed in Chapter 3 Section 3, and $\phi(\lambda)$ is the phase as a function of laboratory frame fractional energy, gives the number oscillation as a function of time and energy,

$$N(\lambda, t) = N_0(\lambda) e^{-t/\gamma\tau_\mu} [1 + A(\lambda) \cos(\omega_a t + \phi(\lambda))]. \tag{2.14}$$

The parameter N_0 in the above expression is the overall normalisation, τ is the muon lifetime in the rest frame, γ is the 'magic' Lorentz factor defined by Equation 2.10, and $A(\lambda)$ is the laboratory frame decay asymmetry. This, Equation 2.14, is the basic five-parameter function used to extract ω_a via an unconstrained fit to the number oscillation above some energy threshold, the same expression used in the toy fit shown in Figure 2.4. The laboratory frame number distribution function is given by

$$N(\lambda) = \frac{1}{3}(\lambda - 1)(4\lambda^2 - 5\lambda - 5), \tag{2.15}$$

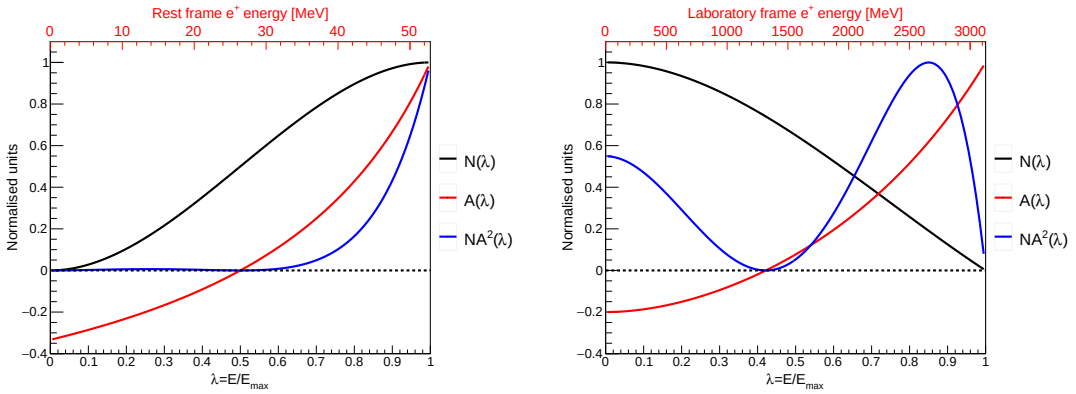

(a) Rest frame. **(b)** Laboratory frame.

Figure 2.5: The number distribution function, N, the decay asymmetry function, A, and the statistical figure-of-merit function, NA^2, against fractional positron energy in (a) the muon rest frame and (b) the laboratory frame.

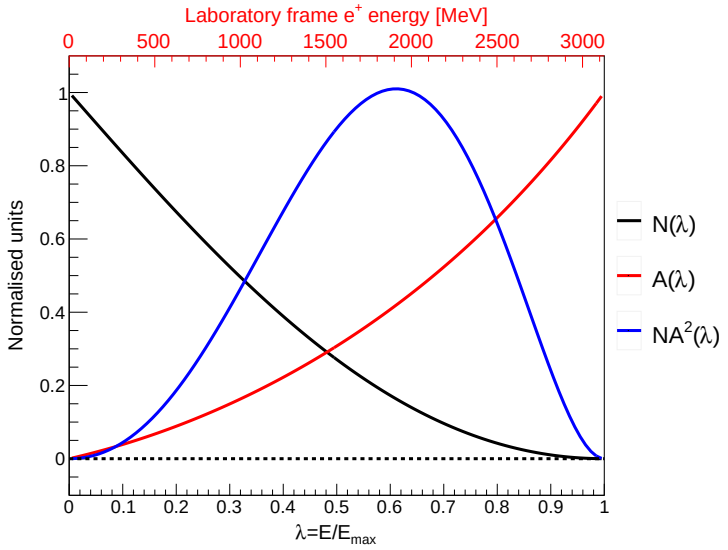

Figure 2.6: The number distribution function, $N(\lambda)$, the decay asymmetry function, $A(\lambda)$, and the statistical figure-of-merit function, $NA^2(\lambda)$, in the laboratory frame; for a subset of positrons above some energy threshold.

and the decay asymmetry function by

$$A(\lambda) = \frac{1 + \lambda - 8\lambda^2}{4\lambda^2 - 5\lambda - 5}, \tag{2.16}$$

both of which are illustrated in Figure 2.5b. For a subset of positrons above some energy threshold, E_{th}, these expressions must be modified again by integration from λ_{th} to one, so that

$$N(\lambda_{th}) = \frac{1}{3}(\lambda_{th} - 1)^2(-\lambda_{th}^2 + \lambda_{th} + 3) \tag{2.17}$$

and

$$A(\lambda_{th}) = \frac{\lambda_{th}(2\lambda_{th} + 1)}{3 + \lambda_{th} - \lambda_{th}^2}, \tag{2.18}$$

which is shown in Figure 2.6.

The statistical uncertainty associated with ω_a may then be found by fitting the above-threshold number oscillation with the five-parameter function (Equation 2.14), which is inversely proportional to the statistical figure-of-merit (FOM) NA^2, by

$$\frac{\delta\omega_a}{\omega_a} = \frac{\sqrt{2}}{\omega_a \tau \sqrt{N} A}, \tag{2.19}$$

where N refers to the total number of positrons. The ideal energy threshold is then the point where NA^2 is maximised [31]. Further discussion on this topic can be found

in [32]. In E989, accounting for detector effects such as resolution and acceptance, this threshold is found to be 1.7 GeV [29].

2.6 The final determination of a_μ

To make a determination of a_μ, the magnetic field must also be measured to a high precision. In E989, this is accomplished by the use of nuclear magnetic resonance (NMR) magnetometers, called probes, where a simplified version of the procedure involves measuring the Larmor precession frequency of a free proton, ω_p, which is used to relate the magnetic field by

$$\omega_p = 2\mu_p B, \tag{2.20}$$

where μ_p is the magnetic moment of the proton. A detailed discussed of the E989 magnetic field system is given in Chapter 2 Section 5, as well as [33]. Combining Equation 2.5 and Equation 2.20 allows for a_μ to be expressed in terms of ω_a and ω_p, such that

$$a_\mu = \frac{\omega_a}{\omega_p}\frac{2\mu_p m_\mu}{Qe}, \tag{2.21}$$

which can be rewritten in terms of the scalar electron magnetic moment

$$\mu_e = g_e \frac{Qe}{4m_e}, \tag{2.22}$$

allowing a_μ to be written in terms of the two frequencies measured in the experiment and three well-measured ratios:

$$a_\mu = \frac{g_e}{2}\frac{\omega_a}{\omega_p}\frac{m_\mu}{m_e}\frac{\mu_p}{\mu_e}. \tag{2.23}$$

As of 2018, g_e, m_μ/m_e, and μ_p/μ_e are known to within 0.00017 ppb, 22 ppb, and 0.3 ppb respectively [34]. These uncertainties, with a quadrature sum of 22 ppb (compared with E989's target precision of 140 ppb), do not present any limitation to the precision on the final determination of a_μ at Fermilab.

3 Searching for a muon EDM

3.1 The spin precession plane tilt angle

A muon with an electric dipole moment (EDM) of zero undergoing spin precession in a magnetic field will do so in the manner described previously: with its spin polarisation vector orthogonal to the magnetic field lines, as illustrated in Figure 2.7a. However, if the muon EDM is non-zero, and the muon is relativistic, it will experience a torque due to the electric field induced by the Lorentz transformation of the laboratory magnetic field into the muon rest frame. In E989, external electric fields generated by the beam focusing electrostatic quadrupoles (ESQs), described in Chapter 3 Section 3.3, also contribute to this torque, resulting in a tilted precession plane where the angle between the polarisation vector and the magnetic field lines is directly related to the size of the muon EDM, d_μ. An illustration of a tilted spin precession due to non-zero muon EDM is shown in Figure 2.7b.

A tilt in the spin precession plane resulting from a non-zero muon EDM would introduce an additional angular frequency, $\vec{\omega}_\eta$, orthogonal to $\vec{\omega}_a$, which is described in the approximation $\vec{\beta} \cdot \vec{E} \approx 0$ (so that the muon momentum vector is orthogonal to the ESQ electric field, $\vec{E}$) by

$$\vec{\omega}_\eta = \eta \frac{Qe}{2m} \left(\vec{\beta} \times \vec{B} + \frac{\vec{E}}{c} \right), \tag{2.24}$$

where η is the dimensionless coupling between EDM and the spin described in Equation 1.9, and the $\vec{\beta} \times \vec{B}$ term is representative of the influence of the induced electric field from the Lorentz transformation of the magnetic field. In rest frame of the muon (again, indicated by asterisks), the spin precession plane tilt angle, δ^*, is given by

$$\delta^* = \tan^{-1} \left(\frac{\omega_\eta}{\omega_a} \right) = \tan^{-1} \left(\frac{\eta \beta}{2a_\mu} \right), \tag{2.25}$$

which may be transformed into the laboratory frame by letting $\vec{\omega}_\eta$ be directed along the x-axis and $\vec{\omega}_\eta$ along the y-axis, so that δ^* may be written as

$$\delta^* = \tan^{-1} \left(\frac{\Delta x^*}{\Delta y^*} \right), \tag{2.26}$$

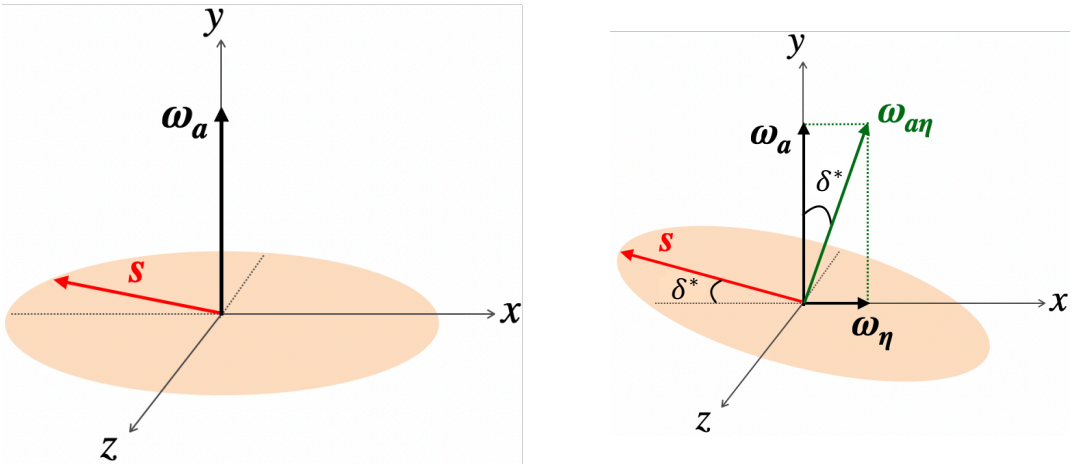

(a) No EDM. **(b)** Non-zero EDM.

Figure 2.7: The muon spin precession plane with in the case of (a) no EDM and (b) a non-zero EDM, where the plane is tilted in the muon rest frame by a maximum angle δ^*. The magnetic field lines are directed along the y-axis and the z-axis is aligned with the direction of motion in the laboratory frame. Images courtesy of R. Chislett [35].

where Δx^* and Δy^* may be Lorentz boosted to the laboratory frame by

$$\Delta x = \frac{\Delta x^*}{\gamma} \quad \text{and} \quad \Delta y = \Delta y^*. \tag{2.27}$$

The expression for the laboratory frame tilt angle, δ, is then

$$\delta = \tan^{-1}\left(\frac{\Delta x^*}{\gamma \Delta y^*}\right) = \tan^{-1}\left(\frac{\tan\delta^*}{\gamma}\right), \tag{2.28}$$

which is reduced compared the rest frame. In practice, the small angle approximation may be applied, so that this reduction is simply equal to a factor of $1/\gamma$. Finally, the relationship between the d_μ and δ may be found by combining Equations 1.9, 2.25, and 2.28, so that

$$d_\mu = \frac{Qe\gamma\hbar a_\mu}{2m_\mu c\beta}\tan\delta. \tag{2.29}$$

3.2 The change in a_μ due to a muon EDM

The oscillation induced by a non-zero EDM increases the total angular frequency of spin precession, $\omega_{a\eta}$, by

$$\omega_{a\eta} = \sqrt{\omega_a^2 + \omega_\eta^2} \tag{2.30}$$

In principle, this means that non-zero muon EDM could account for the observed deviation in a_μ, where the value of d_μ required may be estimated by equating the necessary fractional increase in spin precession frequency to the fractional deviation in a_μ. The resulting EDM for a discrepancy Δa_μ may then be estimated by the expression

$$d_\mu = \sqrt{\Delta a_\mu} \cdot \frac{a_\mu^{\mathrm{Exp}}}{\sqrt{a_\mu^{\mathrm{SM}}}} \cdot \frac{\hbar e}{\sqrt{2} m_\mu c \beta}, \tag{2.31}$$

for which a full derivation is given in Appendix A.

Taking the values of a_μ^{Exp}, a_μ^{SM}, and Δa_μ stated in Chapter 1 Section 1, and attributing the entirety of Δa_μ to d_μ, gives a muon EDM with a value

$$d_\mu = (2.3 \pm 0.3) \times 10^{-19}\, e \cdot \mathrm{cm}.$$

This exceeds the current upper limit of $|d_\mu| < 1.8 \times 10^{-19}\, e \cdot \mathrm{cm}$ (95% C.L.) [4], meaning that the probability of Δa_μ being driven entirely by a non-zero muon EDM is less than 5%. Moreover, this is $\mathcal{O}(10^{10})$ larger than the current upper limit on the electron EDM[4] [5], and is beyond the realms of BSM models which allow for a large muon EDM. Any remaining ambiguity as to a contribution to Δa_μ from d_μ further motivates the muon EDM search at E989.

3.3 The vertical decay angle based search

A number of approaches exist for measuring δ, but this work will focus on a search technique based on a direct measurement of the oscillation in the average vertical angle of decay positrons by use of two straw tracker detectors. The equivalent tracker-based analysis at BNL, called the 'traceback analysis', was statistically limited, rather than systematically limited as the calorimeter-based methods were [4]: meaning that a tracker-based EDM search at Fermilab offers obvious potential for an improvement in sensitivity over BNL, due the availability of a much larger integrated dataset[5]. The E989 detector systems, including the straw trackers, are introduced in Chapter 3 Section 6, and an overview of the E989 datasets is provided in Chapter 3 Section 7.

As with the measurement of ω_a, this method relies on the energy dependent corre-

[4] Or, $\mathcal{O}(10^8)$ larger than the corresponding indirect upper limit on the muon EDM, assuming the linear mass scaling discussed in Chapter 1 Section 2.

[5] Note that this does not necessarily mean that the calorimeter-based methods are inferior to the tracker-based method.

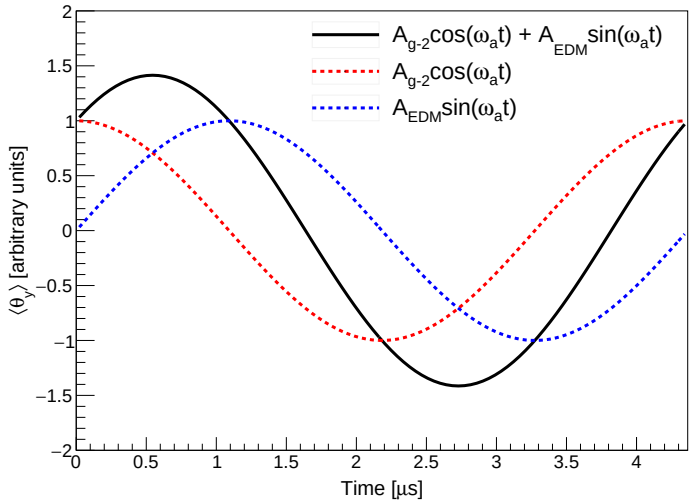

Figure 2.8: An illustration of the average vertical angle fit function, Equation 2.33, over a single $g-2$ period (4.365 μs) compared with its individual orthogonal sine and cosine terms. The phase, ϕ, and offset, c, are set to zero.

lation between the muon spin vector and the momentum vector of the decay positron. In the context of a muon undergoing spin precession with tilted precession plane, this correlation would result in an oscillation in the average vertical decay angle of emitted positrons at an angular frequency $\omega_{a\eta}$. The vertical decay angle, θ_y, is defined in this thesis as the angle that momentum vector makes with the x-z plane in the laboratory frame, so that

$$\theta_y = \sin^{-1}\left(\frac{p_y}{p}\right). \tag{2.32}$$

As noted previously, the maxima and minima of the ω_a oscillation occurs when the muon spin and momentum either are aligned or antialigned. In the case of the ω_η oscillation the maxima and minima occur when the tilt angle is maximised: when the spin vector is orthogonal to the momentum vector. As a result of this, the oscillation in average vertical angle, $\langle\theta_y\rangle$, is $\pi/2$ out-of-phase with ω_a. To then begin extracting δ, the average vertical angle, $\langle\theta_y\rangle$, must be fitted with a function consisting of two orthogonal terms, plus a constant offset, c, as follows:

$$\langle\theta_y\rangle(t) = A_{g-2}\cos(\omega_a t + \phi) + A_{\mathrm{EDM}}\sin(\omega_a t + \phi) + c, \tag{2.33}$$

where amplitudes A_{g-2} and A_{EDM} represent the observed angle in-phase with the ω_a $(g-2)$ oscillation and the ω_η (EDM) oscillations respectively, and ϕ is the constant

phase of the ω_a oscillation. It is assumed that $\omega_a >> \omega_\eta$, so the angular frequency of the oscillation is taken as ω_a. The measured angle A_{EDM} must then be corrected to obtain δ, as will be expanded upon in the following section. The fit function, Equation 2.33, is illustrated in Figure 2.8.

3.4 Sensitivity to a muon EDM

The EDM search applies the same process of optimising the decay asymmetry and statistical sensitivity as the ω_a measurement, described in Section 2.5. The decay asymmetry function in this case relates to vertical (up/down) decays with a tilted spin precession plane, rather than the asymmetry for decays in the x-z plane. A major point of difference here is that when the laboratory frame muon spin and momentum vectors are maximally aligned or anti-aligned, the boosted tilt angle is instantaneously zero. This means that there is no sensitivity to an EDM at maximum and minimum positron energy, which is reflected in the asymmetry function going to zero, as will be shown.

The time dependent probability of positron emission with a titled spin precession plane is given is given by

$$P(\lambda^*, \theta^*, \phi^*, t) \propto N(\lambda^*)\Big(1 + A(\lambda^*)\cos\alpha(\theta^*, \phi^*, t)\Big), \tag{2.34}$$

where θ^* and ϕ^* are the angles the positron momentum vector makes with the z and x axes in the rest frame, and α is the angle between the muon spin vector and the positron momentum vector, so that $\cos(\alpha) = \hat{s} \cdot \hat{p}$. The rest frame number and asymmetry functions, $N(\lambda^*)$ and $A(\lambda^*)$, are equal to those given in Equations 2.12 and 2.13. Transforming into the laboratory frame, and integrating between λ and 1, yields

$$A(\lambda) = \frac{\sqrt{\lambda(1-\lambda)}(1-4\lambda)}{5 + 5\lambda - 4\lambda^2}, \tag{2.35}$$

with a statistical figure-of-merit (FOM) described by

$$NA^2(\lambda) \propto \frac{\lambda(1-\lambda)^2(1+4\lambda)^2}{5 + 5\lambda - 4\lambda^2}, \tag{2.36}$$

where $N(\lambda)$ is given by Equation 2.15. A full derivation of the EDM asymmetry expressions by P. Debevec can be found in [36]. As illustrated in Figure 2.9, the FOM function indicates that statistical sensitivity to an EDM is highest at middling positron energy.

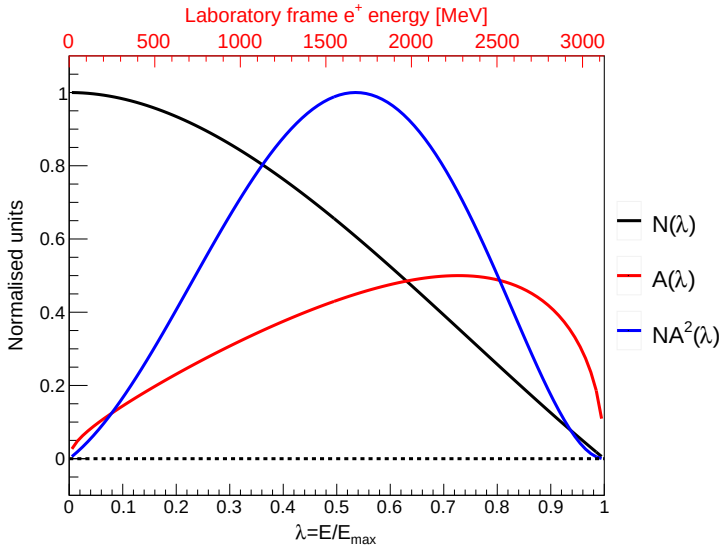

Figure 2.9: The number distribution function, $N(\lambda)$, the decay asymmetry function, $A(\lambda)$, and the statistical figure-of-merit function, $NA^2(\lambda)$, in the laboratory frame; for up/down decays and a non-zero muon EDM.

The asymmetry and statistical FOM functions are verified in simulation in Chapter 5 Section 2.

With a tilted precession plane, it might be expected that the size of average observed vertical angle in-phase with ω_η, $A_{\rm EDM}$ from Equation 2.33, would follow the same dependence on energy as the asymmetry function described above. However, the Lorentz transformation into the laboratory frame results in a momentum dependent variation of the width of the vertical angle distribution, so that the average observed vertical angle is decreases with energy. A description of the variation of the maximum vertical angle with momentum, based on kinematic arguments, is given in Appendix B. In order to properly describe the variation of the angle associated with an EDM, both the asymmetry and the Lorentz transformation of the vertical angle must be accounted for. Following the derivation outlined by J. Price in [37], the expression for the laboratory frame average vertical angle for decays occurring at the point of maximum tilt is given by

$$\langle \theta_y^{\rm EDM} \rangle(\lambda) \propto \frac{(\lambda-1)(2\lambda+1)}{4\lambda^2-5\lambda-5}\frac{\sin\delta^*}{\gamma}, \tag{2.37}$$

where $\sin\delta^*/\gamma \approx \delta$ by the small angle approximation. If all decays could be perfectly observed, and if δ^* were known, the above expression would describe the observed variation in the average vertical angle from an EDM exactly. The level of reduction of $\langle \theta_y^{\rm EDM} \rangle$

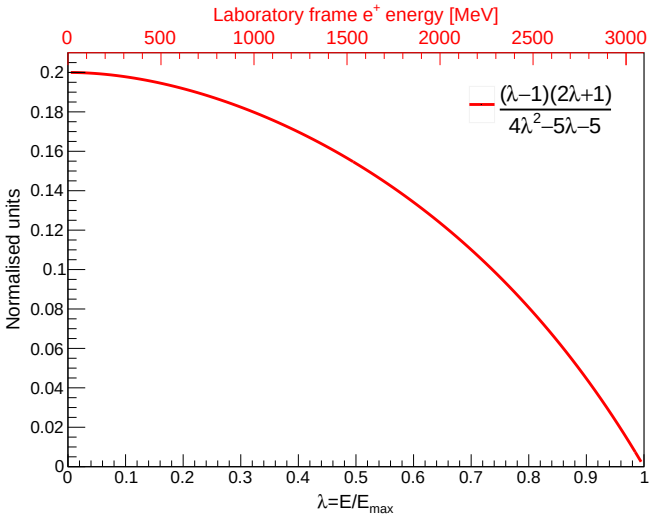

Figure 2.10: The normalised dilution function, Equation 2.38, characterising the momentum dependant reduction in the observed angle, A_{EDM}, compared to laboratory frame tilt angle, δ.

compared to δ is termed 'dilution', d_{EDM}, which may be expressed as a function of λ by

$$d_{\mathrm{EDM}}(\lambda) = \frac{1}{\delta} \cdot \langle \theta_y^{\mathrm{EDM}} \rangle (\lambda), \tag{2.38}$$

and is generally referred to as the 'dilution function' in this thesis. Efforts to characterise the dilution of δ, with the inclusion of detector acceptance, is discussed in detail in Chapter 5. An illustration of the dilution function, Equation 2.38, is shown in Figure 2.10.

Chapter 3

The Fermilab Muon $g-2$ experiment

The Muon $g-2$ experiment at Fermilab (E989) is the latest iteration of a six decade-long campaign to both measure the muon magnetic anomaly, a_μ, and search for the muon EDM. E989 builds on the foundations laid by early efforts the Columbia-Nevis and University of Liverpool cyclotrons in the late 1950s, through a trio of direct measurements at *European Organisation for Nuclear Research* (CERN) from the early 1960s to late 1970s, to the BNL E821 experiment in the 1990s and early 2000s – even reusing the superconducting magnetic storage ring from E821 [38, and references therein]. This most recent experiment makes use of the intense muon beam available from Fermilab's powerful accelerators, as well upgraded instrumentation, to target an unprecedented precision of 140 ppb on a_μ, and a world-leading muon EDM upper limit of $\sim 10^{-21}$ e·cm [39]. This chapter will outline the specific experimental techniques and hardware that comprise the E989 experiment.

1 Overview

E989 is designed to receive a beam of relativistic, longitudinally polarised muons and hold them in a stable circular orbit through a vertically aligned, homogeneous magnetic field. Following a time-dilated lifetime of 64.4 µs, the muons decay, and their much less massive decay products (positrons) curl away from the storage region, towards to centre of the ring. The decay positrons carry with them information pertaining to both a_μ and the muon EDM, which is measured by a suite of detectors instrumenting the ring interior. The magnetic field is precisely measured by a system of NMR probes. A photograph of the experiment is shown in Figure 3.1. A schematic diagram of the

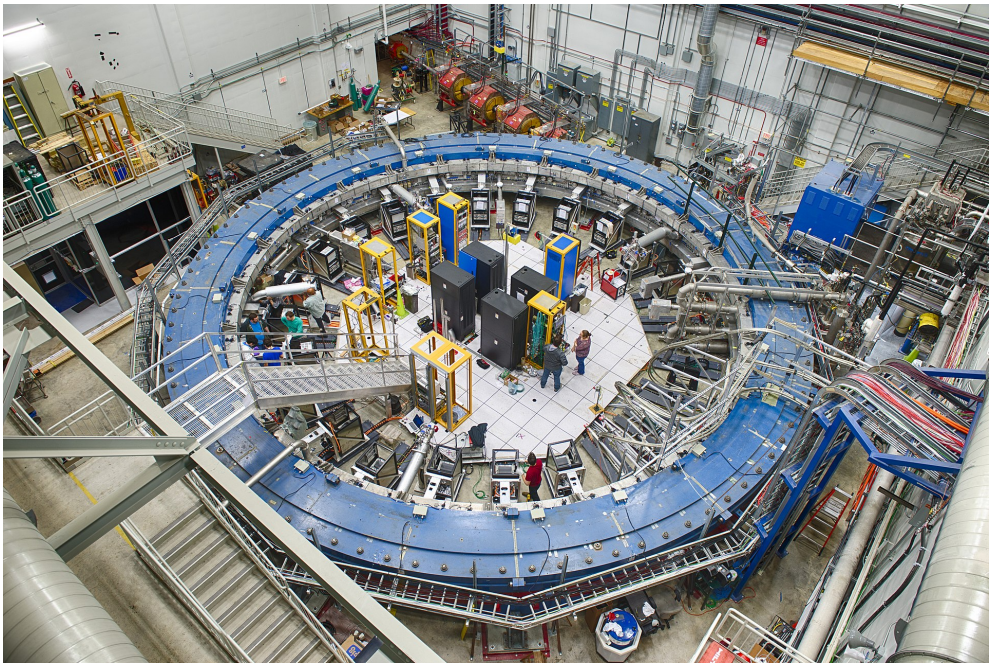

Figure 3.1: A photograph of the Fermilab Muon $g-2$ experiment (E989).

experiment may be found on the final page of this chapter, in Figure 3.20.

2 Muon production

A large part of the motivation for conducting E989 at Fermilab was the availability of a highly intense muon beam from its vast accelerator complex, a schematic of which is show in Figure 3.2. The beamline begins at the linear accelerator (linac), where hydrogen gas is ionised and accelerated, before being delivered as beam of protons to a synchrotron known as the 'booster'. The booster accelerates the protons to 8 GeV and separates them into bunches of 4×10^{12}, which are then passed to a second synchrotron known as the 'recycler'. The purpose of the recycler is to separate the intial bunches into four sets of 1×10^{12}, each with a width in time of 120 ns, which is less than the 149.2 ns cyclotron period of the E989 storage ring. This 're-bunching' process is undertaken with the requirements of E989 in mind, the aim being to bring the eventual rate of flux within the tolerances of the detectors and data acquisition system (DAQ). Following this, the 120 ns bunches are separated by time interval of at least 10 ms and delivered along the in groups of eight to the target hall. Over a full 1.4 s accelerator supercyle, E989 receives sixteen pulses at an average rate of 11.4 Hz, where the timing structure of proton delivery is illustrated in Figure 3.3.

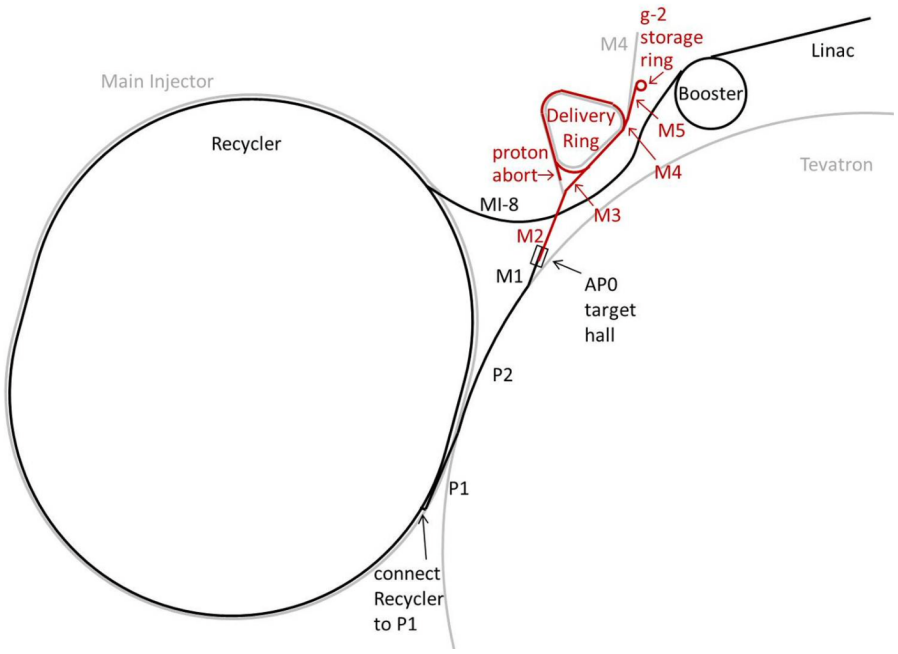

Figure 3.2: A schematic of the Fermilab accelerator complex, which delivers an intense and highly spin polarised beam of 3.094 GeV positive muons to the E989 storage ring. Image reproduced from [39].

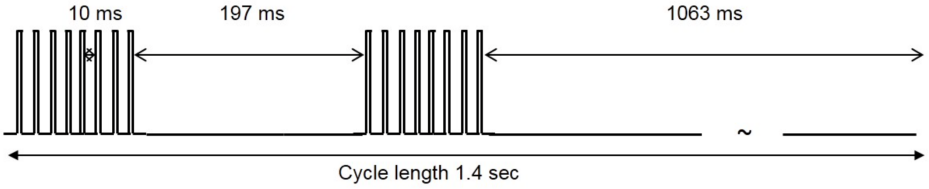

Figure 3.3: The timing of beam pulses delivered to E989 over a single accelerator supercycle. Image reproduced from [39].

Once delivered to the target hall, the protons are directed at an Inconel target, a high-Z nickel-iron alloy, where the ensuing proton-nucleon interactions results in the production of large quantities of pions. The pions are focused by a lithium lens downstream of the production target, and a bending magnet is used to select positive pions with a momentum within ±10% of 3.11 GeV. The beam is then sent to the 'delivery ring', where the pions that have not already decayed into muons are given time to do so by the process given in Equation 2.1. Within the delivery ring, muons with highest momentum are selected, ensuring that the muon beam is highly spin polarised in the manner shown in Figure 2.1. The delivery ring also serves the purpose of removing residual protons and deuterons by use of an electromagnetic kicker. Finally, the muons

are sent to the E989 experiment hall, where they pass through four electromagnetic focusing quadrupoles before being injected into the storage ring as a highly polarised beam with a momentum spread of $\pm 1.6\%$ [30] about the magic momentum, 3.094 GeV. Further discussion on the accelerator complex and muon delivery to E989 may be found in [40].

3 Injection and storage

3.1 The inflector

The E989 main magnet is designed to produce a homogenous magnetic field around the full azimuth of the ring, necessitating a monolithic construction with as few gaps as possible. Because of this, the muons must be injected directly through the magnet yoke (discussed in Section 5). In order to achieve this without the beam being deflected, the muons are passed through a specialised field cancelling device called the 'superconducting inflector magnet', or 'inflector', which is oriented at an approximate tangent to the storage ring. The inflector consists of superconducting niobium-titanium-copper-aluminium coils, wrapped to give the unique geometry of electric currents required to almost completely cancel the main magnetic field, shown in Figure 3.4. The positioning of the inflector relative to storage ring as whole is shown in Figure 3.20. The time at which the beam passes through the inflector marks the beginning of period known as a

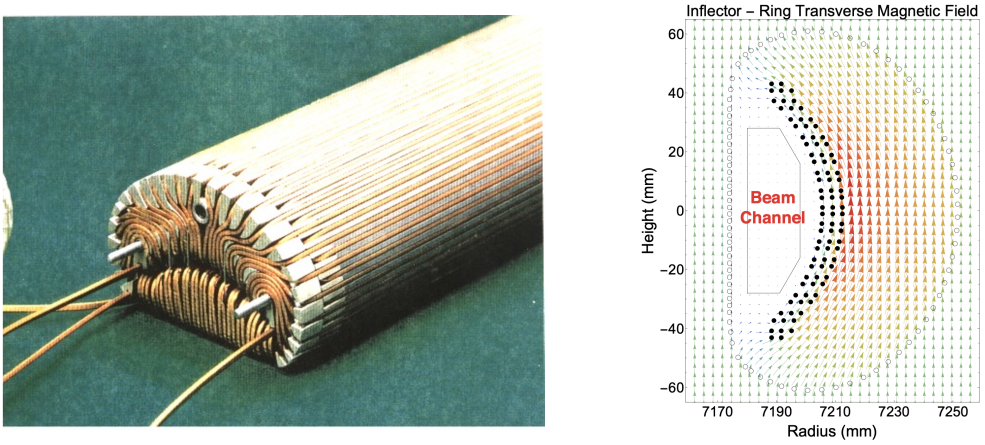

(a) **(b)**

Figure 3.4: (a) A photograph showing an end view of the inflector; (b) the sum of the inflector and main magnet fields, showing the field free region through which the beam passes without being deflected. Images reproduced from [41].

'fill'[1]. Further information on the inflector can be found in [41].

3.2 The kickers

The interior volume of the ring through which the muons circulate, the 'storage region', must be free from obstruction. Because of this, the inflector is displaced from the central radius of the storage region, $R_0 = 7112$ mm, by 77 mm. Without intervention, the muons would propagate once around the ring and collide with the inflector. In order to set the beam on a stable orbit, a large radial force must be applied to the beam, a 'kick'. To achieve this, three electromagnetic kickers positioned at 90° from the inflector, denoted by K1 through K3 in Figure 3.20, provide a pulsed magnetic field sufficient to compensate for the initial displacement, centring the beam on R_0. Each kicker consists of two 1.27 m long aluminium plates, which is non-ferric so as not to perturb the magnetic field, positioned inside the storage ring vacuum. They are designed to produce an integrated vertical magnetic field of approximately 1.1 kG-m for a period of 120 ns, covering the full time width of the injected bunch, which dies away before the muons re-enter the kicker aperture following a cyclotron period of 149.2 ns.

The intensity of the kicker pulse with time is given by the black curve in Figure 3.5a, showing how the peak is contained within the cyclotron period, indicated by dashed blue lines. A photograph of a spare set of kicker plates is shown by Figure 3.5a. Detailed discussion on the kicker system can be found in [42].

3.3 The electrostatic quadrupoles

In the ideal case, the kick would set the muons on a perfect orbit, whereby every muon is aligned with the tangent of circle defined by the ideal storage radius, and has an exclusively longitudinal component of momentum which is exactly equal to the magic momentum, 3.094 GeV. In reality, the storage ring possesses a momentum acceptance of $\pm 0.15\%$ about this value [30], as previously noted in Chapter 2 Section 2.4, with momentum components in the radial and vertical directions. Because of this, the beam must be focused in order to prevent beam divergence and complete loss of storage after a few revolutions. The main dipole magnetic field focuses the beam radially[2], while

[1] The initial time of the fill, $t = 0$, is defined by a detector called the 'T0 counter' described in Section 6.1.

[2] The ESQs have a defocusing effect along the radial axis, but combination of electric and magnetic fields is still adequate to provide net focusing.

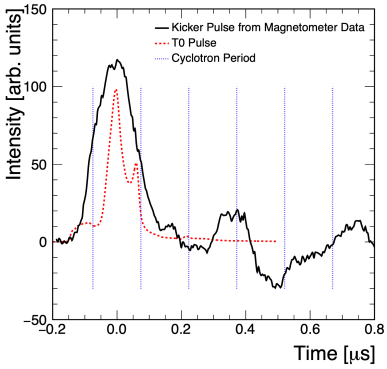

(a) The kicker pulse.

(b) Spare kicker plates.

Figure 3.5: (a) The intensity of the kicker pulse with time, shown by a black curve, where the 120 ns peak is contained within the 149.2 ns cyclotron period, indicated by dashed blue lines; (b) a photograph of a spare set of kicker plates. First image reproduced from [30], second image courtesy of A. P. Schreckenberger [43].

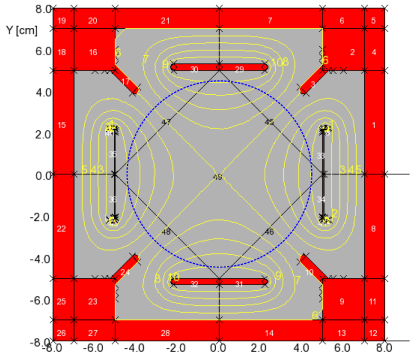

(a) The ESQ field.

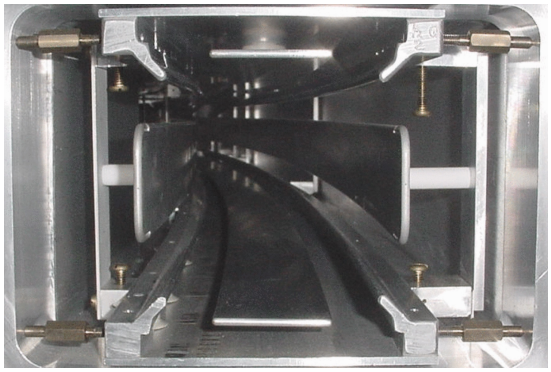

(b) The ESQ plates.

Figure 3.6: (a) A model of the ESQ field, where the yellow curves indicates lines of equal electrostatic potential; (b) a photograph of one set of ESQ plates, viewed from downstream. Images reproduced from [39].

vertical focusing is provided by four in-vacuum electrostatic quadrupoles (ESQs). The ESQs are spaced evenly around the ring, denoted by Q1 through Q4 in Figure 3.20, where they cover 43% of the total azimuth – leaving space for other in-vacuum storage ring components such as the inflector, kickers, and straw tracking detectors. A critical ESQ parameter is the field index, n, which relates the electric field gradient $\kappa = \partial E_y/\partial y$, to the strength of main magnetic dipole field, B_0, given by

$$n = \frac{\kappa R_0}{vB_0} \tag{3.1}$$

where R_0 is the central radius of the storage region and v is the muon velocity [39].

The ESQs also serve the important function of removing improperly stored muons, which are destined to exit the ring before decaying: contaminating the flux of decay positrons falling into the detectors. This process is known as 'scraping', which begins at injection and lasts for 7 µs, after which the ESQs are ramped to their full set-point voltage [30]. The scraping procedure involves charging the ESQ plates with asymmetric voltages to move the beam radially and vertically into five 45 mm radius copper collimators, which scatter muons on the tails of the beam distribution, causing them to lose energy and fall out of the storage region. After a total time of 30 µs after injection, the beam stabilises and the remaining muons are properly stored. Further information on the ESQs can be found in [39].

4 Muon beam dynamics

This section will describe the muon beam dynamics which are relevant to the work presented in this thesis. A more comphrensive review of beam dynamics at E989, as it applies to Run-1, may be found in [30].

4.1 Coherent betatron oscillations

As discussed in Section 3.3, the combination of magnetic and electric fields in ring affect a restoring force on the muon beam in the vertical and radial directions, preventing divergence from the storage region. As a result, the beam undergoes simple harmonic motion in the radial and vertical directions, which may be described by the equations of motion

$$\frac{d^2x}{dt^2} = -\omega_c(1-n)\cdot x, \tag{3.2}$$

$$\frac{d^2y}{dt^2} = -\omega_c n\cdot y, \tag{3.3}$$

where ω_c is the angular cyclotron frequency given by Equation 2.4, and n is the electric field index given by Equation 3.1. In this context, this type of motion is referred to as 'betatron oscillations'. The equations of motion may be solved by substitution of the oscillatory functions

$$x(t) = A_x\cos(\omega_x t - \phi_x), \tag{3.4}$$

$$y(t) = A_y\cos(\omega_y t - \phi_y), \tag{3.5}$$

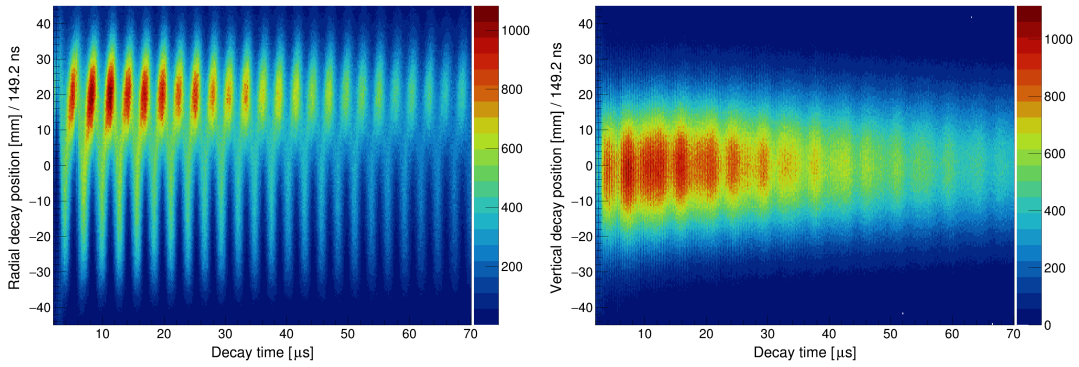

(a) Radial CBO. **(b)** Vertical CBO.

Figure 3.7: Coherent betatron oscillations as measured by the straw trackers described in Section 6.3. The vertical oscillation has an observed frequency which is much higher than its radial counterpart, and so is more difficult to see.

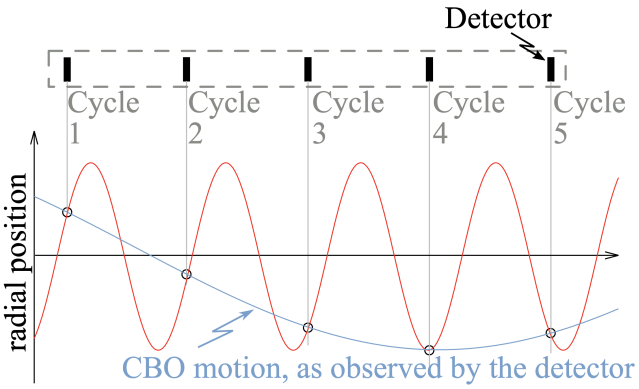

Figure 3.8: The aliasing of the observed frequency of an oscillation. Image reproduced from [44].

giving the betatron frequencies of

$$f_x = f_c \cdot \sqrt{1-n}, \tag{3.6}$$

$$f_y = f_c \cdot \sqrt{n}, \tag{3.7}$$

where $f = \omega/2\pi$.

The muons that comprise the beam share a common phase space distribution following injection and the kick, so that their individual betatron oscillations are coherent: causing the entire beam to move as one. This beam motion is termed 'coherent betatron oscillations' (CBO), shown in Figure 3.7 as measured by the straw trackers described in Section 6.3.

Quantity	Expression	Frequency [MHz]	Time period [μs]
Anomalous precession	f_a	0.229	4.365
Cyclotron	f_c	6.71	0.1492
Horizontal betatron	$f_x = f_c \cdot \sqrt{1-n}$	6.34	0.158
Vertical betatron	$f_y = f_c \cdot \sqrt{n}$	2.21	0.452
Coherent betatron oscillation	$f_{\mathrm{CBO}_x} = f_c - f_x$	0.37	2.703
Vertical waist	$f_{\mathrm{VW}} = f_c - 2 \cdot f_y$	2.31	0.433

Table 3.1: A summary of muon beam oscillation frequencies in the E989 experiment [39]. The values presented here correspond to an n value of 0.108, or a voltage of 18.3 kV, which was used in two of four Run-1 datasets (Run-1a and Run-1d), as detailed in Section 7.

For an oscillation with a frequency f, where f is greater than $f_c/2$ (the Nyquist frequency [45]), the observed frequency of that oscillation will be aliased to the beat frequency $f_c - f$, as explained by Figure 3.8. This is the case with the radial betatron frequency, f_x, which has an observed CBO motion which is much slower than the underlying betatron oscillation, at a frequency

$$f_{\mathrm{CBO}_x} = f_c - f_x. \tag{3.8}$$

One further important oscillation in the average width of the beam, with a frequency of $2 \cdot f_y$, is called the 'vertical waist' (VW). The frequency the VW is aliased to

$$f_{\mathrm{VW}} = f_c - 2 \cdot f_y. \tag{3.9}$$

The EDM search described in this thesis relies on measuring an oscillation in the vertical decay angle modulated at the anomalous precession period, which has a frequency f_a. Both the CBO and VW oscillations occur at higher frequencies than f_a, so must be considered in the analysis. Important beam oscillations at E989 are summarised in Table 3.1. Further information on the CBO and VW can be found in [30] and [44].

4.2 The fast rotation

The rotation frequency of a stored muon is approximately inversely proportional to its equilibrium radius, x_e, which is relative to R_0. This means that, following injection as a bunch, muons at smaller radii will begin to overtake those at greater radii: causing debunching as the beam revolves around the storage ring. This result is a rapid modulation

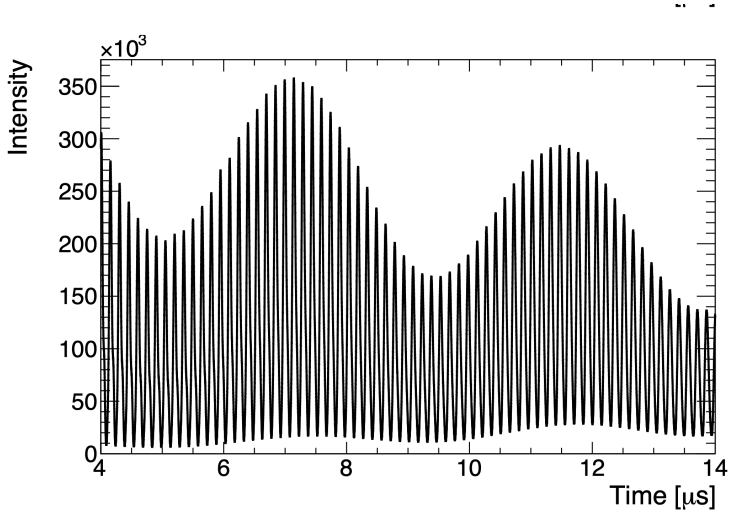

Figure 3.9: The positron number oscillation early in the fill, counted in intervals of 1 ns, showing the rapid oscillation caused by the fast rotation effect. The modulation of the amplitude is caused by ω_a. Image reproduced from [30].

of the cyclotron frequency early in the fill, which largely dies away after 30 µs once the muons are uniformly distributed around the ring. This 'fast rotation' (FR) effect, showing in Figure 3.9, necessitates a correction to ω_a [29], but in the context of the EDM search the fast rotation effect is removed by a combining data in intervals equal to the cyclotron period, T_c, and then applying uniform randomisation of decay times at $\pm T_c/2$ (discussed further Chapter 6 Section 3.4). Further information on the FR can be found in [30, and references therein].

4.3 The distortion of the closed orbit

Local inhomogeneities in the storage ring magnetic field cause the equilibrium radius of the beam to vary as function of ring azimuthal angle, culminating in an effect termed the 'closed orbit distortion' (COD). An illustration of the radial closed orbit is shown in Figure 3.10 [46].

Variations in the vertical electric field, and radial magnetic field, also result in a vertical COD. This effect is highly relevant to the radial magnetic field measurements presented in Chapter 4, and is discussed in detail in Section 3 of that chapter.

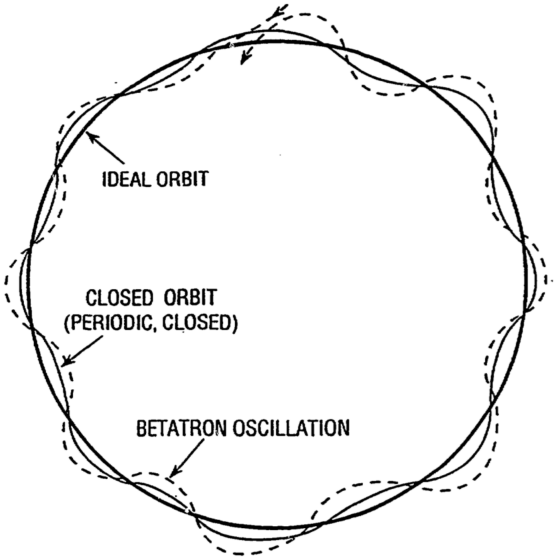

Figure 3.10: An illustration of the radial closed orbit, where the beam equilibrium radius is periodically displaced from the ideal orbit. The horizontal betatron oscillation is also indicated by a dashed line. Imaged reproduced from [46].

5 The magnetic field

The E989 magnetic field system consists of the superconducting magnetic storage ring (referred to here as the 'main magnet'), a suite of NMR probes used to map the magnetic field, and an array of passive and active of shims used to reduce inhomogeneities in the field. The system is designed to produce a vertical magnetic field of 1.45 T, with uniformity of 1 part-per-million (ppm) around the full azimuth of the muon storage region.

The main magnet, originally designed and built for the E821 $g-2$ experiment at BNL, is a continuous ring of low-carbon steel which is excited by superconducting coils to generate a magnetic field. Twelve flux return yokes, each covering a 30° azimuthal section, are fixed together to form a ring approximately 15 m in diameter and 3 m high, with a mass of 680 metric tons. Each yoke has a 'C-shaped' cross-section, illustrated by Figure 3.11, which partially encloses the muon storage region, and allows decay positrons to exit the field in the direction of the ring interior.

Magnetic flux is induced in the yokes by three superconducting niobium-titanium (NbTi) coils connected in series, which carry a ∼5170 A current from a 5 V power supply. There is one outer coil and two inner coils, positioned on either side of the

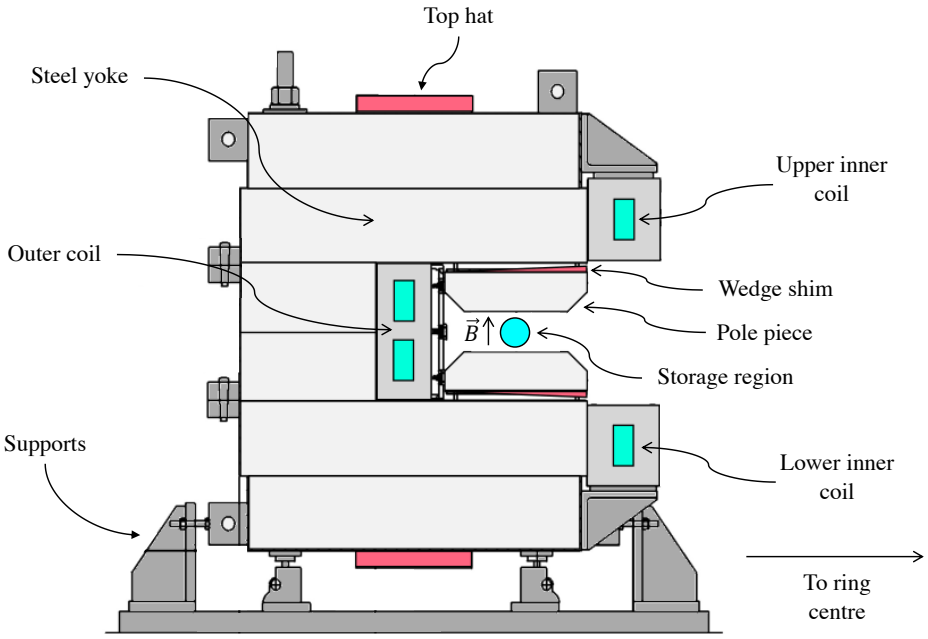

Figure 3.11: A cross-section of the E989 main magnet, showing: the 'C-shaped' yoke, superconducting coils (green), pole pieces, shims (red), and muon storage region (blue). The orientation of the magnetic field in the storage region is indicated by an arrow. Not shown are the additional passive shims, and the surface correction coils (active shims), fixed to the inner surfaces of the pole pieces. Image adapted from Figure 2 of [47], and inspired by Figure 2.4 of [48].

equilibrium radius of the storage region, $R_0 = 7112$ mm, at radii of 6677 mm and 7512 mm respectively. The outer coil, consisting of 48 turns with a gap at the mid-plane to allow space for the inflector, drives the field across the storage region; the two inner coils, consisting of 24 turns each, are supplied with a current in the opposing direction to the outer coil, cancelling the flux in the ring centre and improving the quality of the field in the storage region. The coils are typically operated at temperature of 5 K, which is maintained by a supply of cryogenic helium.

The dipole field across the storage region is shaped by sections of higher quality steel called 'pole pieces'. The pole pieces are isolated from the magnet bulk an air gap of 1.5 cm, decoupling the field across the storage region from aberrations in the yoke and producing a highly uniform field. The air gap also allows space for steel wedges to be inserted, which, along with larger sections of steels fixed to the top and bottom of the yoke called 'top hats', improve uniformity of the field by passive shimming. Additional 'edge shims' on the inner surfaces of pole pieces, as well as iron foil laminations, fine-tune

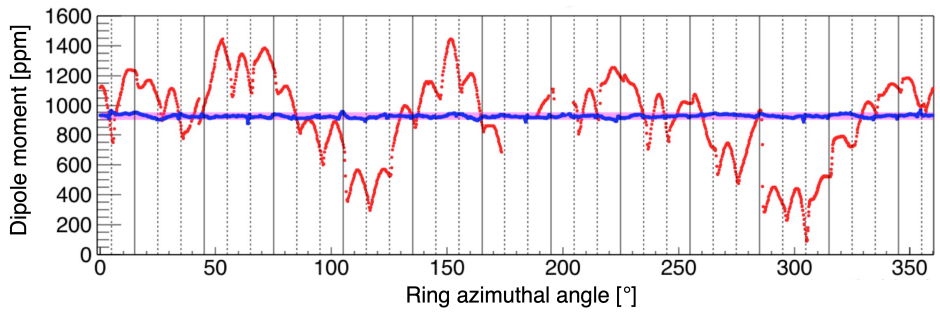

Figure 3.12: The dipole magnetic field measured around the ring before the shimming campaign in 2015-2016 (red) and after (blue), where variations in the field were reduced to ∼100 ppm. Image adapted from [50].

the field uniformity even further. The process of mechanically shimming the magnetic field was carried out during the E989 commissioning period in 2015-2016, reducing variations in the field to within ∼100 ppm, as shown in Figure 3.12. Detailed discussion of the shimming campaign can be found in [49].

The azimuthally averaged variations in the field are finally brought to within ∼1 ppm by the active shimming provided by sets of 100 concentric current-carrying coils, which are printed on circuit boards and fixed to the inner surface of the each pole piece. The currents carried by these 'surface correction coils' (SCCs), may be adjusted during operation by input in the stand-alone magnetic field DAQ system. This utility of this subsystem, beyond shimming the magnetic field, will be demonstrated in Chapter 4.

Finally, the muon storage region is enclosed in an aluminium vacuum chamber, in order to both prevent the beam from scattering off air molecules and to minimise the likelihood of discharge from any of the various high voltage systems inside the ring. Detailed discussion on the main magnet can be found in [39] and [47].

The magnetic field is measured by 378 fixed NMR probes attached to the top and bottom of the vacuum chamber, called 'fixed probes', and a mobile array of 17 NMR probes which periodically transits the full circumference of vacuum chamber in a device called the 'trolley'. Each probe contains a sample of a proton rich organic substance (petroleum jelly), where the Larmor precession frequency of the protons in the substance is proportional to the strength of the field. The probes are calibrated by comparison with measurements taken with a device termed the 'plunging probe', which contains a sample of well-characterised high purity water. The fixed probes provide a means of measuring the field drift while the experiment is receiving beam, while the trolley

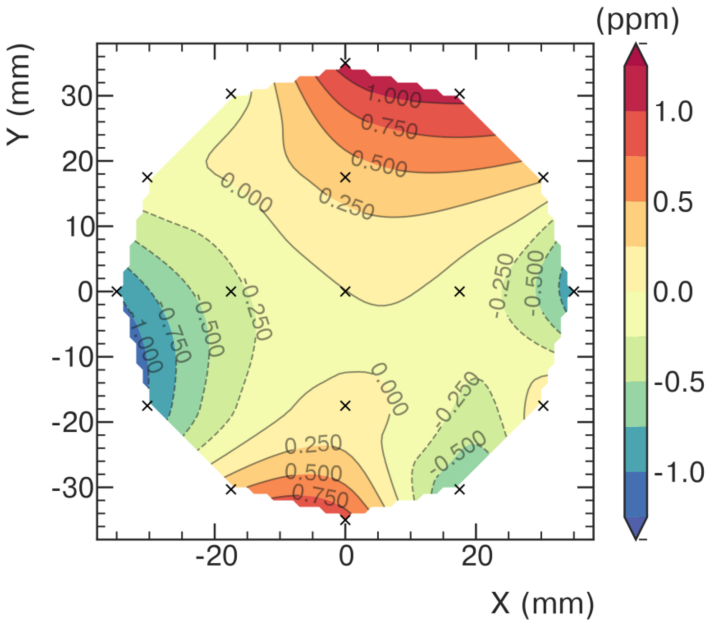

Figure 3.13: An azimuthally averaged field map of the storage region, constructed from data taken from a single trolley NMR probe. Variations in the magnetic field are within the target ∼1 ppm. Image reproduced from [33].

is used to build precision maps the field from several thousand points around the ring during dedicated beam-off periods called 'trolley runs', which take place every three days. An example of an azimuthally averaged field map produced by a single trolley probe is shown in Figure 3.13. The field maps from the trolley are weighted with maps of the spatial beam distribution measured by the straw tracking detectors, discussed in Section 6.3, in order to measure the average magnetic field experienced by the muons at the time of decay.

6 Detectors

6.1 Auxiliary detectors

The auxiliary detectors are distinct from the calorimeters and straw tracking detectors, which are discussed in the following sections, in that their function relates to making direct measurements of the muon beam in order to monitor injection and study beam dynamics, rather than detecting decay positrons.

Three systems fall into this category, the first being the 'T0' counter: a scintillating paddle connected to two photomultiplier tubes (PMTs), positioned outside the ring and

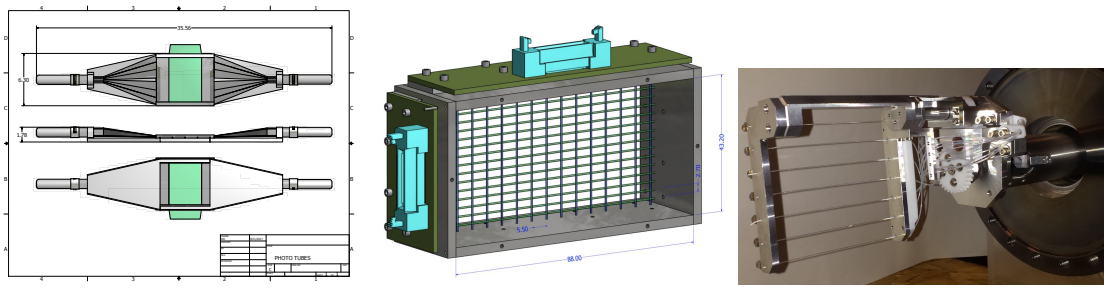

(a) T0 **(b)** IBMS **(c)** Fibre harp

Figure 3.14: Representations of the E989 auxiliary detector systems, showing: (a) a schematic of the T0 counter, showing the scintillator (green) attached to PMTs on the left and right; (b) a computer model of one the IBMS detectors (IBMS1), showing the grid of scintillating fibres connected to SiPMs; (c) a photograph of one of the four fibre harps, showing the scintillating fibres (horizontally aligned in this case) mounted on a retractable arm. Images reproduced from [51], [52], and [53].

upstream of the inflector. The primary function of the T0 is to define the initial time of the fill, $t = 0$, which is essential for the synchronisation the various systems in the ring [51]. The second auxiliary detector is the 'inflector beam monitoring system' (IBMS): grids of scintillating fibres connected to silicon photomultipliers (SiPMs), positioned at two locations upstream of the inflector. The IMBS measures the spatial distribution of the muons before injection, providing the valuable diagnostic information required for optimally directing the beam through the narrow inflector aperture. An additional IBMS detector with horizontal fibres only may be inserted downstream of the inflector to make a destructive measurement of the vertical beam profile [52]. The third of these systems are the 'fibre harps', which were recovered from the E821 $g-2$ experiment and refurbished for use in E989. These are retractable 'harps' of scintillating fibres, which can be inserted inside the vacuum chamber at approximate ring azimuthal angles of 180° and 270°. Two detectors are positioned at each location, one with horizontally aligned fibres and another with vertically aligned fibres. While inserted, the fibre harps are used to make a destructive measurement of the spatial distribution of the beam, serving as a means of directly measuring effects such as the horizontal and vertical CBO during dedicated systematic runs. More information on the fibre harps may be found in [39].

6.2 Calorimeters

The primary means of positron detection at E989 are the twenty-four electromagnetic calorimeters which instrument the interior the ring, indicated by numbers 1 through 24

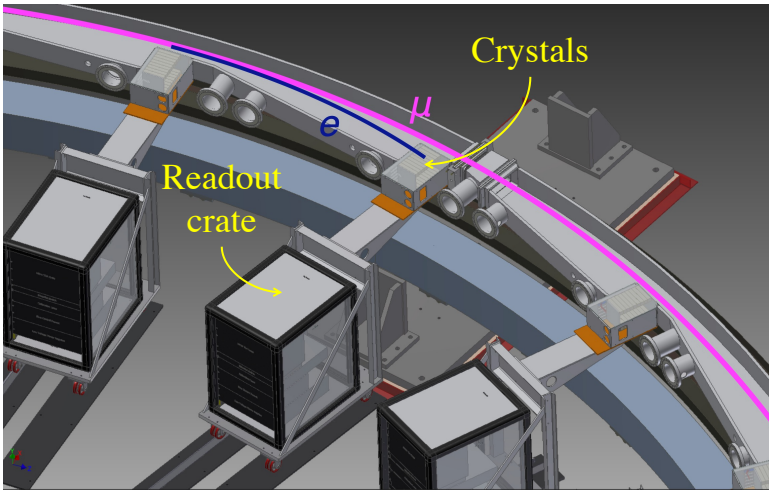

(a)

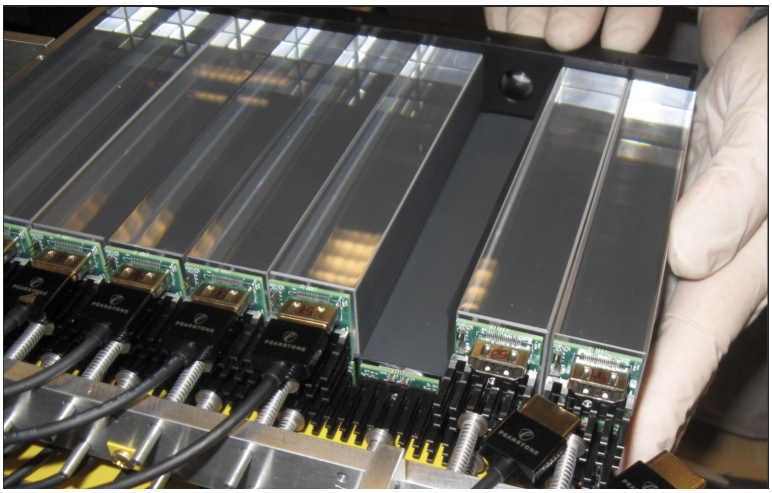

(b)

Figure 3.15: The E989 calorimeters, showing: (a) a model of three calorimeters in position during operation, with an incident decay positron indicated by a blue line; (b) a photograph of the $PbFl_2$ crystals and SiPMs during assembly. Images reproduced from [54].

in Figure 3.20. The purpose of the calorimeters is to measure the energy, arrival time, and (to a lesser extent) the hit position of decay positrons.

Unlike the E821 calorimeters, which had a monolithic construction, the E989 calorimeters are composed of a segmented 9-wide $\times$ 6-high array of lead-fluoride ($PbFl_2$) crystals, a each with a volume of $25 \times 25 \times 140$ mm^3. Behind every crystal is a silicon photomultiplier (SiPM), which senses the Cherenkov light produced by relativistic charged particles passing through the crystal medium. The intensity of the light falling onto the SiPMs is proportional to the incident positron energy. Each crystal is isolated from its neighbours by a thin opaque and non-reflective wrapping, black Tedlar foil, which greatly limits the

level of light transmitted between crystals: improving the spatial resolution of detected hits. The calorimeters are spaced evenly around the ring, each positioned immediately downstream of an extruded section of the vacuum chamber – allowing decay positrons to travel with minimal energy loss before exiting the vacuum and being intercepted. Frontend electronics for each calorimeter are housed in a crate positioned away from the magnetic field region. A illustration of the calorimeters in position relative to the vacuum chamber is shown in Figure 3.15a, and a photograph of the $PbFl_2$ crystals is shown in Figure 3.15b.

The calorimeter temporal resolution exceeds 100 ps for positrons with a kinetic energy greater than 100 MeV, as specified by the design requirements [39], aided by the short and fast signal produced by Cherenkov radiation. This requirement is motivated by the need to resolve pileup events, where two or more hits close in time and space are erroneously reconstructed as a single hit. Pileup, if unresolved, changes the number of positrons detected 'above threshold' in the ω_a number oscillation. Pileup is more prominent early in the fill, causing an apparent time dependence in the phase of ω_a. The requirements of the energy resolution of the calorimeters are less stringent, at better than 5% at 2 GeV, since the ω_a measurement only uses the hit cluster energy as means of event selection rather than as a direct observable.

An additional requirement on the calorimeters is that variations in the energy response, or gain, must fall within 0.1% per 200 µs. Much like pileup, changes in gain can bias ω_a between early and late times in the fill. To monitor this, a system of lasers periodically fire pulses of light into the crystals, allowing for 'in-fill' gain variations to be corrected by directly comparing the detected energy to the energy deposited by the laser. The laser monitoring system may also be used to detect gain variations fill-by-fill, as well as to measure the SiPM time resolution by firing two pulses in quick succession. Detailed discussion on the calorimeters may be found in [39] and [55].

6.3 The straw trackers

The straw trackers, or trackers, are a secondary system of positron detectors which are designed to make a non-destructive measurement of muon beam profile, reconstructing both the decay position and momentum of particles exiting the storage region as a function of time.

The information provided by the trackers is extremely valuable for a numbers of

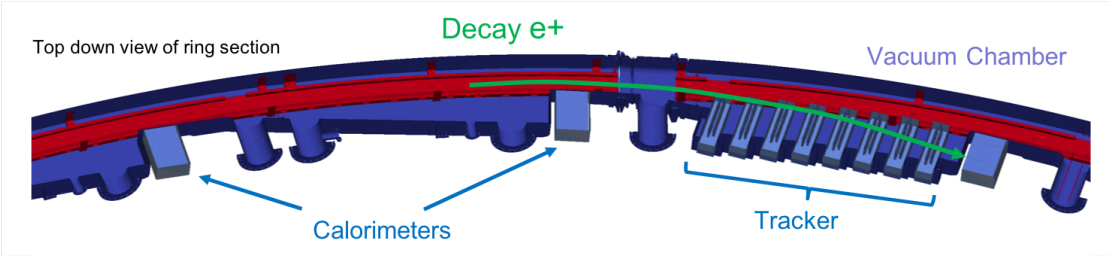

Figure 3.16: A rendering of the tracker modules in position inside the vacuum chamber, shown with respect to nearby calorimeters. The trajectory of a decay positron is shown in green, illustrating the case where a track may be matched with a calorimeter cluster. Image courtesy of the E989 collaboration.

reasons. Firstly, it enables the precise characterisation of beam dynamics effects such a betatron motion, described in Section 4, minimising the associated systematic uncertainty on ω_a. Secondly, and as discussed in Section 5, tracker measurements of the spatial beam distribution are used to weight the field maps measured by the trolley NMR probes, which is essential for the final determination of the magnetic field. Thirdly, positron trajectories may be extrapolated both backwards to the point of decay, or forwards to the downstream calorimeter: enabling direct comparison between tracker hits, hereafter referred to as 'tracks', and calorimeter clusters. This 'tracker-calorimeter matching' is extremely useful for cross-checks of pileup and gain variations[3]. Finally, the trackers' ability to measure the time evolution of the average positron vertical decay angle is central to the muon EDM search described in this thesis.

There are two tracker stations, referred to as stations 12 and 18[4] in this thesis (indicated by T1 and T2 in Figure 3.20), positioned at approximately 180° and 270° around the ring. Each station is composed of a row of eight modules which are inserted into the vacuum chamber. The individual modules consist of four layers of 32 Mylar tubes, called straws, which are fixed to aluminium manifolds. The straws are 5 mm in diameter, 10 cm in length, and have a wall thickness of 15 µm. Each straw encloses an atmosphere of equal parts argon and ethane, at a pressure of 1 atm, at centre of which is a 25 µm diameter gold-plated tungsten sense-wire held at a positive potential difference of 1.65 kV. The sense-wire acts as an anode and the electrically grounded straw walls acts as a cathode, resulting in a strong radial electric field around the wire.

[3] A study utilising tracker-calorimeter matching (conducted by the author), where the ratio of cluster energy to track momentum was used to verify gain measurements made by the laser monitoring system, can be found in [56].

[4] Named after the numbering of the extruded vacuum chamber sections shown in Figure 3.20, counting from zero.

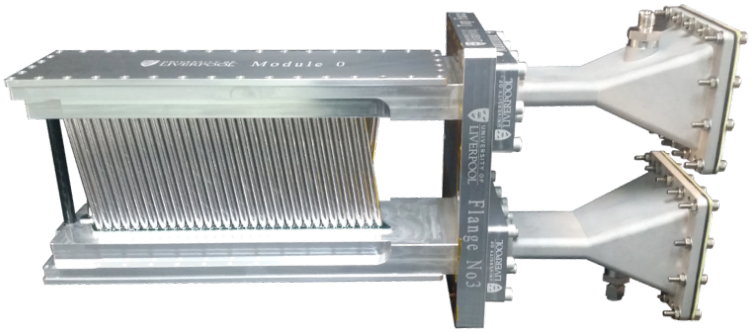

(a)

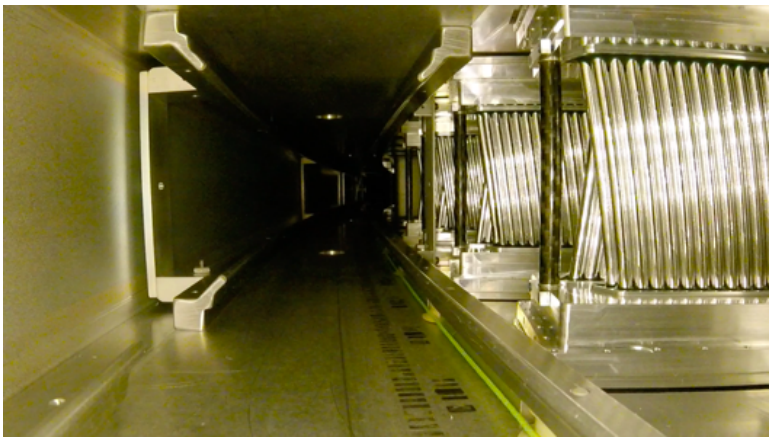

(b)

Figure 3.17: Photographs of the straw trackers, showing: (a) an individual module, with two of the four layers Mylar straws visible; (b) a photograph taken from the interior of the vacuum chamber, showing a tracker station from the perspective of the muon beam. Images courtesy of the E989 collaboration.

When a positron traverses the interior of a straw it creates a trail of primary ionisation products (electrons and positive ions) in its wake. Compelled by the electric field, the electrons drift towards the wire, creating an avalanche of secondary ionisation products in the process, and cause an accumulation of charge on the wire which is registered as a hit. Meanwhile, the positive ionisation products are neutralised by the straw walls. Straw layers are alternately orientated at $\pm 7.5°$ from the vertical, labelled U and V layers, enabling the vertical component of positron trajectory to be measured. The components of the trackers are constructed from non-magnetic materials so as not to perturb the magnetic field, and extensive leak testing was carried out to ensure that the tracker gas does not disturb the storage region vacuum [57]. Photographs of the tracker modules are shown in Figure 3.17, and a rendering of the arrangement of modules relative to the vacuum chamber, and downstream calorimeter, can be found in Figure

3.16. Further discussion on the tracker design and performance can be found in [58].

Tracks as formed by first grouping straw hits into 80 ns windows, which is less than the maximum drift time within a straw, to create 'time islands'. Within the time island, hits are clustered by UV layer into singlets and doublets, e.g., if there are hits in both layers then the cluster is a doublet. Neighbouring clusters are then grouped together to form 'track candidates'. Next, the correlation between drift times in adjacent layers is used to calculate an initial time, t_0, from which the drift times of individual hits are calculated. Using a calibrated relationship between drift time and distance, the 'distance of closest approach' (DCA) of a positron to the sense wire is then calculated for each hit. Track fitting is then performed on candidates using a `GEANE` (Geometry and Error Propagation) [59] based χ^2 minimisation algorithm developed by N. Kinnaird [60].

In order to characterise positron parameters at the muon decay point, such as the decay angle, tracks are extrapolated backwards, through a region of varying magnetic field, using method developed by S. Charity [57]. This method relies on a Runge-Kutta-Nyström algorithm [61] to find the point of radial tangency, or the point where the radial component of momentum is zero, which is considered to be a reliable estimate of the decay point. The resolution of track extrapolated parameters is discussed, in the context of the muon EDM search, in Chapter 6 Section 3.6.

Finally, cuts are imposed on the parameters of tracks and extrapolated vertices in order to obtain a sample of what are referred to in this thesis as 'quality tracks', or 'quality vertices'. An example of a track-level quality requirement is that the track fit has a p-value of > 0.05, and an example of a vertex-level quality requirement is that the positron does not scatter through a large volume of material before detection [62].

7 Measurement periods

At the time of writing, E989 is nearing the end of its fifth data-taking period, called 'Run-5'. The work presented in this thesis is primarily focused on an analysis of Run-1 data, supported by radial magnetic field measurements carried out in Run-4 (described in Chapter 4). Run-6, which may involve running with μ^- as opposed to μ^+, is likely to take place in 2022/2023. The total number of measured positrons over time is expressed in terms of the fraction of the BNL E821 cumulative dataset in Figure 3.18, where the E989 raw integrated dataset is presently a factor of $\sim$18 times larger than that of E821.

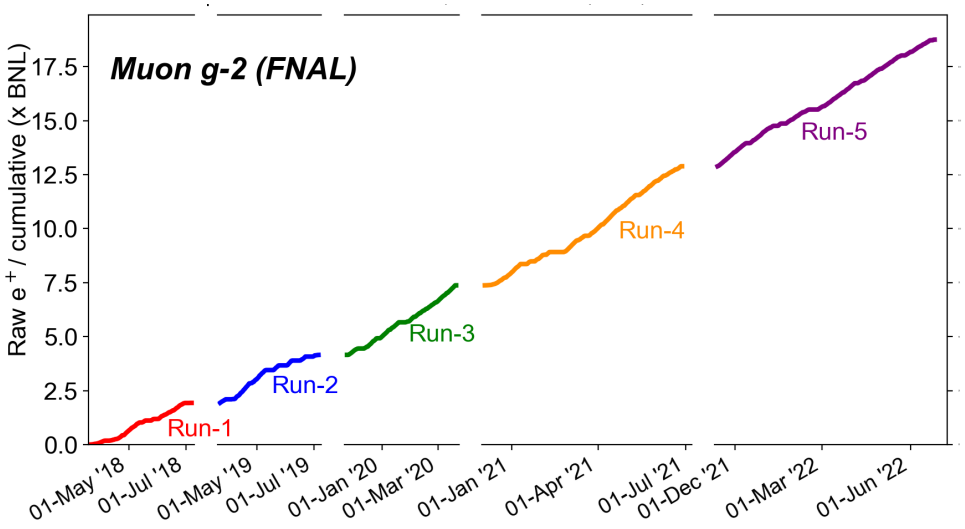

Figure 3.18: The raw integrated E989 dataset at the time of writing, expressed as fraction of the BNL E821 cumulative dataset. Image courtesy of M. Lancaster.

Dataset	Quality tracks	Quality vertices	ESQ field index, n	ESQ voltage [kV]
Run-1a	3.54×10^7	1.81×10^7	0.108	18.3
Run-1b	4.86×10^7	2.49×10^7	0.120	20.4
Run-1c	7.28×10^7	3.71×10^7	0.120	20.4
Run-1d	1.41×10^8	7.22×10^7	0.108	18.3
Total	2.98×10^8	1.52×10^8	–	–

Table 3.2: The numbers of high quality tracks and extrapolated track vertices for each Run-1 dataset, along with the ESQ field indices and corresponding voltages.

Run-1 is divided into four datasets, labelled '1a' through to '1d'. The statistical precision of the muon EDM search presented in Chapter 6 is governed by the numbers of quality-cut-passing tracks and extrapolated track decay vertices per Run-1 dataset, which are summarised in Table 3.2. Also included are the ESQ field indices, and corresponding voltages, which are relevant to the radial magnetic field analysis detailed in Chapter 4.

8 Overview of computing

The computing framework at E989 is split between an online data acquisition (DAQ), and offline data processing and simulation. The `MIDAS` [64] based DAQ system handles the exceptionally high rate of raw data produced by the experiment while receiving

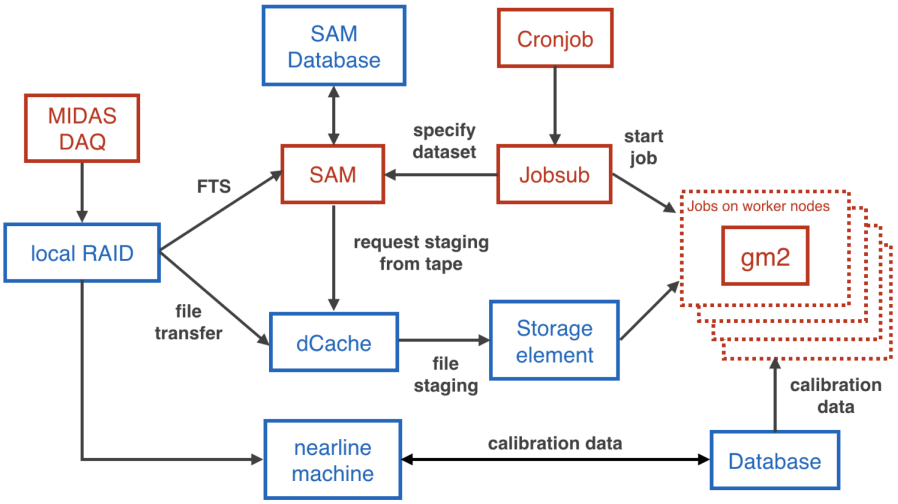

Figure 3.19: A diagram illustrating the flow of data at E989, from the acquisition of raw data to high level analysis. Image reproduced from [63].

beam (∼20 GB/s) – predominantly from 1296 calorimeter channels (54 channels per calorimeter). After receiving triggers from the accelerator complex, the DAQ system processes the raw calorimeter data into 'derived datasets' (such as islands of digitized pules) with 28 NVIDIA *K40* GPUs working in parallel, writing binary files in `MIDAS` format to temporary storage on local RAID array, after which they are transferred to tape for permanent on-site storage using the `dCache` system at a much reduced rate of ∼200 MB/s. The experiment also utilises a data quality monitor (DQM), which reconstructs a subset of the data, providing live feedback as to the status of the experiment during operation. In addition, high level `ROOT` [65] histograms and `Ntuples` are produced on a multi-core nearline (NL) machine, writing output to a local disk which may be accessed by users via a web server. Once written to tape, the data is fully reconstructed and organised into datasets using the sequential access via metadata (SAM) [66] cataloguing service. This in an automated procedure called 'data production', which relies heavily on grid computing: a combination of FermiGrid [67] and Open Science Grid [68]. For simulation, E989 employs a `GEANT4` [69] based model of the storage ring and detector systems called `gm2ringsim`. Event processing, both for data and simulation, is handled by use of Fermilab's `C++` based `art` framework [70]. A diagram illustrating the flow of data in at E989 is given in Figure 3.19. Further information on E989 computing can be found in [71].

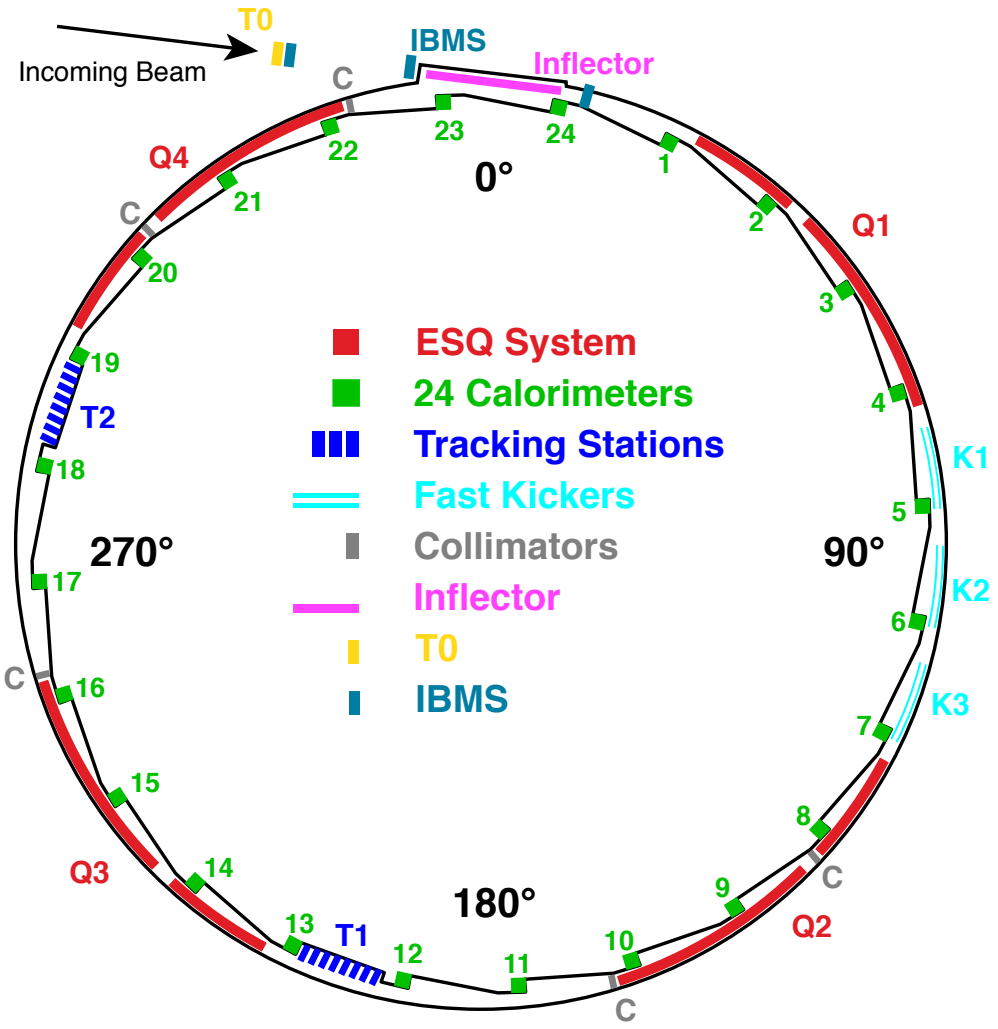

Figure 3.20: A schematic of the E989 storage ring, illustrating the various components discussed in this chapter. Image reproduced from [30].

Chapter 4

The radial magnetic field

The E989 main magnet is designed to produce a 1.45 T vertical dipole magnetic field which is precisely measured by use of a suite of NMR probes, as described in Chapter 3 Section 5. Components of the field in the radial, B_x or B_r, and longitudinal, B_z, directions can make ppm-level contributions to the total field, which are not usually measured at E989. In the context of the muon EDM search described in this thesis, the radial magnetic field component, hereafter referred to as 'the radial field', can tilt the muon spin precession plane in a manner consistent with a non-vanishing muon EDM; which could obfuscate a genuine signal. This makes the radial field a potentially limiting source of systematic uncertainty in the search for d_μ, which must be precisely characterised. In this chapter, the development and execution of a novel technique for measuring the radial field to a precision of < 1 ppm will be described, and the results of measurements performed in Run-4 will be shown. Additionally, a method for extrapolating the results of these measurements as a means of estimating the average radial field, $\langle B_r \rangle$, in any E989 dataset, including Run-1, will be presented.

1 The significance of the radial field

The existence of non-zero field components besides the vertical has significance to both the measurement of a_μ and the search for a muon EDM. In the case of a_μ, B_x (B_r) and B_z can modify the anomalous precession frequency, ω_a, by

$$\vec{\omega}_a = a_\mu \frac{e}{m_\mu} \vec{B} = a_\mu \frac{e}{m_\mu} (B_x \hat{x} + B_y \hat{y} + B_z \hat{z}). \tag{4.1}$$

In the case the EDM, both B_r and B_z result in a tilted muon spin precession plane, with B_z causing a longitudinal tilt and B_r a radial tilt, as illustrated in Figure 4.1. Both manifest as an oscillation in the average vertical muon decay angle, $\langle \theta_y \rangle$. In the context

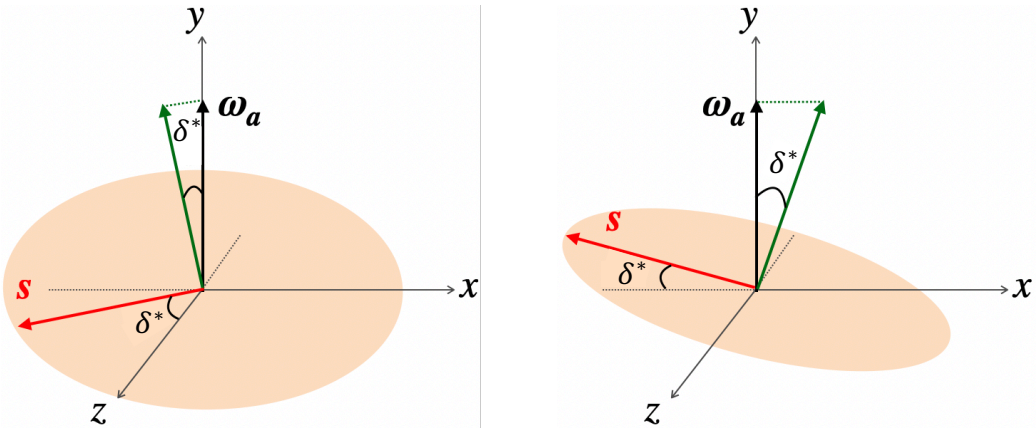

(a) Longitudinal field. **(b)** Radial field.

Figure 4.1: The tilt in muon spin precession plane resulting from: (a) a non-zero longitudinal field component; (b) a non-zero radial field component. Note that the radial field results a tilt in same direction as would be caused by a muon EDM, as shown in Figure 2.7b. Images courtesy of R. Chislett [35].

of a vertical decay angle based muon EDM search, such as described Chapter 2 Section 3.3, the oscillation produced by B_z is in-phase with ω_a and is therefore absorbed by the cosine term in the vertical angle fit function given by Equation 2.33. Conversely, the oscillation associated with B_r is in-phase with $\omega_\eta - \pi/2$ out-of-phase with ω_a – which is consistent with a signal from a non-zero EDM. This means that the radial field can effectively mimic an EDM at E989, and therefore constitutes a potentially limiting source of systematic uncertainty. Because of this, B_r must be precisely measured before a muon EDM search is undertaken.

2 The required precision of a radial field measurement

The required precision of a radial field measurement is governed by the statistical limit for sensitivity to an EDM signal. For any finite dataset, the statistical uncertainty will at some point overcome the systematic uncertainty caused by a radial field. At this point, no improvement in the total uncertainty can be made by improving the uncertainty on the radial field. Examples of the statistically limited EDM sensitivity against the radial field uncertainty are illustrated in Figure 4.2, courtesy of D. Vasilkova [72]. The case for a muon EDM measurement made using a dataset of one hundred million high quality tracks, approximately comparable to the size of the Run-1 dataset, is shown in

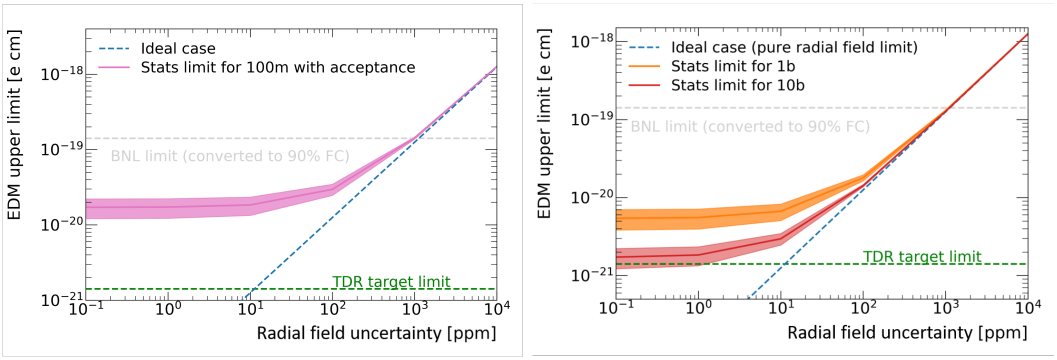

(a) One hundred million tracks. **(b)** One and ten billion tracks.

Figure 4.2: The upper limit on a muon EDM versus the uncertainty on a radial field measurement for: (a) one hundred million tracks, which is comparable to the E989 Run-1 dataset; (b) one to one hundred billion tracks, which is comparable to the target integrated dataset. For Run-1, the target precision for a radial field measurement is ≤ 10 ppm, while for the integrated dataset it is ≤ 1 ppm. Images courtesy of D. Vasilkova [72].

Figure 4.2a. This indicates that the radial field uncertainty for an EDM search in Run-1 must be ≤ 10 ppm. For the integrated E989 dataset, consisting of billions of tracks, a precision of ≤ 1 ppm is required, as shown in Figure 4.2b.

3 The distortion of the vertical closed orbit

A radial field would not only produce a tilt in the spin precession plane, but would also modify the average vertical beam position, $\langle y \rangle$, due to the Lorentz force. Counteracting this effect is vertical electric field from the ESQs[1], which pushes the beam back towards the centre of the storage region so that an equilibrium position is reached. The resulting value of $\langle y \rangle$ depends on the size of the vertical ESQ potential difference, V, and B_r. The interaction between V, B_r, and $\langle y \rangle$ is central to the work presented in this chapter, as it may be exploited to make a measurement of B_r.

The interplay between the radial field and the ESQs is referred to as the distortion of the vertical closed orbit[2] due to a magnetic skew dipole [73], and is described by the summation

$$y(\theta) \approx \sum_{N=0}^{\infty} \frac{R_0}{B_0} \frac{(B_{rcN}\cos(N\theta) + B_{rsN}\sin(N\theta))}{N^2 - n}, \tag{4.2}$$

where θ is the azimuthal angle around the ring, R_0 is the ideal storage radius (7112 mm),

[1]The electrostatic quadrupoles, introduced in Chapter 3 3.3.
[2]The distortion of the closed orbit having been introduced in Chapter 3 Section 4.3.

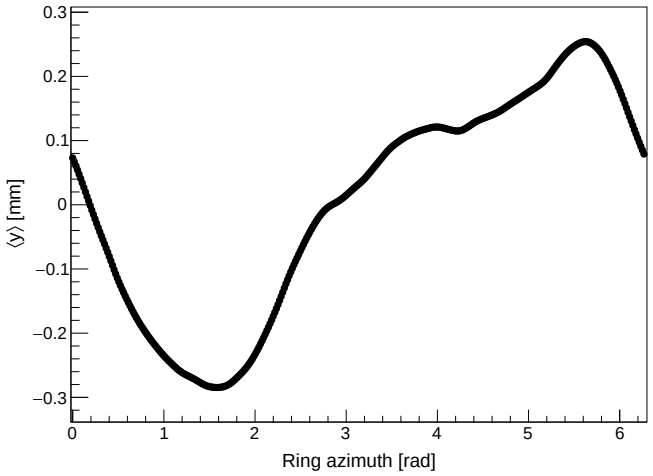

Figure 4.3: The variation in average vertical beam position as a function of ring azimuthal angle, from a simulation of the distortion of vertical closed orbit due to a magnetic skew dipole. Simulation data courtesy of D. Tarazona [74].

B_0 is the dominant vertical magnetic dipole field, the $B_{rs,c}$ terms represent orthogonal components of the radial magnetic field, and n is the ESQ field index, given by Equation 3.1. For illustration, the simulated variation in $\langle y \rangle$ as a function of ring azimuth is shown in Figure 4.3. Expanding Equation 4.2 gives

$$y(\theta) \approx \frac{R_0}{B_0}\left[-\frac{B_{r,N=0}}{n} + \frac{B_{r,N=1}\cos(\theta-\phi_1)}{1-n} + \frac{B_{r,N=2}\cos(2\theta-\phi_2)}{4-n} + ...\right], \tag{4.3}$$

where the phase shifts, ϕ_N, are introduced by the absorption of the sine terms. The $N > 0$ terms cancel when $\langle y \rangle$ is observed simultaneously around the ring, which in practice means taking the average position as measured over all calorimeters; a technique described in detail the following section. In this case, only the $N = 0$ term remains, leaving the linear relationship

$$\langle y \rangle = \frac{R_0}{vB_0}\frac{\langle B_r \rangle}{n} = \frac{\langle B_r \rangle}{\kappa}. \tag{4.4}$$

Furthermore, since κ is proportional to V, the above expression may be simplified to give the relationship

$$\langle y \rangle \propto \frac{\langle B_r \rangle}{V}, \tag{4.5}$$

which is central to the measurements presented in this chapter.

As an additional detail, simultaneously measuring $\langle y \rangle$ around the full ring azimuth

also simplifies the influence of an additional distortion arising from misalignment of the ESQs. This phenomenon is referred to as the distortion of the vertical closed orbit due to an electric skew dipole, and is described, in a manner similar to Equation 4.2, by

$$y(\theta) \approx \sum_{N=0}^{\infty} \frac{R_0}{cB_0} \frac{(E_{ycN}\cos(N\theta) + E_{ysN}\sin(N\theta))}{N^2 - n}, \tag{4.6}$$

where $R_0/cB_0 = n/\kappa$ by Equation 3.1. If the $E_{yc,s}$ terms arise from ESQ misalignment then they will scale with V, as will κ. This makes the ratio E_y/κ a constant. Expanding the summation, absorbing the sine terms with phase shifts as with Equation 4.3, and defining $E_y/\kappa{=}E'_y$ gives

$$y(\theta) \approx -E'_{y0} + \frac{n}{1-n}E'_{y1}\cos(\theta - \phi_{E,1}) + \frac{n}{4-n}E'_{y1}\cos(2\theta - \phi_{E,2}) + ... \tag{4.7}$$

As with Equation 4.3, the $N > 0$ terms cancel when taking the average $\langle y \rangle$ around the full ring azimuth, leaving the constant $-E'_{y0}$. Importantly, this means that the dependence of the ring average $\langle y \rangle$ on V has no contribution from ESQ misalignment, and is driven exclusively by $\langle B_r \rangle$, according to Equation 4.5.

4 Measurement technique

4.1 Measuring the background radial field

The average radial field, $\langle B_r \rangle$, has two contributions: the average field applied by the surface correction coils (SCCs)[3], $\langle B_r^a \rangle$, and an unknown average background field, $\langle B_r^b \rangle$, so that

$$\langle B_r \rangle = \langle B_r^a \rangle + \langle B_r^b \rangle. \tag{4.8}$$

In the case where the total field is zero, $\langle B_r^b \rangle$ must be equal in magnitude and opposite in sign to $\langle B_r^a \rangle$, which is a known quantity, as follows

$$\langle B_r \rangle = 0 \rightarrow \langle B_r^a \rangle = -\langle B_r^b \rangle. \tag{4.9}$$

The challenge is then to find the point at which $\langle B_r \rangle = 0$. Following the relationship given by Equation 4.5, this is possible by performing a series of ESQ scans of V over a

[3]The SCCs are described in detail in Chapter 3 Section 5.

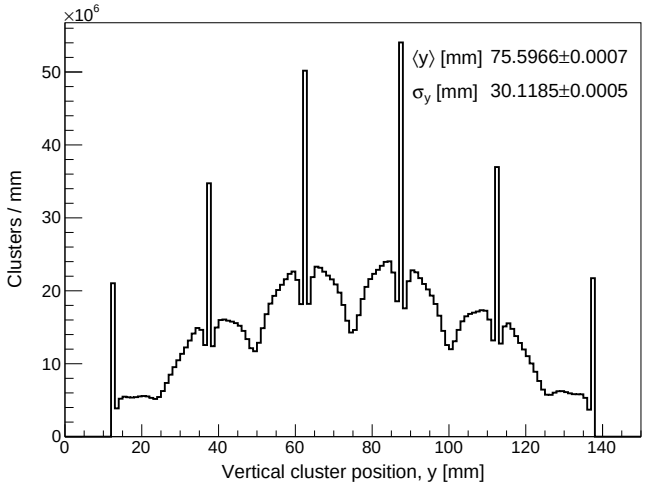

Figure 4.4: The distribution of vertical cluster positions for all calorimeters in the Run-1a dataset, where the mean, $\langle y \rangle$, is taken as a proxy for the ring average vertical beam position. The peaks in the distribution correspond to clusters where a single crystal was hit.

range of SCC $\langle B_r^a \rangle$ values, measuring the ring average $\langle y \rangle$ by taking the mean vertical hit position as measured by all calorimeters at each set point. Calorimeter hit position is often referred to as 'cluster position' in E989, and is calculated by taking an energy weighted average of the central positions of crystals in cluster of hits. Detailed discussion on the formation of calorimeter clusters and the calculation of cluster position may be found in [75]. An example of the distribution for vertical cluster positions, in this case for the Run-1a dataset, is given by Figure 4.4.

This technique is most easily described with the aid of a toy model of the measurement, summarised in Figure 4.5. In this example, there is an injected $\langle B_r^b \rangle$ of 8 ppm, twenty four set-points, an inputted statistical uncertainty on $\langle y \rangle$ drawn from Run-1 data (discussed further Section 4.2). Uncertainties associated with V and B_r^a are, at present, neglected in the work presented in this chapter; however, current best estimates give small uncertainties of $\sim$0.1 kV and $\sim$3% respectively [76][77]. Figure 4.5a illustrates the ESQ scans of V, and Figure 4.5b demonstrates how the gradients of linear fits made to those scans, which are proportional to the $\langle B_r \rangle$ by Equation 4.5, vary with $\langle B_r^a \rangle$. The point at which $\langle B_r \rangle = 0$ is found by evaluating a linear fit to this secondary plot, where $\langle B_r^b \rangle$ is equal in magnitude and opposite in sign to the x-intercept of the fit. If the parameters of this fit consist of a gradient m and a y-intercept c, then the uncertainty

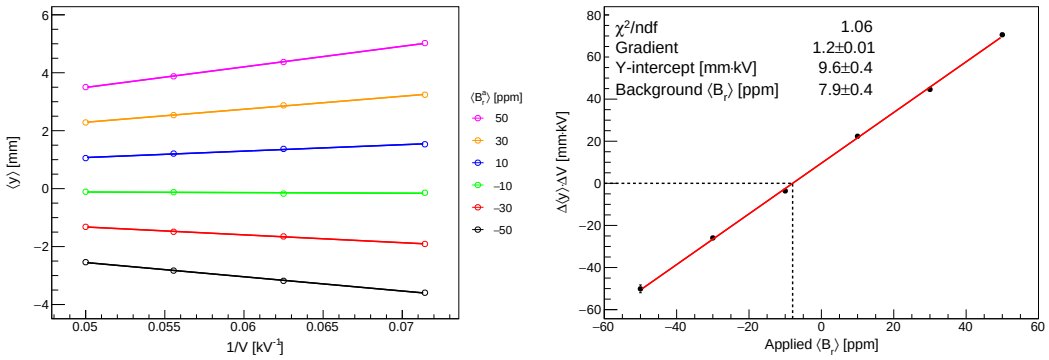

(a) Toy ESQ/SCC scans. **(b)** Toy $\langle B_r^b \rangle$ fit.

Figure 4.5: Fits for a toy radial field measurement with twenty four set-points and an injected $\langle B_r^b \rangle$ of 8 ppm. The measured result shows good agreement with the true value, and the uncertainty is less than the target of 1 ppm.

on the x-intercept – the uncertainty on $\langle B_r^b \rangle$ – is given by

$$\delta\langle B_r^b \rangle = \langle B_r^b \rangle \sqrt{\left(\frac{\delta m}{m}\right)^2 + \left(\frac{\delta c}{c}\right)^2 - \frac{2}{mc}\sigma_{mc}}, \tag{4.10}$$

where σ_{mc} is the covariance of the fit parameters m and c [78]. A full derivation of Equation 4.10 is given in Appendix C Section 1. Finally, once $\langle B_r^b \rangle$ has been measured, the SCC currents may be adjusted so that $\langle B_r^a \rangle = -\langle B_r^b \rangle$, setting $\langle B_r \rangle$ to zero.

4.2 Practical considerations

The aforementioned toy model, while useful for purposes of demonstration, was created primarily to provide a means of preparing the practical aspects of the measurement, such as: the values of the set-points, the number of set-points, and the total amount of beam time required to reach the target statistical precision of ≤ 1 ppm stated in Section 2.

In the toy model, the uncertainty on the average vertical cluster position per set-point, $\delta\langle y \rangle$, is assigned based on statistical uncertainties sampled from Run-1 data. For example, the toy measurement shown in Figure 4.5 possesses an inputted $\delta\langle y \rangle$ of 17.1 µm (equivalent to 2.87 million CTAGs[4] or 75 subruns[5]). The central value, $\langle y \rangle$, is randomly

[4] A CTAG, or calorimeter tag, is a measure of the number of calorimeter hits recorded over a certain time and energy range. It is used as a proxy for muon storage in E989 [79].

[5] A subrun is a subset of a run: a period of data collection defined by MIDAS DAQ system described in Chapter 3 Section 8.

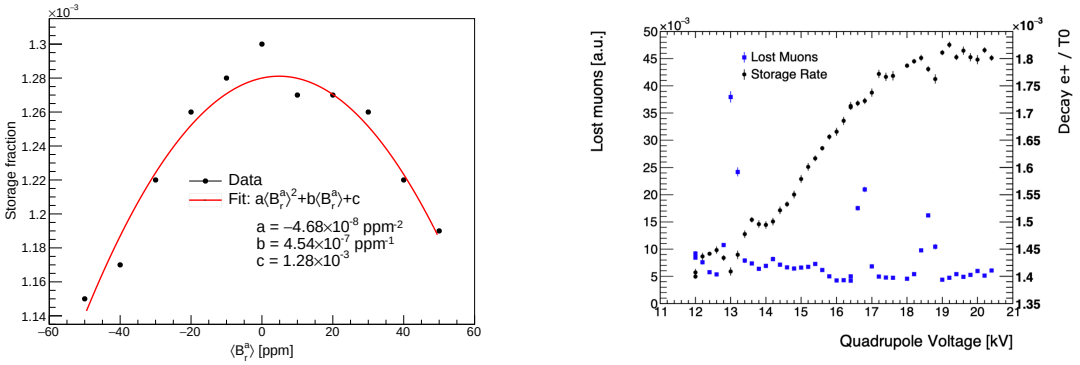

(a) Storage fraction vs. $\langle B_r^a \rangle$. **(b)** Storage fraction vs. V.

Figure 4.6: The change in muon storage fraction when adjusting (a) SCC $\langle B_r \rangle$ set-points, and (b) ESQ voltages . The minimum storage at 14 kV and -50 ppm is ∼300 CTAGs/fill. Images courtesy of P. Winter and A. Tewsley-Booth [80], and E. Barlas-Yucel [81].

drawn from a Gaussian distribution with a mean calculated by Equation 4.4, and a width equal to $\delta\langle y \rangle$. Many trial measurements may be performed to populate a distribution of fit uncertainties, $\delta\langle B_r^b \rangle$, the mean of which may be taken as the statistical precision associated with a particular configuration of set-points at some $\delta\langle y \rangle$.

The set-point configuration was chosen to give the widest range of values possible, without compromising on muon storage, based on the variation in storage over a range of $\langle B_r^a \rangle$ and V shown in Figure 4.6. Additionally, the maximum ESQ voltage was limited to 19.5 kV, according to the tolerances of the system. This chosen configuration utilised a total number of set-points, N_{set}, of twenty four, with: voltages of 14, 16, 18, and 19.5 kV; and applied radial fields of -50, -30, -10, 10, 30, and 50 ppm. Using this configuration, 1000 trials of the toy measurement were performed with varying levels of $\delta\langle y \rangle$, where the mean fit uncertainties are distributed against CTAGs per setting in Figure 4.7. The widths of the truth residual distributions for each value of $\delta\langle y \rangle$ are also overlaid as a cross-check, showing good agreement. All input values of $\delta\langle y \rangle$ produce a results with $\delta\langle B_r^b \rangle < 1$ ppm. From this, it may be inferred that the minimum total number of CTAGs, N_μ, required to reach ≤ 1 ppm is $\sim 9.5 \times 10^5$ (or 25 subruns). Referring again to Figure 4.6, the required beam-time of the measurement was calculated based on a conservative estimate of the average muon storage rate over the full measurement, R_μ, of ∼300 CTAGs per fill at 11 Hz. The total measurement time, t_{tot}, may then be

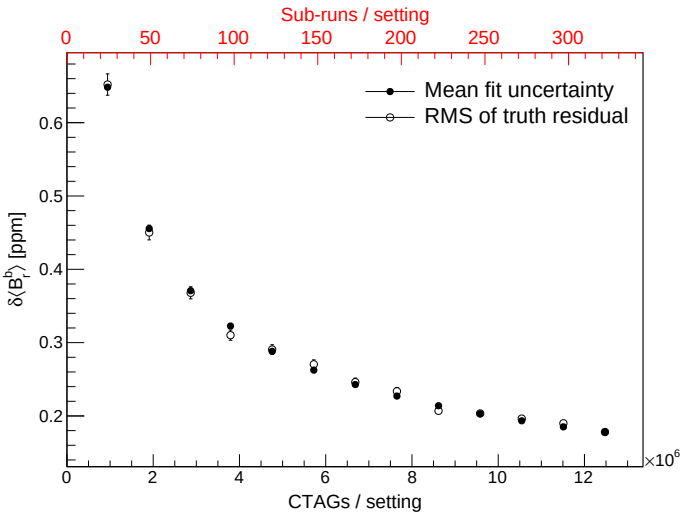

Figure 4.7: The mean fit uncertainties and the widths of the truth residual distributions for 1000 trial measurements, using the same configuration of set-points shown in Figure 4.5, graphed against CTAGs and subruns per setting. Data points at the same level of statistical uncertainty are consistent between the two distributions, and all values of $\delta\langle B_r^b\rangle$ are better than the target uncertainty of 1 ppm.

estimated, accounting for the time for adjustment between set-points, t_a, by

$$t_{\text{tot}} = N_{\text{set}} \cdot \left(\frac{N_\mu}{R_\mu} + t_a \right). \tag{4.11}$$

This means that the minimum t_{tot} required, with $t_a = 5$ minutes, would be ~ 4 hours. Fortunately, the time allocated for this measurement was ≤ 12 hours, making it possible to maximise the statistical precision by targeting $N_\mu = 3.79 \times 10^6$ CTAGS (100 sub-runs, or ~20 minutes beam-time) per set-point, or $t_{\text{tot}} \approx 10$ hours, corresponding to an estimated precision of $\delta\langle B_r^b\rangle = 0.403$ ppm. As an essential additional note in the methodology, ESQ beam scraping (which moves the beam in the x-y plane) was disabled for this measurement.

4.3 Extrapolating the results

In the context of the muon EDM search, $\langle B_r\rangle$ must be known for all E989 datasets used in the analysis. Estimates of $\langle B_r\rangle$ can be made for any dataset by examining the change in $\langle y\rangle$, $\Delta\langle y\rangle$, relative to a reference position, $\langle y\rangle_{\text{ref}}$, where $\langle B_r^b\rangle$ is known, given by

$$\Delta\langle y\rangle = \langle y\rangle - \langle y\rangle_{\text{ref}}. \tag{4.12}$$

This may be converted into $\Delta\langle B_r\rangle$ by a constant conversion factor, k:

$$\Delta\langle B_r\rangle = k\Delta\langle y\rangle. \tag{4.13}$$

If k, and by extension, $\Delta\langle B_r\rangle$, is known, then $\langle B_r\rangle$ may be estimated according to

$$\langle B_r\rangle = \Delta\langle B_r\rangle + \langle B_r^b\rangle_{\text{ref}}. \tag{4.14}$$

The constant k is found via an empirical method, where data from the radial field measurement is recycled to make linear fits to $\langle y\rangle$ against $\langle B_r^a\rangle$ for a range of voltages, the gradients of which are plotted against $1/V$, and the ensuing distribution is fitted with a straight line of the form

$$\frac{\Delta\langle y\rangle}{\Delta\langle B_r^a\rangle} = \frac{m}{V} + c, \tag{4.15}$$

where m and c are the gradient and y-intercept, and $\Delta\langle B_r^a\rangle = k\Delta\langle y\rangle$, from Equation 4.13. Provided that V is known in the dataset of interest, k may be calculated by

$$k = \frac{1}{\frac{m}{V} + c}. \tag{4.16}$$

This approach may be conceptualised as an inversion of the procedure used to measure $\langle B_r^b\rangle$, and is demonstrated in practice in Section 5.4. The uncertainty associated with k is given by the expression

$$\delta k = \sqrt{\left(\frac{1}{Vk^2}\right)^2 \cdot \delta m^2 + \left(\frac{1}{k^4}\right) \cdot \delta c^2 + \left(\frac{2}{Vk^4}\right) \cdot \sigma_{mc}}, \tag{4.17}$$

where σ_{mc} is the covariance of the fit parameters m and c [78]. A full derivation for Equation 4.16 is given in Appendix C Section 2.

The uncertainty on $\Delta\langle y\rangle$ receives contributions from statistical uncertainties on both the reference position and the measurement position, δ_{stat}, the systematic uncertainty arising the potential changes in calorimeter alignment between the reference dataset and the dataset of interest, δ_{align}, as well as the size of any drift in $\langle y\rangle$ over the dataset, δ_{drift}. The necessity of accounting for δ_{align} and δ_{drift} is obvious from the distribution of $\langle y\rangle$ per calorimeter, $\langle y_{\text{calo}}\rangle$, shown for Run-1 in Figure 4.8. The relative misalignment can be seen in the differences in vertical position between calorimeters. The drift in

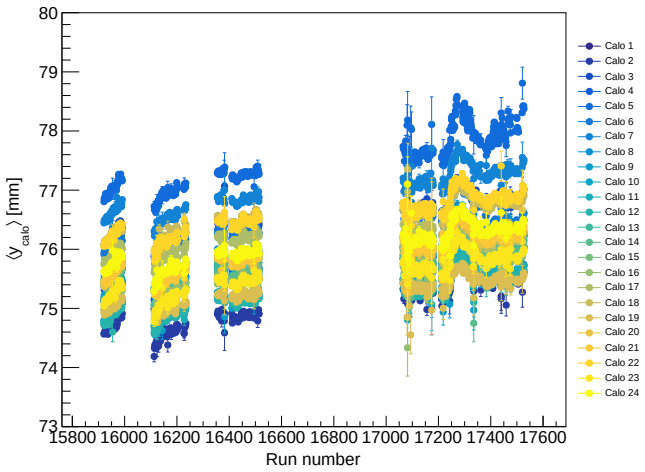

Figure 4.8: $\langle y \rangle$ per calorimeter in Run-1, where the four distinct datasets may be clearly seen. The differences in position between calorimeters is due to their relative misalignment, and the drift in position arises from a varying radial magnetic field caused by temperature fluctuations.

position, arising from a varying radial magnetic field, due to temperature fluctuations causing contraction and expansion of the magnet, is also clearly seen. δ_{align} is estimated by measuring the difference in vertical beam position reported by adjacent pairs of calorimeters in a particular dataset, taking the change in these differences compared to the reference position, and then taking the width of the resulting distribution as the uncertainty. δ_{drift} is taken to be the width of the distribution of $\langle y \rangle$ for a particular dataset. The total uncertainty on $\Delta\langle y \rangle$ is then the sum of these contributions in quadrature, so that

$$\delta\Delta\langle y \rangle = \sqrt{\delta^2_{\text{stat}} + \delta^2_{\text{align}} + \delta^2_{\text{drift}}}, \tag{4.18}$$

where the uncertainty on $\Delta\langle B_r \rangle$ is given by

$$\delta\Delta\langle B_r \rangle = \Delta\langle B_r \rangle \sqrt{\frac{\delta\Delta\langle y \rangle}{\Delta\langle y \rangle}^2 + \frac{\delta k}{k}^2}. \tag{4.19}$$

The absolute radial field uncertainty may then estimated by combining of Equation 4.19 and the uncertainty on $\langle B^b_r \rangle_{\text{ref}}$, as follows

$$\delta\langle B_r \rangle = \sqrt{\delta\Delta\langle B_r \rangle^2 + \delta\langle B^b_r \rangle^2_{\text{ref}}}. \tag{4.20}$$

5 Results

In this section, two measurements of $\langle B_r^b \rangle$, performed in Run-4, will be described. The first, a preliminary measurement, was used to prove the method and to enable the zeroing $\langle B_r^b \rangle$ prior to a second (primary) measurement. The primary measurement utilised the full configuration detailed in Section 4.2, aiming for sub-ppm precision. Based on the result of the primary measurement, and applying the method outlined in Section 5.4, estimates for $\langle B_r \rangle$ were made for various E989 datasets in Run-1 through Run-3. An estimate was also performed in Run-4 for completeness, along with a preliminary estimate made using a small subset of nearline (NL) data in Run-5.

5.1 Preliminary results for the background radial field

A preliminary background radial field measurement was performed over the 8^{th}–9^{th} of December 2020, during a period of Run-4 where beam intensity was ∼10% of Run-3. Because of the low beam intensity, the minimum possible number of settings was used, with voltages of 14 kV and 18 kV, and applied radial magnetic fields of −30 ppm and 30 ppm. Data was collected for 1.5 hours (aiming for ∼2.5 million CTAGs) per set-point, targeting a precision of ∼ 1 ppm [82]. The results of the preliminary measurement are illustrated in Figure 4.9,

$$\langle B_r^b \rangle = 15 \pm 1 \text{ ppm},$$

which was then used to zero $\langle B_r^b \rangle$ prior to the primary measurement.

5.2 Primary results for the background radial field

Following the preliminary measurement, and subsequent zeroing of the background radial field, the beam intensity was increased to nominal and a second measurement was carried out on the 30^{th} of December 2020, using the full configuration described in Section 4.2. As planned, data was collected for ∼ 20 minutes (aiming for ∼4 million CTAGs) per set-point, targeting a precision of ∼ 0.4 ppm. Two settings, 18 kV at 10 ppm and 14 kV at −50 ppm, are not included in the analysis due to errors when loading those configurations in the field DAQ [83]. The results of the primary measurement are

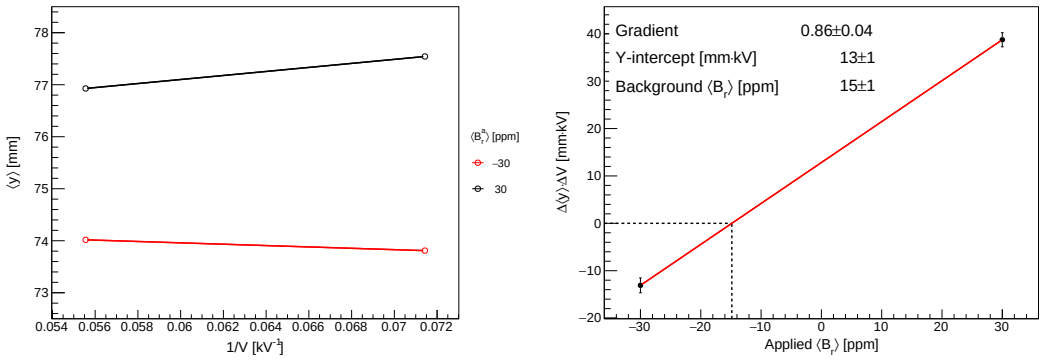

(a) Preliminary ESQ/SCC scans. **(b)** Preliminary $\langle B_r^b \rangle$ fit.

Figure 4.9: The results of the preliminary measurement of $\langle B_r^b \rangle$ in Run-4, showing: (a) ESQ scans of $\langle y \rangle$ over $1/V$ for two SCC $\langle B_r^a \rangle$ set-points; (b) $\Delta\langle y \rangle \cdot \Delta V$ over $\langle B_r^a \rangle$. $\langle B_r^b \rangle$ was measured to be 15 ± 1 ppm.

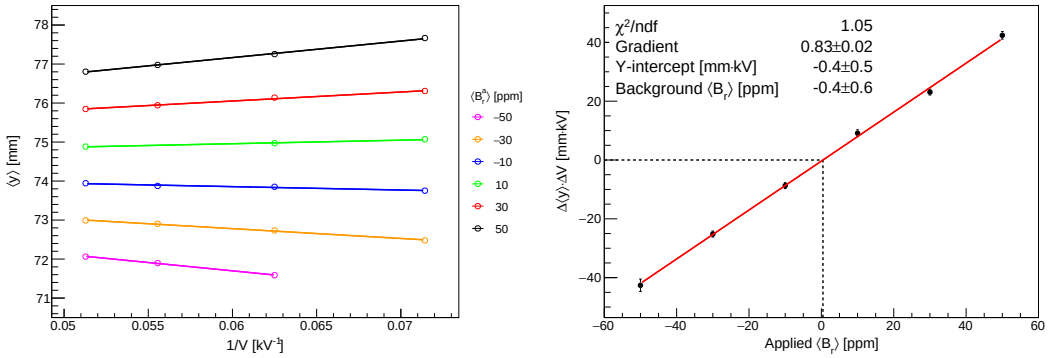

(a) Primary ESQ/SCC scans. **(b)** Primary $\langle B_r^b \rangle$ fit.

Figure 4.10: The results of the primary measurement of $\langle B_r^b \rangle$ in Run-4, showing: (a) ESQ scans of $\langle y \rangle$ over $1/V$ for the full range of SCC $\langle B_r^a \rangle$ set-points; (b) $\Delta\langle y \rangle \cdot \Delta V$ over $\langle B_r^a \rangle$. $\langle B_r^b \rangle$ was measured to be -0.4 ± 0.6 ppm.

illustrated in Figure 4.10, where the $\langle B_r^b \rangle$ was measured to be

$$\langle B_r^b \rangle = -0.4 \pm 0.6 \text{ ppm},$$

which is consistent with zero as expected, and has a statistical uncertainty of < 1 ppm, as required.

5.3 Analysis cuts

The quantity being directly observed throughout these measurements was the ring average vertical cluster position, $\langle y \rangle$, which depends on the energy and in-fill hit times of

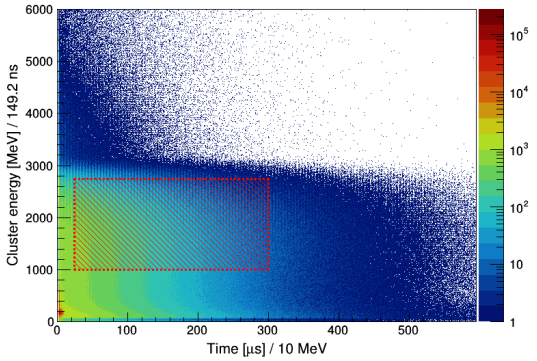

(a) Cluster energy against time in-fill.

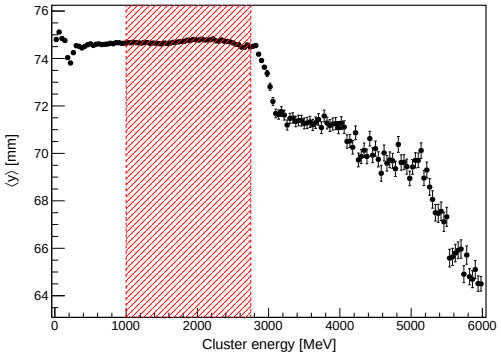

(b) $\langle y \rangle$ against cluster energy.

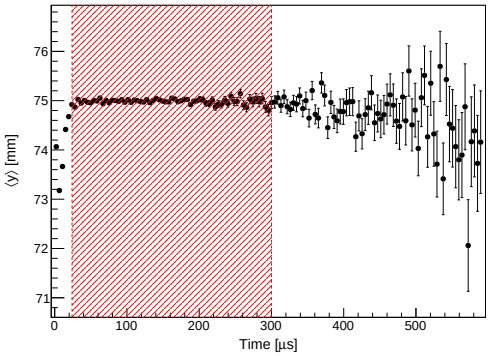

(c) $\langle y \rangle$ against time in-fill.

Figure 4.11: Cuts in time and energy used during the analysis of $\langle B_r^b \rangle$, optimised for stability in $\langle y \rangle$.

the decay positrons. Cuts were implemented to select a region of parameter space where $\langle y \rangle$ is stable, illustrated in Figure 4.11, with the red lines outlining the following regions used in the analysis:

$$23 < t\ [\mu\text{s}] < 300 \quad \text{and} \quad 1000 < E\ [\text{MeV}] < 2750.$$

The possible factors driving these regions of instability are: ESQ charging at early times, a low muon population at late times, positron pileup at high energies, and lost muons at low energies.

5.4 Extrapolation results

Following the measurements of $\langle B_r^b \rangle$, $\langle B_r \rangle$ was estimated for various datasets from Run-1 through to Run-5. The period of the runs selected to act as a reference position, $\langle y \rangle_{\text{ref}}$, follows the primary radial field measurement in Run-4, and consists of runs 38100-42588.

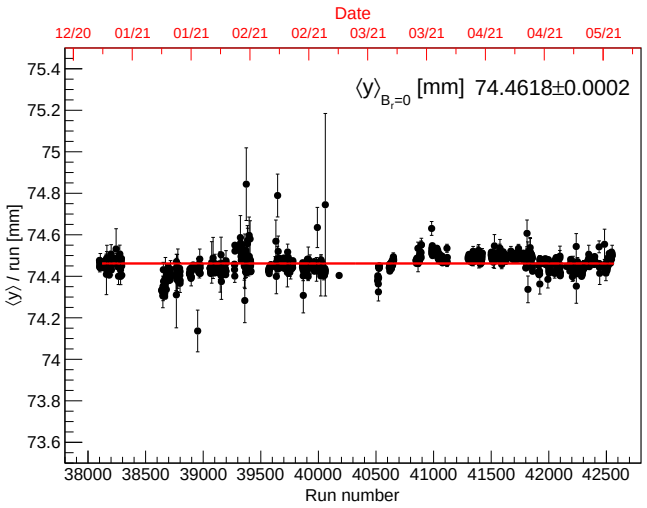

Figure 4.12: A zeroth order fit to $\langle y \rangle$ over a period of Run-4 where $\langle B_r \rangle$ was known to be zero. The result is an uncertainty weighted average which may be used as a reference position, $\langle y \rangle_{\text{ref}}$, to estimate $\langle B_r \rangle$ in any E989 dataset.

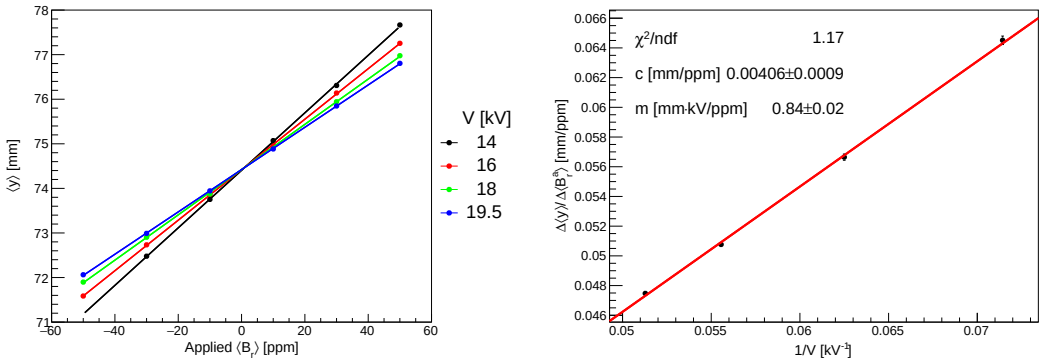

(a) **(b)**

Figure 4.13: Fits for the radial field conversion factor, k, showing: (a) fits to scans of $\langle y \rangle$ over $\langle B_r^a \rangle$; (b) a fit the gradients $\Delta\langle y \rangle / \Delta\langle B_r^a \rangle$ against $1/V$, giving a function which may be evaluated at the voltage used in the dataset of interest to obtain k.

This corresponds to a period between the 5$^{\text{th}}$ of January 2021 and the 10$^{\text{th}}$ of May 2021. The uncertainty weighted $\langle y \rangle$ was measured via a zeroth order polynomial fit over this period, as shown in Figure 4.12, giving

$$\langle y \rangle_{\text{ref}} = 74.4618 \pm 0.0002 \text{ mm}.$$

This done, the constant required to convert between $\Delta\langle y \rangle$ and $\Delta\langle B_r \rangle$, k, from Equation 4.16, was derived from the same data used in the primary measurement of $\langle B_r^b \rangle$. Fits

for k are shown in Figure 4.13, giving

$$k\,(18.3\text{ kV}) = 19.9 \pm 0.6\text{ ppm/mm}$$
$$k\,(20.4\text{ kV}) = 21.9 \pm 0.7\text{ ppm/mm},$$

where the ESQ voltage is 18.3 kV for all datasets except Run-1b and Run-1c, where it is 20.4 kV (as given in Table 3.2) [30].

The systematic contributions from calorimeter misalignment and field drift, δ_{align} and δ_{drift}, were then estimated (following the method detailed in Section 5.4). An example of the relative misalignment per calorimeter in Run-1a compared to Run-4 is shown in Figure 4.14a, where the width of the distribution in Figure 4.14b was taken as δ_{align} for

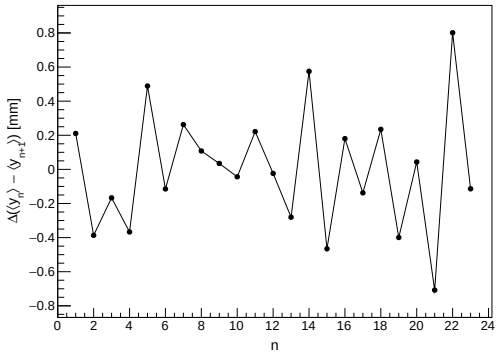

(a) Adjacent calorimeter $\Delta\langle y\rangle$.

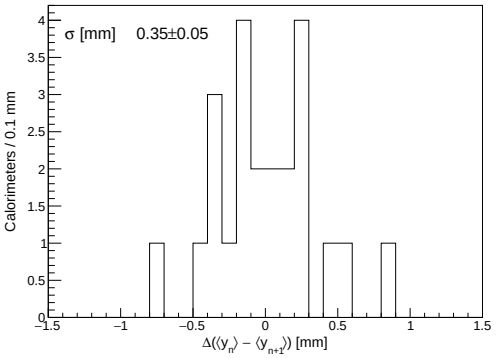

(b) The change in adjacent calorimeter $\Delta\langle y\rangle$.

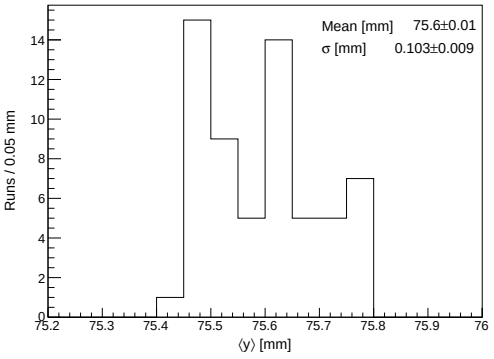

(c) The drift in $\langle y\rangle$.

Figure 4.14: Assessment of the systematic uncertainties δ_{align} and δ_{drift} in Run-1a, showing: (a) the difference in measured $\langle y\rangle$ between adjacent pairs of the twenty four calorimeters, where $n = 1$ represents the pair $\langle y_1\rangle - \langle y_2\rangle$; (b) the distribution of those differences compared to Run-4, the width of which was taken as δ_{align}; (c) the distribution of $\langle y\rangle$, where again, the width was taken as the uncertainty δ_{drift}.

Dataset	δ_{stat} [mm]	δ_{align} [mm]	δ_{drift} [mm]
1a	7.28×10^{-4}	0.348	0.103
1b	6.28×10^{-4}	0.354	0.109
1c	5.29×10^{-4}	0.369	0.0480
1d	4.12×10^{-4}	0.425	0.162
2b	8.25×10^{-4}	0.175	0.0381
2c	4.05×10^{-4}	0.183	0.0631
2d	4.46×10^{-4}	0.298	0.0914
2e	6.75×10^{-4}	0.173	0.0385
2f	6.44×10^{-4}	0.173	0.0450
2g	1.80×10^{-3}	0.236	0.0600
2h	1.14×10^{-3}	0.246	0.0208
3N	4.36×10^{-4}	0.247	0.0316
3O	4.82×10^{-4}	0.269	0.0233
4 (NL)	3.37×10^{-4}	0.0235	0.0510
5 (NL)	3.88×10^{-4}	0.171	0.0224

Table 4.1: Contributions to the uncertainty on the estimated total radial magnetic field in each datasets. Estimates in Run-4 and Run-5 were made using nearline (NL) data, and so are preliminary.

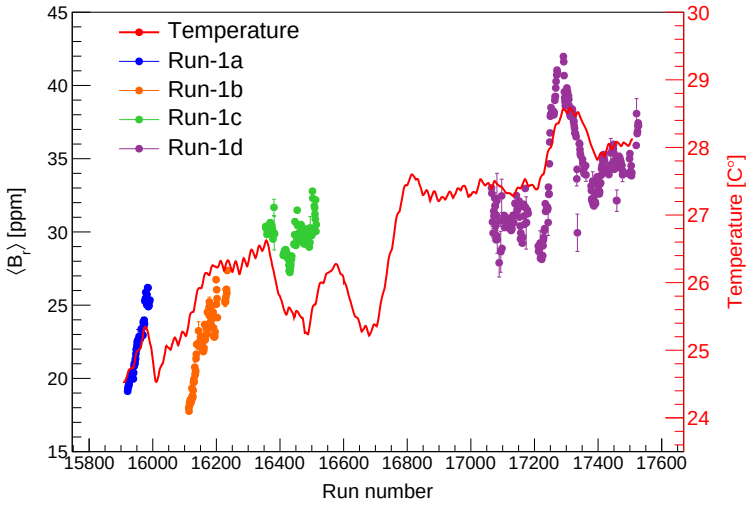

Figure 4.15: The estimated $\langle B_r \rangle$ throughout Run-1. The observed variation appears to be correlated with the temperature as measured by a probe inside the experiment hall, which is overlaid on a secondary scale for comparison. The uncertainties associated with each data-point are purely statistical. Temperature data courtesy of D. Vasilkova [84].

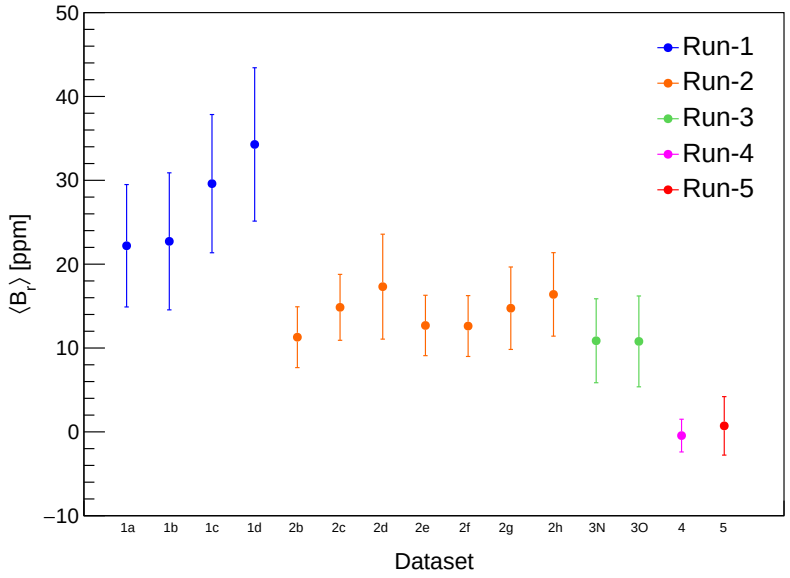

Figure 4.16: Estimates for $\langle B_r \rangle$ in ppm for various E989 datasets. The estimates for Run-4 and Run-5 are preliminary.

Dataset	$\langle B_r \rangle$ [ppm]	Equivalent d_μ [$\times 10^{-20}$ e·cm]
1a	22 ± 7	7 ± 2
1b	23 ± 8	7 ± 3
1c	30 ± 8	9 ± 3
1d	34 ± 9	10 ± 3
2b	11 ± 4	4 ± 1
2c	15 ± 4	5 ± 1
2d	17 ± 6	6 ± 2
2e	13 ± 4	4 ± 1
2f	13 ± 4	4 ± 1
2g	15 ± 5	5 ± 2
2h	16 ± 5	5 ± 2
3N	11 ± 5	3 ± 2
3O	11 ± 5	3 ± 2
4 (NL)	-0.4 ± 2.0	-0.1 ± 0.6
5 (NL)	0.7 ± 3.5	0.2 ± 1.1

Table 4.2: Estimates for $\langle B_r \rangle$ in ppm, as well as the equivalent fake EDM signal in e·cm, for various E989 datasets. The uncertainties for Run-1 are within the 10 ppm target stated in Section 2.

that dataset. An example distribution of $\langle y \rangle$ for Run-1a, the width of which was taken as δ_{drift} for that dataset, is shown in Figure 4.14c. These systematic uncertainties are reported, alongside the statistical contribution, δ_{stat}, for various E989 dataset in Table 4.1. The contribution from calorimeter misalignment dominates.

For the purposes of illustration, the estimated $\langle B_r \rangle$ per run is presented for Run-1 in Figure 4.15, where the uncertainty per run is taken as purely statistical. Significant variation may be seen both within and between datasets, which appears to be correlated with the temperature as measured by a probe inside the experiment hall. The cause of this correlation is thought to arise from the expansion and contraction of the C-shaped yoke with varying hall temperature. Since Run-1, the addition of thermal insulation around the magnet, as well as improvements to the climate control inside the experiment hall, appear to have minimised this effect.

Finally, the results for $\langle B_r \rangle$ are presented in Figure 4.16 and Table 4.2, which includes to the total uncertainty $\delta\langle B_r \rangle$. The equivalent laboratory frame precession plane tilt angle is also given in units of e·cm, which is obtained by first taking $\langle B_r \rangle$ in units of ppm to be equivalent to µrad by the small angle approximation, so that the laboratory frame tilt angle is given by

$$\delta = \frac{B_r}{B_y}, \tag{4.21}$$

and calculating the equivalent fake muon EDM signal by Equation 2.29. These values will eventually be subtracted from the measured muon EDM signal.

6 Summary and outlook

The average background radial field, $\langle B_r^b \rangle$, was measured in E989 Run-4 by use of a novel ESQ/SCC scan-based method. Two measurements were performed. The first was a preliminary measurement performed on the 8^{th}–9^{th} of December 2020, during a period with low beam intensity (10% of Run-3), where $\langle B_r^b \rangle$ was measured to be 15 ± 1 ppm. Following this result, SCC currents adjusted were to cancel the background, so that the total field, $\langle B_r \rangle$, was set to zero. A second measurement was then performed on the 30^{th} December 2020 with nominal beam intensity, whereupon $\langle B_r^b \rangle$ was found to -0.4 ± 0.6 ppm, which is consistent with zero. The target uncertainty for this measurement, based on the statistically limited case for a muon EDM search using the E989 integrated dataset, was $\leq$1 ppm, which is achieved by this measurement. This result was then

extrapolated, based on the change in ring average vertical beam position, to estimate $\langle B_r \rangle$ for all available E989 datasets. These estimates are reported in Figure 4.16 and Table 4.2. In the case of the Run-1 datasets, the uncertainties fall within the target of $\leq$10 ppm (for 100 million high quality tracks), meaning that the search for a muon EDM in Run-1 is not limited by the radial field systematic.

The ESQ/SCC scan-based method has the significant advantage over measurements which involve the use of additional hardware, such as hall probes, in that it does not require any physical modifications to the experiment, and may be accomplished in a relatively short period of beam-time. Since the time of writing, the methods described in this chapter have been used by fellow E989 collaborators to conduct a measurement of $\langle B_r^b \rangle$ in Run-5, and produce estimates of the radial field in further E989 datasets as they are produced.

Chapter 5

Simulation for the muon EDM search

The muon EDM search described in this thesis relies on a large-scale Monte Carlo simulation to verify aspects of the theory behind the EDM search, develop the analysis strategy, and study sources of systematic uncertainty. Critically, simulation also provides a means of characterising the impact of detector acceptance on the dilution of observed angle in-phase with the EDM oscillation, A_{EDM}, compared with the laboratory frame tilt angle, δ. Without this, an accurate measurement of a potential muon EDM signal is not possible. This work builds on previous muon EDM simulation efforts at E989 by S. Charity [57] and G. Lukicov [85].

1 Simulation with a large injected muon EDM

The analysis described in this section depends, to a great extent, on access to a large sample of Monte Carlo events with an injected muon EDM of known size. The size of the injected signal was chosen to be $5.4 \times 10^{-18}\ e \cdot \mathrm{cm}$, or $30\times$ the muon EDM upper limit measured at BNL [4]. The exact magnitude of the injected signal is somewhat arbitrary, but a large signal is preferable as it may be more easily resolved from a finite number of simulated events. An additional, smaller, sample with an injected muon EDM of $1.8 \times 10^{-18}\ e \cdot \mathrm{cm}$, or $10\times$ the BNL upper limit, was generated for the purposes of cross-checking the main sample. By application of Equation 2.29, this gives δ values of 1.69 mrad and 0.594 mrad for the $30\times$ and $10\times$ BNL samples respectively.

Events were generated using the GEANT4-based in-house framework `gm2ringsim`, introduced in Chapter 3 Section 8, using a mode termed the 'gas gun'. In this mode, muon decay times are randomly sampled from an exponentially decaying distribution,

Label	Description	Decays or vertices [$\times 10^6$]
All decays	All e^+ (100% acceptance)	70.6
Truth/reco vertices	Truth/measured information from track vertices	32.9

Table 5.1: The three simulation reconstructions described in this chapter, including the number of decays, or quality-cut-passing track vertices, for samples with an injected EDM of 5.4×10^{-18} $e\cdot$cm ($\sim 30\times$ the BNL upper limit). Approximately 1% of generated events (one muon per event) results in high quality track vertex. The *truth/reco vertices* samples are not a subset of *all decays* in this case.

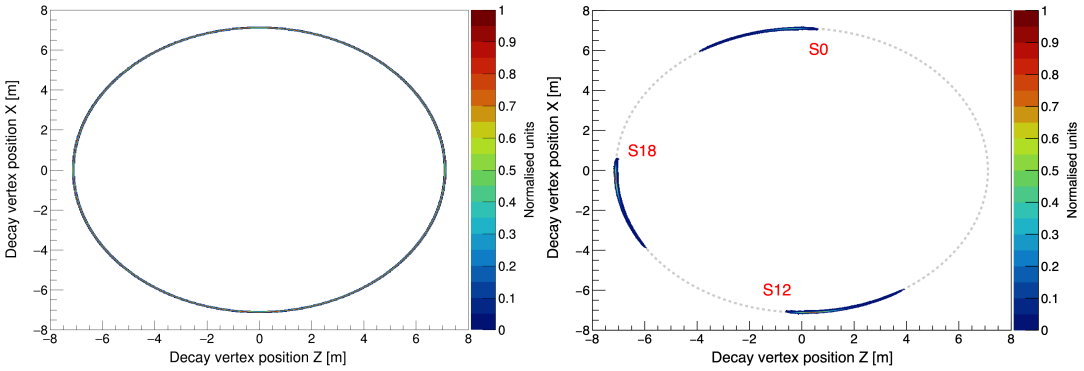

(a) *All decays.* **(b)** *Reco vertices.*

Figure 5.1: The azimuthal acceptance of Monte Carlo events for: (a) truth parameters for all positrons, *all decays*, with 100% acceptance; (b) measured information from track decay vertices, *reco vertices*, showing a $\sim 25°$ acceptance. The coordinate system is the same as used in Figure 3.20, that is, where the inflector is positioned at 12 o'clock with the muons circulating clockwise. The ideal orbit is marked by a grey dashed line, and the positions of each tracker station are indicated. Station 0 (S0) is a proposed third tracker station, which, at present, only exists in simulation.

while the energy-momentum four-vector, position, and polarisation of the individual muons are determined based on the time since injection. The simulated muons are then placed in a model of the storage ring and allowed to decay instantaneously. A muon EDM is injected by the addition of an oscillating vertical component to the muon polarisation vector [57].

Once generated, events were reconstructed in three distinct ways: the first, labelled *all decays*, utilised truth decay parameters for all positrons in the sample, with no detector effects; the second, labelled *truth vertices*, used truth information associated with extrapolated track decay vertices; and the third, labelled *reco vertices*[1], used measured

[1] 'Reco' being an abbreviation for 'reconstructed', or 'measured using the nominal track reconstruction algorithm'.

information associated with extrapolated track decay vertices. These three reconstructions are summarised in Table 5.1, along with the number of e^+ or quality-cut-passing extrapolated track vertices, introduced in Chapter 3 Section 6.3, for the primary 30× BNL sample. Comparison between decays and vertices was critical when characterising the impact of the detector acceptance on the dilution of the measured tilt angle, expanded upon in Section 4. This is because the *all decays* sample provides a means of performing a muon EDM analysis with 100% acceptance, as demonstrated by the azimuthal acceptance for *all decays* compared with *reco vertices* shown in Figure 5.1.

It should be noted that the samples of decays and track vertices were not reconstructed from entirely the same sets of events, so that one is not a subset of the other. This is because a large sample consisting only of track vertices was generated prior to the decision to retain the decays, and means that the relative number of vertices and decays in Table 5.1 are not a reflection of detector acceptance. The true acceptance of the trackers, in terms of track vertices per decay positron, has been measured to be ∼3.5% (where just ∼1% form high quality track vertices). This is despite the excellent 25° azimuthal acceptance per tracker station, which is limited by the fact that the number of positrons is highest at low momentum (below 1 GeV), as illustrated by the number distribution function in Figure 2.9, and the average momentum of tracks originating from further upstream are necessarily high momentum – lower momentum positrons curl out of the storage region before reaching the detector. The low momentum positrons which do pass through the trackers do not generally form good quality tracks due to their high curvature in the magnetic field. Track quality cuts are discussed in Chapter 3 Section 6.3.

2 Verifying the decay asymmetry function

A fundamental aspect of the underlying physics driving the experimental sensitivity to an EDM at E989 is the decay asymmetry function, $A(\lambda)$, given by Equation 2.35 in Chapter 2 Section 3.4. As such, it is important to verify the validity of this function. This was accomplished by use of the *all decays* sample, where truth information was used to calculate the angle ϵ between the x-z plane and the muon spin polarisation vector, as well as the angle θ between the x-z plane and the decay positron momentum vector. If the product of these angles is positive, so that $\epsilon \cdot \theta > 0$, then the muon spin

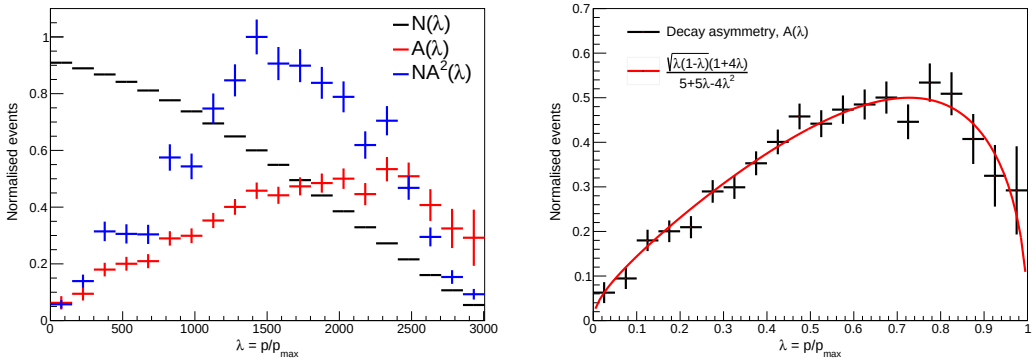

(a) **(b)**

Figure 5.2: EDM decay asymmetry verification, showing: (a) The simulated distributions of the number function, $N(\lambda)$, the decay asymmetry function, $A(\lambda)$, and the statistical FOM function, $NA^2(\lambda)$, in the laboratory frame; (b) the analytical form of $A(\lambda)$ overlaid on the corresponding simulated distribution, showing excellent agreement.

vector and positron momentum vector must be directed in the same vertical hemisphere, and so these were counted as 'up' decays. If $\epsilon \cdot \theta < 0$, then the reverse is true, and such decays were counted as 'down' decays. From the numbers of up/down decays, N_u and N_d, it is possible to define the asymmetry as

$$A = \frac{N_u - N_d}{N_u + N_d}, \tag{5.1}$$

with a corresponding uncertainty of

$$\delta A = \sqrt{\frac{1 - A^2}{N_u + N_d}}, \tag{5.2}$$

a full derivation for which is given in Appendix C Section 3. The distributions $A(\lambda)$ and the statistical figure-of-merit (FOM) $NA^2(\lambda)$, derived from simulation, are shown in Figure 5.2a. The analytical form of $A(\lambda)$ is overlaid on the corresponding distribution from simulation in Figure 5.2b, showing excellent agreement.

3 Fitting the vertical angle oscillation

As introduced in Chapter 2 Section 3.3, the measured signal in this analysis is the vertical angle in-phase with the EDM oscillation, A_{EDM}. This quantity may be accessed by fitting for an oscillation in the average vertical angle as a function of time, $\langle \theta_y \rangle(t)$, which is phase shifted by $\pi/2$ from the anomalous precession oscillation (the number

oscillation, introduced in Chapter 2 Section 2.5). Therefore, the first step in the analysis is to fit the number oscillation for the anomalous precession oscillation phase, ϕ, using the five parameter function given by Equation 2.14. $\langle\theta_y\rangle(t)$ may then be fitted with Equation 2.33 for A_{EDM}, with ϕ as a fixed parameter. ω_a is fixed to a value of 1.439311 rad/µs throughout, which is the average measured value for the positive muon at the BNL $g-2$ experiment [2].

Furthermore, the muon EDM search presented in this thesis employs momentum-binned approach, which is motivated, in part, by the momentum dependence of A_{EDM} – or, the momentum dependence of the total dilution of δ – described by Equation 2.38. Additionally, and as will be discussed in both Section 3.5 and Chapter 6 Section 3.3, the average vertical angle itself possesses a momentum dependence (due to acceptance effects), further motivating a momentum-binned analysis. Fits to the vertical angle oscillation without the use of this technique, where momentum intervals are fitted simultaneously, are referred to in this thesis as 'simultaneous fits'. These are performed as a cross-check of the main results.

3.1 Modulation at the anomalous precession period

In the analysis of both simulation and Run-1 data, which is presented in Chapter 6, the number oscillation and the vertical angle oscillation are modulated at the anomalous precession period, $T_{g-2} = 4.365\,\mu\mathrm{s}$. This simply means that the distribution of θ_y as a function of time is divided into periods of T_{g-2}, which are then recombined into a single

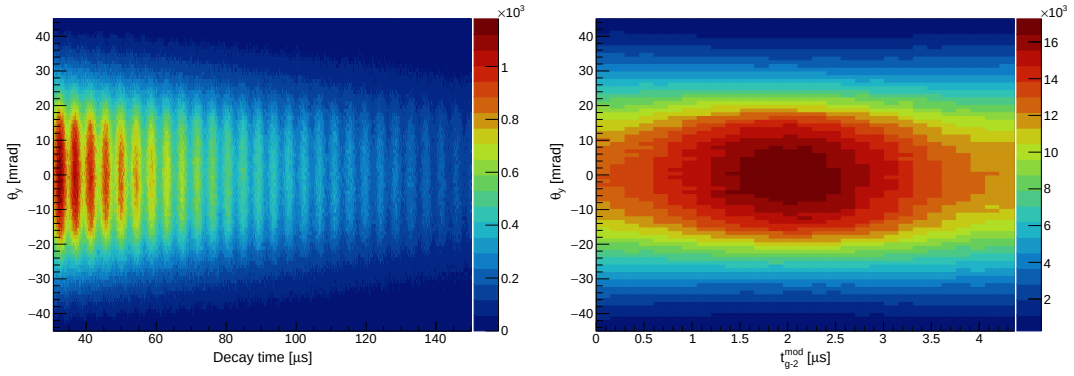

(a) Unmodulated. **(b)** Modulated.

Figure 5.3: The effects of time modulation at the anomalous precession period, showing the distribution of vertical decay angles over time with (a) no modulation, and (b) with modulation. The distributions pictured are formed from the *all decays* reconstruction.

distribution, as demonstrated in Figure 5.3. Time modulation is employed so as to minimise the influence of oscillations such as the CBO, introduced in Chapter 3 Section 4.1, which will de-phase and destructively interfere over many modulated periods. This technique also maximises sensitivity to oscillations with a period equal to T_{g-2}, which combine constructively. The modulated time, t_{g-2}^{mod}, is calculated by

$$t_{g-2}^{\text{mod}} = \left(\frac{t}{T_{g-2}} - \text{int} \left[\frac{t}{T_{g-2}} \right] \right) \cdot T_{g-2}, \tag{5.3}$$

which is reproduced from [85].

3.2 Momentum selection

The maximum statistical sensitivity to a muon EDM occurs at middling decay positron energy, as demonstrated by the statistical FOM function, $NA^2(\lambda)$, in Figure 2.9. Consequently, cuts are imposed to select tracks of middling momentum. The choice of momentum range also depends on the momentum acceptance of the trackers, which drops off sharply below 1000 MeV. Accounting for this, the momentum range was chosen to be 1000-2500 MeV: a region overlaid on the momentum distribution as measured by the straw trackers in Run-1a in Figure 5.4. In the case of the anomalous precession oscillation, a low energy threshold of 1.7 GeV was used, based on the optimum thresh-

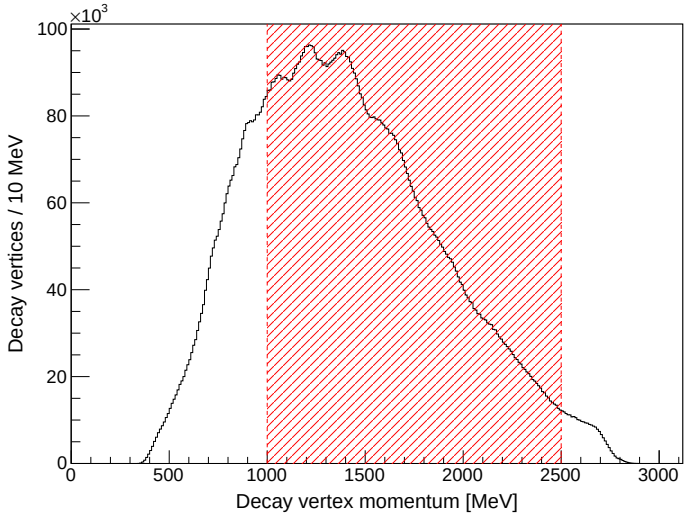

Figure 5.4: The positron momentum distribution as measured by the straw trackers in Run-1a, illustrating the momentum range selected for the analysis of the vertical angle oscillation. Tracker stations 12 and 18 are combined.

old for maximising the statistical sensitivity to the anomalous precession oscillation, discussed in Chapter 2 Section 2.5.

3.3 Anomalous precession oscillation fits

Fits to the number oscillation for the anomalous precession oscillation phase, ϕ, for each of the three reconstructions of the 30× BNL Monte Carlo sample, are shown in Figures 5.5a, 5.5c, and 5.5e. The measured phases are included in Table 5.2.

An early time cut of 30.6 µs, or seven multiples of T_{g-2}[2], is imposed. This time cut is essential to avoid ESQ scraping, as well as the worst effects of the fast rotation and muon losses (described in Chapter 3). In order to remove any residual fast rotation effects, the oscillation is binned in time at the cyclotron period, T_c =149.2 ns, and decay times are uniformly randomised by $\pm T_c/2$ about the measured value. Tracker stations 12 and 18 are combined, and station 0 is excluded.

3.4 Simultaneous vertical angle oscillation fits

Fits to the average vertical angle oscillation over the momentum range of 1000-2500 MeV, for A_{EDM}, are shown in Figures 5.5b, 5.5d, and 5.5f, for each of the three reconstructions of the 30× BNL Monte Carlo sample. For the same reasons as given in the context of the anomalous precession oscillation fits, an early time cut of 30.6 µs is imposed, and decays times are both measured in intervals of T_c and uniformly randomised by $\pm T_c/2$ about the measured value.

The reduced χ^2 of the vertical angle fits, the observed A_{EDM}, and the average dilution factor in this momentum range are given in Table 5.2. Importantly, these results highlight the impact of detector acceptance, in that the average reduction of A_{EDM} com-

Label	χ^2/NDF	ϕ [rad]	A_{EDM} [mrad]	d_{EDM}
All decays	0.974	0.169 ± 0.003	0.250 ± 0.006	0.148 ± 0.004
Truth vertices	1.47	0.134 ± 0.004	0.126 ± 0.006	0.075 ± 0.004
Reco vertices	1.36	0.141 ± 0.004	0.127 ± 0.006	0.075 ± 0.004

Table 5.2: A summary of fit results, corresponding to Figure 5.5, listing: the χ^2/NDF, the observed A_{EDM}, and the dilution, d_{EDM}, for each reconstruction. The results of the vertical angle oscillation fits are consistent between *truth vertices* and *reco vertices*, and the *all decays* sample demonstrates the greatest sensitivity to the injected EDM.

[2]When utilising time modulation, time cuts must be placed at a multiple of the modulation period.

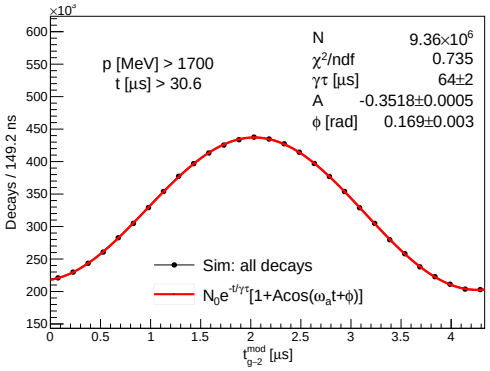

(a) *All decays*: fit for ϕ.

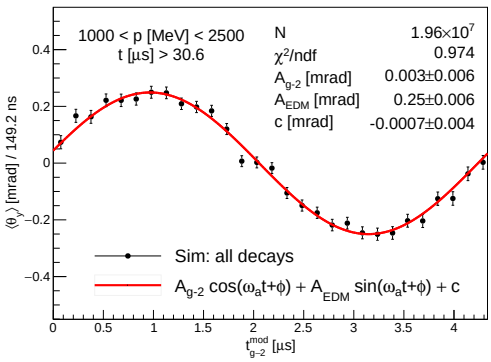

(b) *All decays*: fit for A_{EDM}.

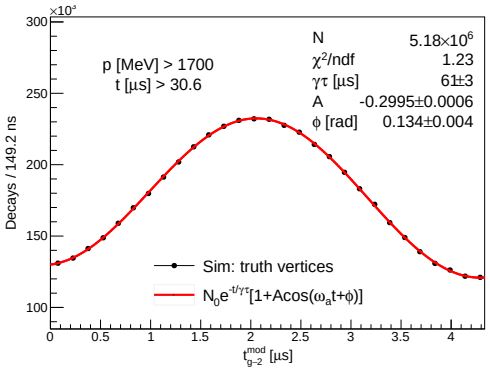

(c) *Truth vertices*: fit for ϕ.

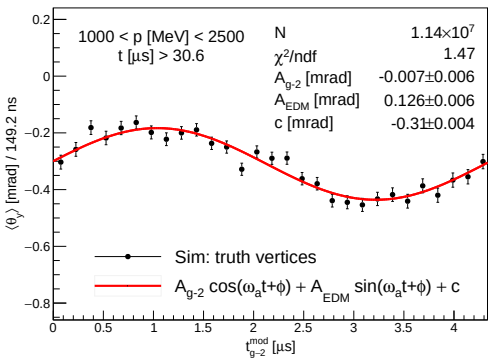

(d) *Truth vertices*: fit for A_{EDM}.

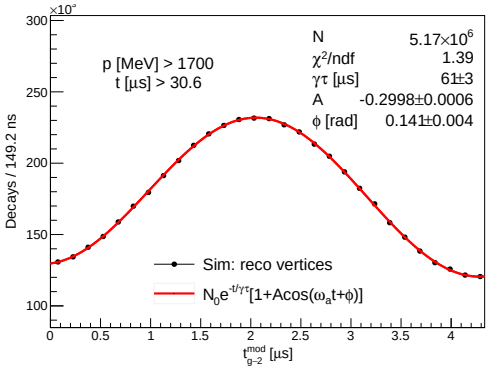

(e) *Reco vertices*: fit for ϕ.

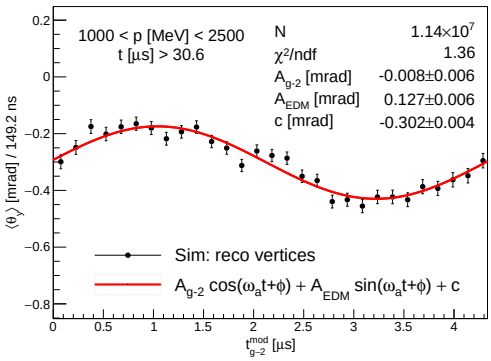

(f) *Reco vertices*: fit for A_{EDM}.

Figure 5.5: Fits to both the number oscillation, for the anomalous precession phase ϕ, and the average vertical angle oscillation, for the observed EDM vertical angle, A_{EDM}. Tracker stations 12 and 18 are combined, and station 0 is excluded. As discussed in the text, the inclusion of detector acceptance results in a more pronounced dilution of the tilt angle, $\delta = 1.69$ mrad. A_{EDM} is consistent between *truth vertices* and *reco vertices*.

pared to δ is more pronounced for *truth/reco vertices* by an approximate factor of two. The fit quality also degrades with the inclusion of acceptance, as seen in the change in χ^2/NDF.

3.5 The dependence of the average vertical angle on momentum in simulation

For extrapolated track decay vertices, the average vertical angle, $\langle\theta_y\rangle$, is offset from zero; as demonstrated by the parameter c in vertical angle oscillation fits shown in Figure 5.5. This offset has a dependence on momentum, which is not observed in the *all decays* reconstruction above 500 MeV, shown by Figure 5.6a. From this, it may be inferred that this momentum dependence is a consequence of detector effects rather than a physical change in the true average vertical angle. Moreover, the fact that the offset is less pronounced in tracker station 0, as shown in Figure 5.6b, which has perfect global alignment (expanded upon Section 6) with the beam in simulation, indicates that this effect is partly related to global tracker alignment, and by extension detector acceptance. This dependence is also present in data, as will be discussed in Chapter 6 Section 3.3.

The dependence of $\langle\theta_y\rangle$ on momentum is one factor motivating the aforementioned momentum-binned approach to fitting the vertical angle oscillation. In this context, dividing the oscillation into momentum intervals has the effect of reducing the variation

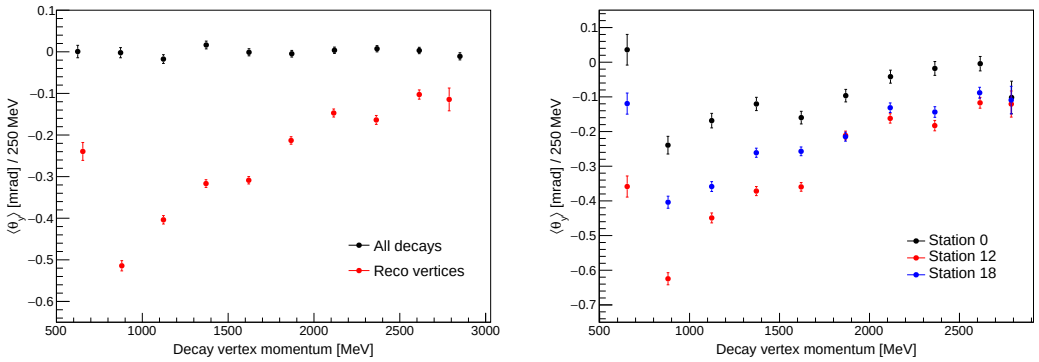

(a) **(b)**

Figure 5.6: The average vertical angle in momentum intervals of 250 MeV, for (a) *all decays* and *reco vertices* (station 12 and station 18 combined), and (b) individual stations including station 0 (for *reco vertices*). Above 500 MeV, this momentum dependence is not present in *all decays*, and is therefore a detector effect. This is partly acceptance related, since it is less pronounced in station 0, which has perfect global alignment in simulation.

in $\langle\theta_y\rangle$ with momentum in each fit.

3.6 Momentum-binned fits

Fits to the average vertical angle oscillation in momentum intervals of 250 MeV, using the *reco vertices* reconstruction of the 30× BNL sample, are presented in Figure 5.8. Besides the momentum binning, the fitting procedure is identical to that described in Section 3.4, and the same values of ϕ are used as are reported in Table 5.2.

The measured values of A_{EDM} for each of the three reconstructions are distributed over the range of 500-3000 MeV in Figure 5.7a. An overall reduction in A_{EDM} with increasing momentum is present in all samples, as expected from the momentum dependent dilution function given by Equation 2.38. The impact of tracker acceptance is clear, manifesting as a significant decrease in sensitivity in the tracked samples compared to the *all decays* sample, which is most pronounced at low momentum.

3.7 Verifying the dilution function

The aforementioned dilution function, Equation 2.38, describes the variation in A_{EDM} with momentum in the case of 100% detector acceptance. This expression is vital in the extraction of the tilt angle, δ, from the measured values of A_{EDM} per momentum bin, and so must be verified. To accomplish this, A_{EDM} per 250 MeV, measured from the *all decays* reconstruction, was converted to dilution, d_{EDM}, according to the aforementioned

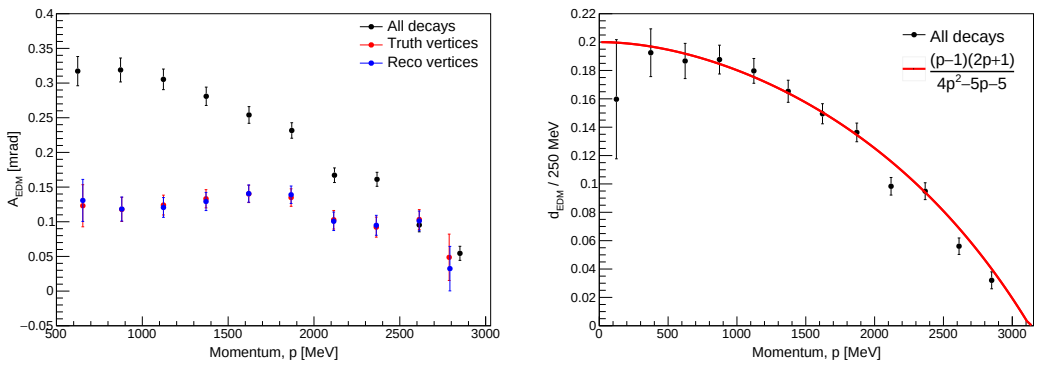

(a) **(b)**

Figure 5.7: Fit results from the momentum-binned analysis, showing: (a) A_{EDM} distributed against the mean momentum in each 250 MeV bin; (b) the dilution function, with a normalisation factor of one, overlaid on the tilt angle dilution factor, d_{EDM}, as measured using truth information and 100% detector acceptance (*all decays*).

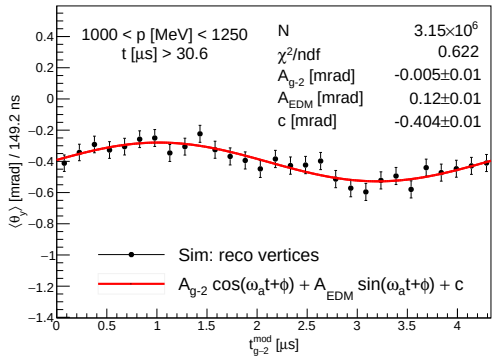

(a) 1000-1250 MeV.

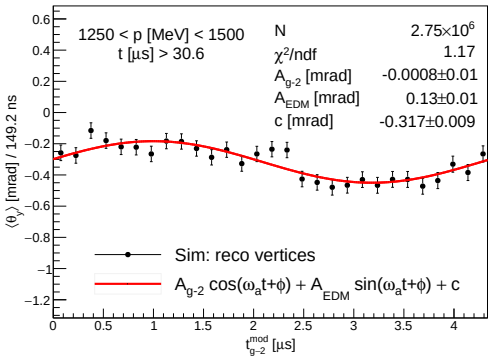

(b) 1250-1500 MeV.

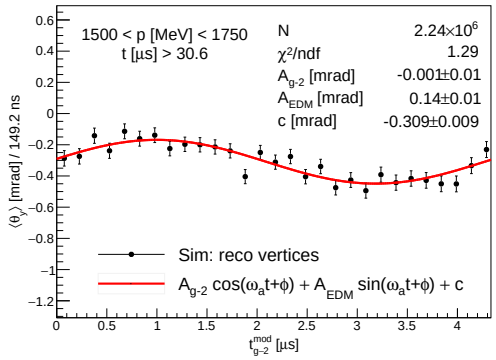

(c) 1500-1750 MeV.

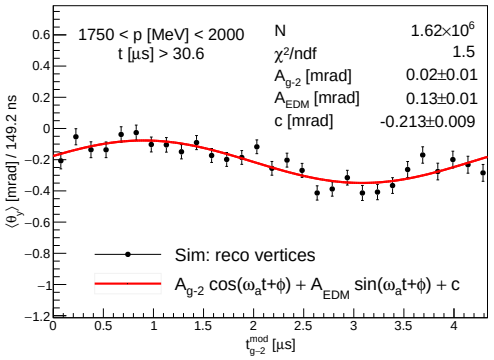

(d) 1750-2000 MeV.

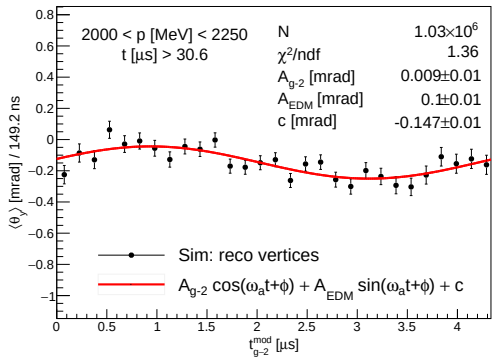

(e) 2000-2250 MeV.

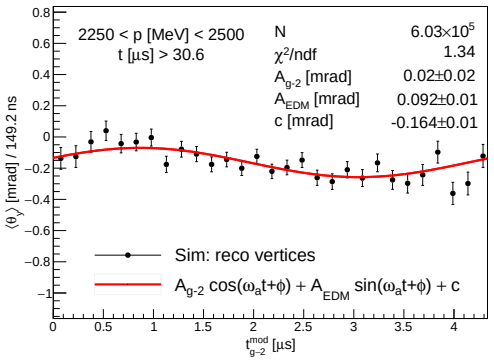

(f) 2250-2500 MeV.

Figure 5.8: Momentum-binned vertical angle oscillation fits for the *reco vertices* reconstruction. Tracker stations 12 and 18 are combined.

inputted δ of 1.69 mrad. The dilution function was then overlaid on the simulated distribution of d_{EDM}, demonstrating good agreement as shown by Figure 5.7b.

4 Tracker acceptance characterisation

By comparison of fit results from *all decays* to those from track vertices, presented in the previous section, it may be deduced that tracker acceptance plays a critical role in the observed dilution of the tilt angle. In this section, the impact of tracker vertical angle acceptance on the measured A_{EDM} as a function of momentum will be characterised.

4.1 Vertical angle acceptance

The vertical angle acceptance of the straw trackers is three-dimensional, with varying acceptance of θ_y in the radial, azimuthal, and vertical axes. Distributions of θ_y in each of these three dimensions are given in Figure 5.9, showing both two-dimensional histograms and their corresponding one-dimensional x-axis profiles. Little correlation is observed between θ_y and the radial decay position or azimuthal decay angle, while there is a clear negative correlation between θ_y and the vertical decay position, y, as shown by Figure

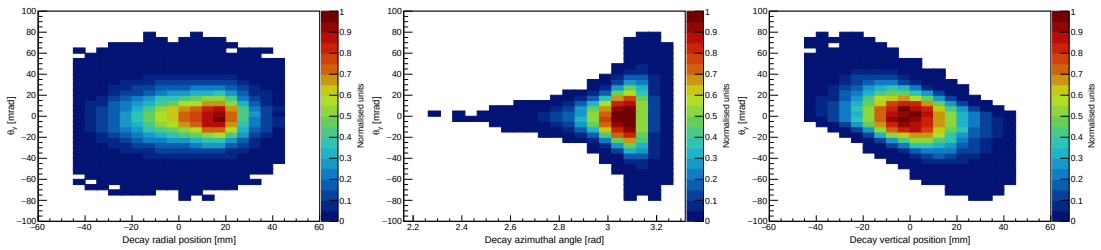

(a) Radial. **(b)** Azimuthal. **(c)** Vertical.

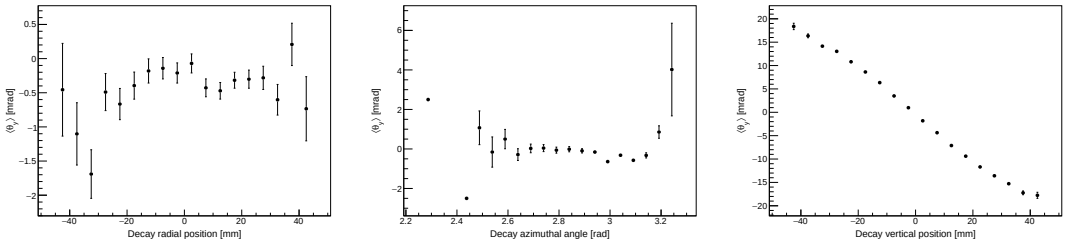

(d) Radial. **(e)** Azimuthal. **(f)** Vertical.

Figure 5.9: The distributions of accepted vertical angles in the radial, azimuthal, and vertical directions. A clear correlation is seen between θ_y and the vertical decay position. The azimuthal distributions presented in this figure are for station 12 only.

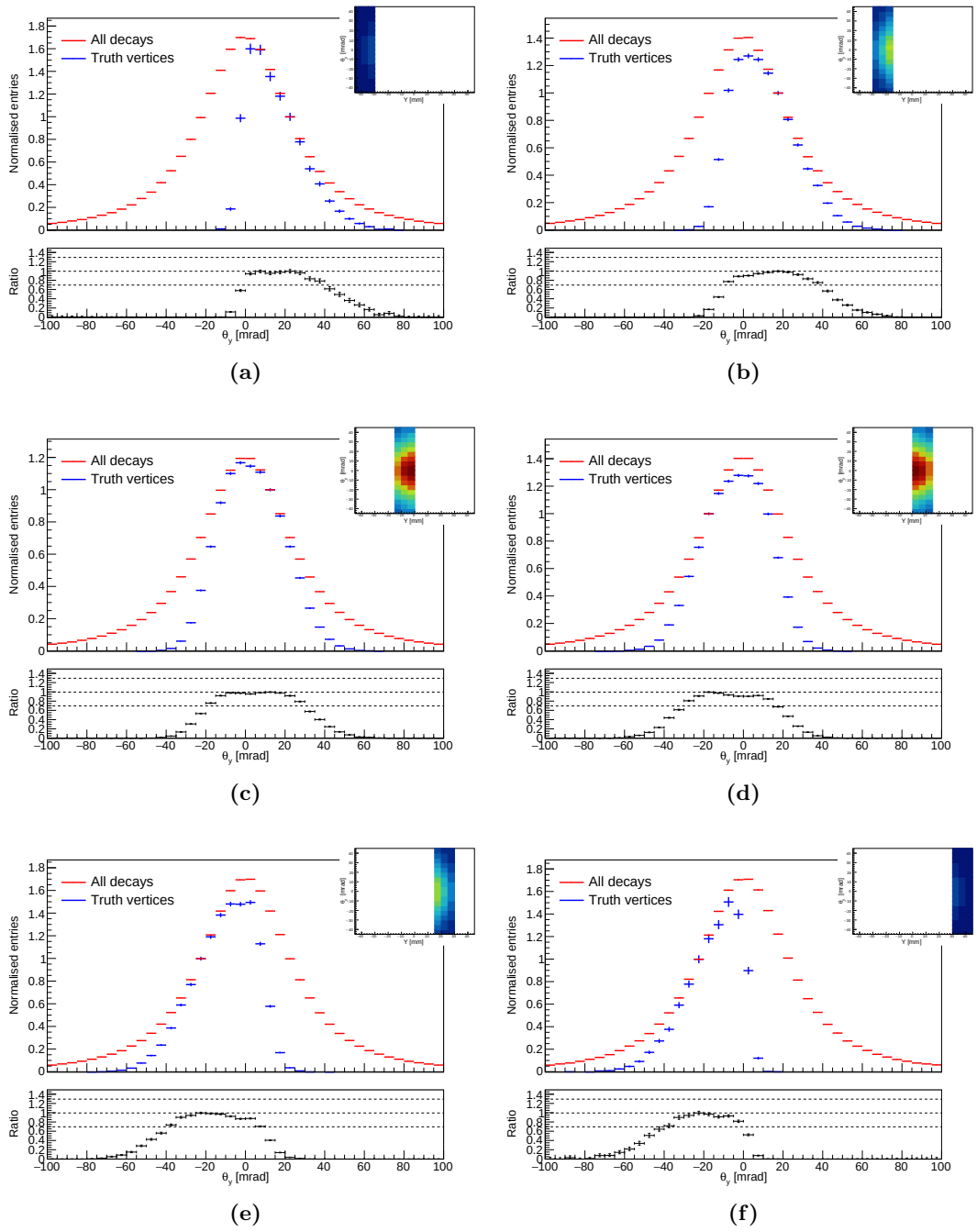

Figure 5.10: θ_y acceptance ratios in y intervals of 15 mm, indicated by secondary two-dimensional histograms. Positrons originating from the bottom of the storage region must carry a positive vertical component of momentum to be accepted by the straw trackers, and vice versa, resulting in negative correlation between θ_y and y. Histograms are formed from a Monte Carlo sample where vertices are a subset of decays, the one-dimensional distributions are normalised to their maximum ratio, and tracker stations are combined.

5.9f. For this reason, it was decided that only the vertical component of θ_y acceptance need be considered for the study presented in this section.

The physical origin for the correlation between the accepted θ_y and y is as follows: a positron originating from the bottom of the storage region, vertically lower than the mid-plane of the straw trackers, must possess a positive vertical component of momentum if it is to travel upwards and be accepted by the detector. The reverse is true for positrons originating at the top of the storage region. This effect is demonstrated by Figure 5.10, where one-dimensional distributions of θ_y for *truth vertices* and *all decays* are overlaid in 15 mm intervals of y. The physical (*all decays*) distributions of θ_y remains symmetrical, whereas the accepted (*truth vertices*) distribution is positive for a negative interval of y, and vice versa.

The distributions in Figure 5.10 are formed from an additional, pre-existing, sample of Monte Carlo with no injected EDM. In this sample, the true extrapolated track vertices are a subset of the truth decay parameters, which is essential when calculating the fraction of decays accepted by the trackers, and is not the case for the simulation datasets detailed in the earlier sections of this chapter.

4.2 Acceptance weightings

In order to assess the contribution of acceptance to the reduction of A_{EDM} between *truth/reco vertices* and *all decays*, shown in Figure 5.7a, the underlying histograms of $\theta_y(t)$ used to form the *all decays* vertical angle fits were weighted according to tracker 'acceptance maps' in θ_y versus y. This weighting procedure corrects the shape of the distribution of θ_y, so that *all decays* resembles *truth/reco vertices*, albeit with a different normalisation; however, in the context of this study, the normalisation of θ_y is not relevant. The weighted *all decays* distributions were then fitted for A_{EDM}, and results were compared with those measured from *truth vertices*.

Acceptance weightings were calculated by populating histograms of θ_y against y, once for *truth vertices* and then again for *all decays*, using the Monte Carlo sample with no injected EDM. The ratio of these two histograms, after being normalised according to the contents of its maximum bin, gives the aforementioned 'acceptance map': a two-dimensional distribution that may be used to weight θ_y according to y for that decay. An example acceptance map for stations 12 and 18 over all momentum is given in Figure 5.11.

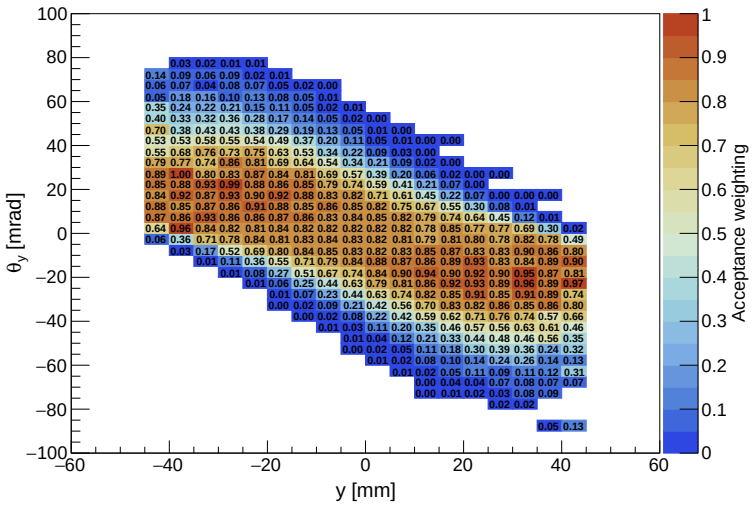

Figure 5.11: An acceptance map for all momentum, with tracker stations 12 and 18 combined.

In keeping with the momentum-binned method, treating each momentum interval as an independent analysis, maps were also produced in intervals of 250 MeV, with the *all decays* $\theta_y(t)$ distributions per bin being weighted according to the corresponding map for that momentum range. This approach also absorbs acceptance variations along the azimuthal axis, since the average momentum of accepted tracks is positively correlated with track extrapolation distance; that is, tracks originating from further away tend to possess a higher momentum, since low momentum positrons are more likely to curl out of the ring before reaching the detector. Acceptance maps were also produced for individual stations.

Distributions of A_{EDM} derived from both unweighted and weighted *all decays* samples, as well as *truth vertices*, are shown in momentum intervals of 250 MeV in Figure 5.12. As an estimate of the level of agreement between the weighted *all decays* distribution and the *truth vertices* distribution, the average number of standard deviations separating the data-points was found to be 1.13, 1.37, and 1.33 for stations 12, 18, and both stations combined respectively. This level of consistency indicates that the reduction of A_{EDM} measured by the trackers compared to *all decays* may be attributed to tracker acceptance.

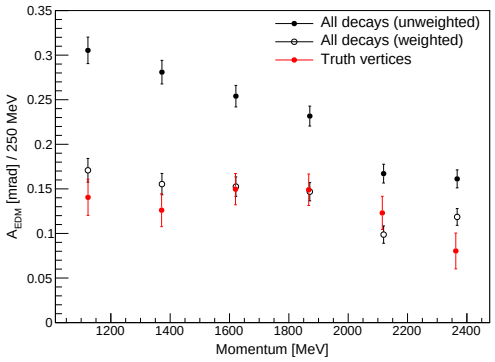

(a) Station 12.

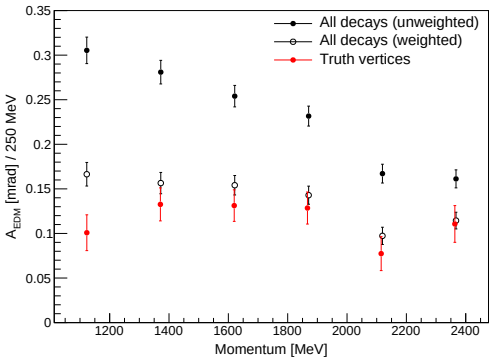

(b) Station 18.

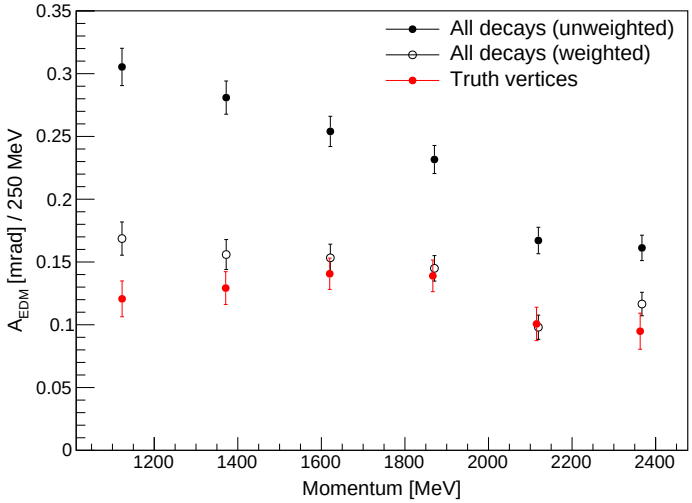

(c) Combined.

Figure 5.12: Distributions of A_{EDM} for *all decays*, acceptance weighted *all decays*, and the *truth vertices*. As discussed in the text, the acceptance weighted *all decays* distribution and the *truth vertices* distributions show a good level of consistency, indicating that the observed difference between A_{EDM} measured from *all decays* compared to *truth vertices* may be attributed to acceptance. Tracker stations 12 and 18 are combined.

4.3 The acceptance dilution factor and associated uncertainty

Having established that the reduction of A_{EDM} measured by the trackers compared to *all decays* may be attributed to tracker acceptance, an 'A_{EDM} acceptance factor' was calculated per momentum bin from the ratio of A_{EDM} measured using *truth vertices* to that measured from *all decays*. These factors may be defined as the tilt angle dilution factors associated with tracker acceptance.

As shown by Figure 5.13, the acceptance factors per momentum bin have an associated statistical uncertainty, which arises from the finite Monte Carlo dataset used to determine said factors. To estimate the corresponding uncertainty on the dilution

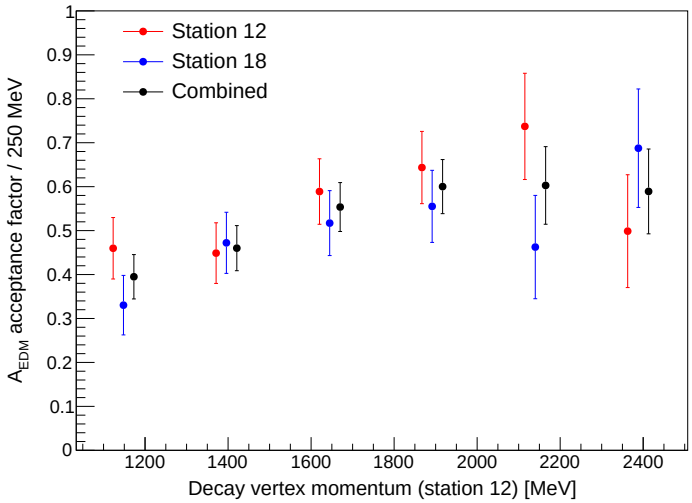

Figure 5.13: Acceptance factors versus momentum, or the tilt angle dilution factors associated with tracker acceptance, calculated from the ratio of A_{EDM} measured using *truth vertices* to that measured using *all decays*.

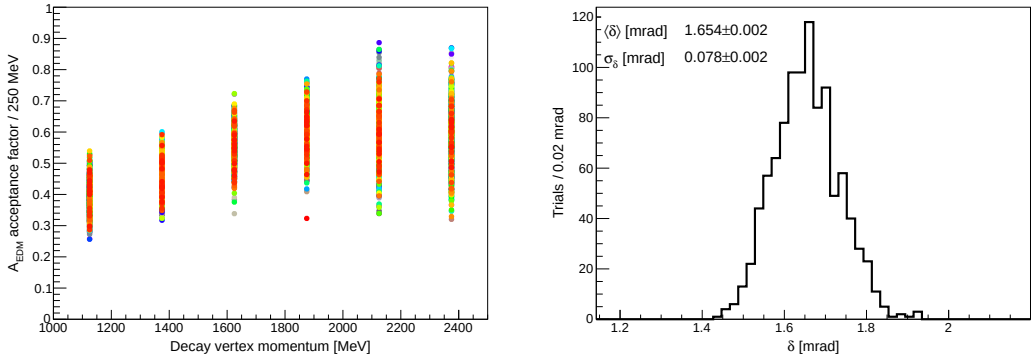

(a) **(b)**

Figure 5.14: Characterisation of the Monte Carlo statistical uncertainty associated with the dilution corrected tilt angle, showing: (a) 1000 sets of acceptance factors, drawn from Gaussian distributions with a width equal to the statistical uncertainty on the central value; (b) the distribution of dilution corrected tilt angles for measured track vertices, where the width is taken as the uncertainty in mrad.

corrected δ, 1000 sets of acceptance factors were randomly drawn from a Gaussian distribution with a mean equal to the acceptance factor in that bin and a width equal to its statistical uncertainty. Each set of acceptance factors is then used to correct the dilution of A_{EDM} for δ, using a method described in the following section, where the width of the resulting distribution of tilt angles is taken as the uncertainty in units of mrad. This is demonstrated in Figure 5.14.

5 Extracting the tilt angle

In order to extract the laboratory frame tilt angle, δ, from A_{EDM} at a particular momentum interval, a correction must be applied which is specific to the average momentum of that interval. In the case of 100% acceptance (*all decays*), the correction factor may be found by simple evaluation of the dilution function, Equation 2.38. In the case where tracker acceptance is included (*truth/reco vertices*), the correction factor is the product of the value obtained from the dilution function and the appropriate A_{EDM} acceptance factor.

Once the correction factors are applied, the result is a flat distribution of δ across momentum, which may be fitted with a zeroth order polynomial to obtain an uncertainty

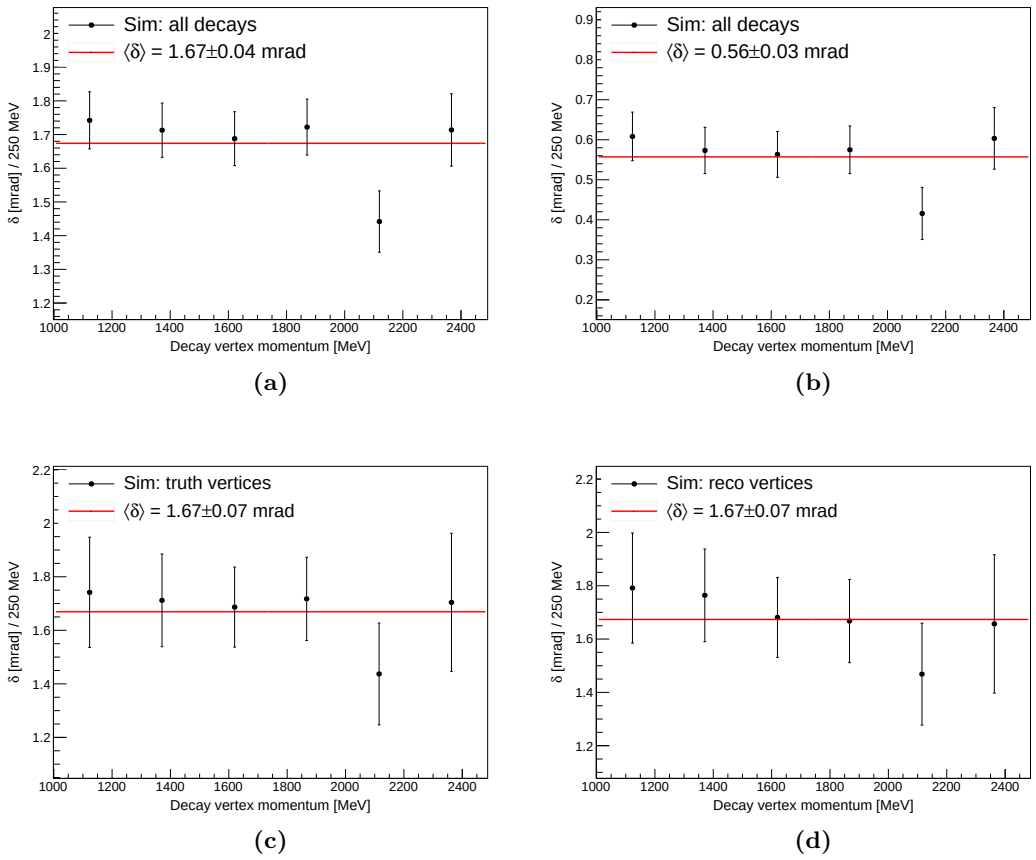

Figure 5.15: The dilution corrected δ per 250 MeV momentum bin, for: (a) *all decays* with a 30× BNL injected EDM, or a 1.69 mrad tilt; (b) *all decays* with a 10× BNL injected EDM, or a 0.594 mrad tilt; (c) *truth vertices*; and (d) *reco vertices*. Figures (c) and (d) both contain an injected 1.69 mrad tilt, and utilise the A_{EDM} acceptance factors shown in Figure 5.13. Tracker stations 12 and 18 are combined. All results are consistent with the injected tilt angle.

weighted average, $\langle\delta\rangle$. As illustrated in Figure 5.15, this procedure was performed for both the 30× and 10× BNL *all decays* samples, which have injected tilt angles of 1.69 mrad and 0.595 mrad respectively, along with the *truth/reco vertices* 30× BNL samples. Two injected EDM signals were used for purposes of checking for non-linearities between the level of dilution and the size of the injected signal, a possibility which is ruled out by the fact that all measured values of $\langle\delta\rangle$ are consistent with the injected tilt angle. Some deviation is observed at 2000-2250 MeV in all four distributions shown in Figure 5.15, which may be entirely attributed to a statistical fluctuation at the same momentum interval in Figure 5.7b.

6 Tracker global alignment characterisation

The characterisation of acceptance, described in the previous section, relies on the simulated detectors being orientated at the same relative position to the beam as in data. If this is not the case, then the acceptance correction uncertainty will receive some systematic contribution according to the size of the misalignment. In this section, a preliminary procedure for determining the size of this contribution from the straw tracker global alignment[3] error, in terms of an uncertainty on $\langle\delta\rangle$, will be described.

The straw tracker global alignment, hereafter referred to as 'alignment', has four parameters: the radial position, vertical position, radial angle, and vertical angle. These

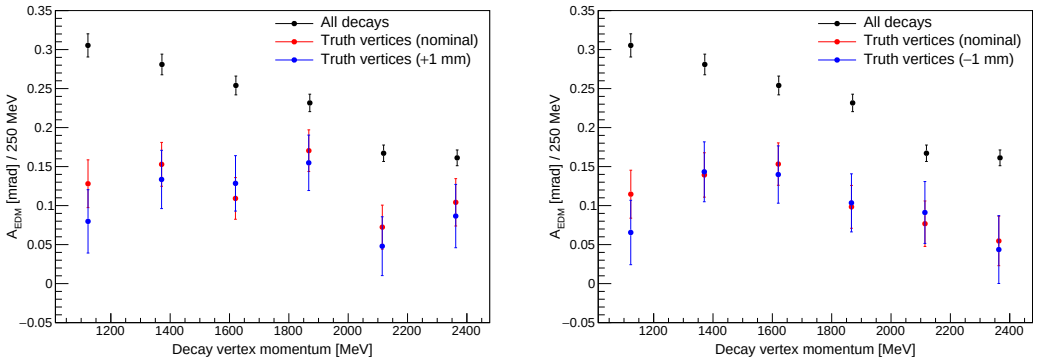

(a) Station 12 (+1 mm). **(b)** Station 18 (−1 mm).

Figure 5.16: Distributions of A_{EDM} with the tracker global vertical position shifted by (a) +1 mm for station 12 and (b) −1 mm for station 18, using the *truth vertices* reconstruction. Also shown is the nominal distribution from the *all decays* reconstruction.

[3]Global alignment refers to the absolute position of the tracker stations in the experiment's global coordinate system. This is distinct from internal alignment, which pertains to the relative position of the individual tracker modules. Alignment is discussed in detail in [85].

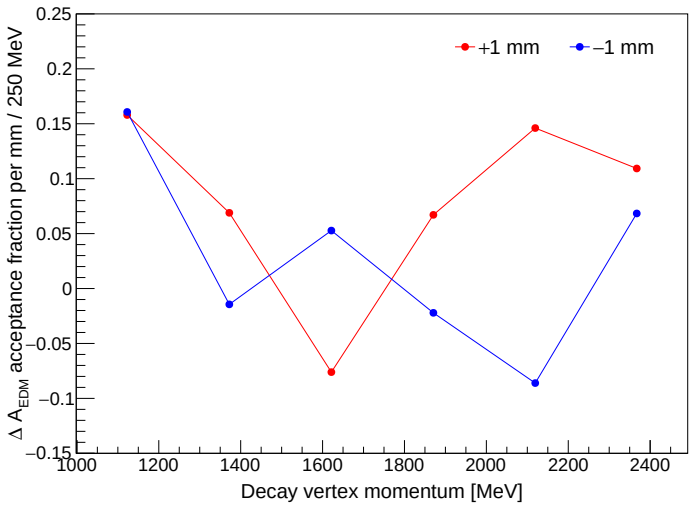

Figure 5.17: The variation in A_{EDM} acceptance factor with the tracker global vertical position shifted by ± 1 mm.

parameters are precisely measured via laser survey [85], with an uncertainty associated with each. In the context of the vertical θ_y acceptance uncertainty, the most relevant parameters are the vertical position and vertical angle. In the following preliminary study, only the vertical position, which has an uncertainty of ± 0.6 mm [86], is considered.

In order to begin propagating the vertical position alignment error through to an uncertainty on $\langle \delta \rangle$, the vertical alignment parameter was varied in simulation and the resulting shift in A_{EDM} was measured. In each case, the vertical position alignment was varied by $+1$ mm for station 12 and -1 mm for station 18. Due to practical constraints, only a subset of the sample described in Section 1 was available for reconstruction, which manifests an increased statistical uncertainty on A_{EDM}. The resulting distributions of A_{EDM} against momentum are shown in Figure 5.16.

The change in the A_{EDM} acceptance factor per mm is then approximated by subtracting the factors calculated at nominal vertical alignment from those calculated at ± 1 mm vertical alignment, shown in Figure 5.17. This uncertainty may then be estimated in terms of $\langle \delta \rangle$ by varying the nominal acceptance factor according to aforementioned ± 0.6 mm uncertainty, and taking the average shift in $\langle \delta \rangle$ as the uncertainty.

The procedure described in this section makes the approximation that the uncertainties associated with A_{EDM} are 100% correlated between the nominal and shifted samples, that is, the sets of tracks in both samples are derived from the same set of positrons. This is an inaccuracy, although the exact level of correlation is not known

at present, and so the possibility that the variation seen in Figures 5.16 and 5.17 is due to statistical fluctuations cannot be excluded. Because of this, and the fact that the contributions from the global tracker vertical angle is not yet included, the global alignment uncertainty described here must be considered preliminary.

7 Summary and outlook

The large-scale Monte Carlo simulation efforts outlined in this chapter have been shown to be vital to the development and verification of the tracker-based muon EDM analysis technique. The analysis procedure was demonstrated by use of a primary sample with an injected EDM of 5.4×10^{-18} e·cm (30× the BNL upper limit [4]), and a secondary sample with an injected EDM of 1.8×10^{-18} (10× BNL). The momentum-binned approach to fitting the vertical angle oscillation was introduced and motivated, based on the variation of $\langle\theta_y\rangle$, and the dilution of δ, with momentum. The decay asymmetry and dilution functions, Equations 2.35 and 2.38, were verified, and the impact of tracker acceptance on the dilution of observed angle A_{EDM} was characterised. Critically, this enables δ to be extracted from the measured A_{EDM}, producing results consistent with expectation, as shown. Finally, procedures were developed for estimating the contributions to the uncertainty on δ from the acceptance correction, including the contribution from the Monte Carlo statistical uncertainty, and, preliminarily, the contribution from global vertical alignment.

Moving forward, a greater number of events will be folded into the Monte Carlo datasets used to characterise the contribution from tracker acceptance to the dilution of δ, thereby reducing the statistical uncertainty associated with the A_{EDM} acceptance factors, and assisting in the analysis of the global alignment uncertainty. Additionally, the variation in A_{EDM} arising from the tracker vertical tilt angle error will be incorporated into said alignment uncertainty.

Chapter 6

The Run-1 muon EDM search

In this chapter, a blinded search for a muon EDM using straw tracker detectors in E989 Run-1 will be presented. Section 1 will detail the blinding procedure, which is designed to ensure that the analysis is unbiased. In Section 2, a direct measurement the EDM vertical angle oscillation will be shown, and Section 3 will provide a thorough assessment of sources of systematic uncertainty in that analysis. Finally, in Section 4, the expected upper limit on the EDM of the muon will be estimated, based on the uncertainty associated with the combined Run-1 result.

1 Blinding

The problem of bias, unconscious or otherwise, presents a challenge in any scientific experiment. To undertake an objective analysis, the central value of the result must be treated as arbitrary until all sources of systematic uncertainty have been identified and minimised. To this end, the EDM signal is blinded so that the measured vertical angle in-phase with the EDM oscillation, A_{EDM}, is hidden.

The blinding procedure for the EDM search utilises the same underlying blinding software used in the ω_a analysis[1], described in [29]. Here, a unique blinding phrase (a string), S, is used as a seed for a Mersenne Twister pseudo-random number generator [87], the output of which is designed to be used to draw a blind ppm offset on ω_a from a uniform distribution with Gaussian tails. In the context of the EDM search, the value drawn from this distribution is used as a multiplying factor on the BNL EDM limit, $|d_\mu| < 1.8 \times 10^{-19}$ e·cm [4], giving the magnitude of a blind EDM signal. This signal is then superimposed on the data by first converting it into a blind observed EDM angle, $A_{\mathrm{EDM}}^{\mathrm{BLIND}}$, by applying the appropriate dilution factor from the decay asymmetry,

[1] The ω_a analysis is double-blinded, utilising both software and hardware level blinding.

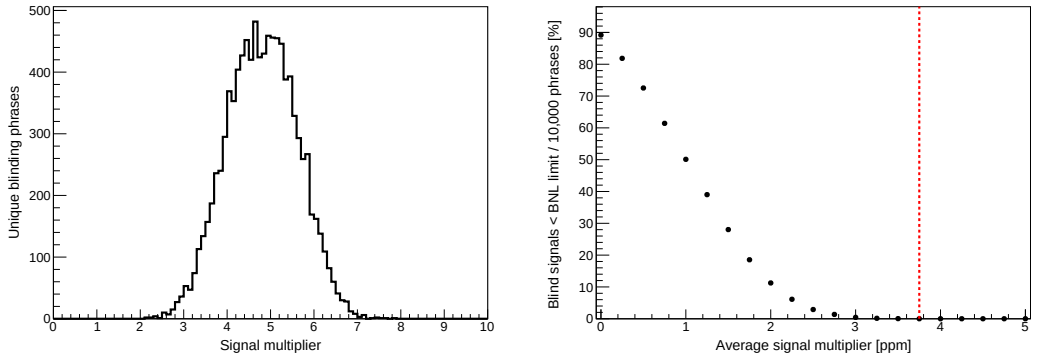

(a) **(b)**

Figure 6.1: The EDM blind signal multipliers, showing: (a) the distribution of multipliers from 10,000 unique blinding phrases; (b) a scan over the average signal multiplier parameter, G, showing how any value of G greater than 3.75 is sufficient to ensure that 100% of the blind signal multipliers drawn from the aforementioned distribution are larger than the BNL EDM upper limit.

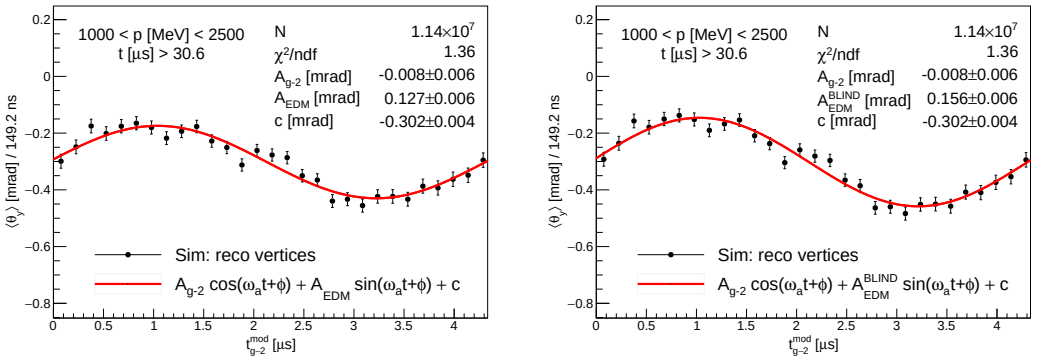

(a) Unblinded. **(b)** Blinded.

Figure 6.2: The EDM blinding applied to simulated track decay vertices with an injected muon EDM, demonstrating how the blinding procedure exclusively modifies the parameter A_{EDM}.

Lorentz boost, and tracker acceptance for a the appropriate momentum interval. The total vertical angle oscillation, as measured in the blinded analysis, is then

$$\theta_y^{\text{BLIND}}(t) = \theta_y(t) + A_{\text{EDM}}^{\text{BLIND}}(G, S) \cdot \sin(\omega_a t + \phi), \tag{6.1}$$

where ϕ is the anomalous precession phase. The constant G is the average signal multiplier, or the average value of the flattened Gaussian distribution described above. This distribution is shown in Figure 6.1a, for 10,000 unique blinding phrases, with chosen parameters of 0.25 for the width of the uniform section of the distribution, a width of

0.7 for the Gaussian tails, and a value of 4.81 for G. This value was selected to ensure that the injected signal is always larger than the BNL limit, as shown in Figure 6.1b: with a red dashed line indicating the smallest value of G where zero out of 10,000 trial blinding phrases resulted in a signal less than the BNL limit[2].

A demonstration of the blinding applied to simulated track decay vertices with an known injected EDM signal, as detailed in the previous chapter, is shown in Figure 6.2. Critically, this demonstrates that the blinding increases the measured EDM angle without modifying the other fit parameters. Separate blinding phrases are used for simulation and data, and all Run-1 datasets share a common phrase.

2 Fitting the vertical angle oscillation

In this section, blinded direct measurements of the EDM vertical angle oscillation in Run-1 are described. Both simultaneous and momentum-binned vertical angle oscillation fits, over a momentum range of 1000-2500 MeV, are presented. An example of underlying vertical angle distribution is shown, for Run-1a, in Figure 6.3, and widths of the vertical angle distributions for each Run-1 dataset are summarised in Table 6.1.

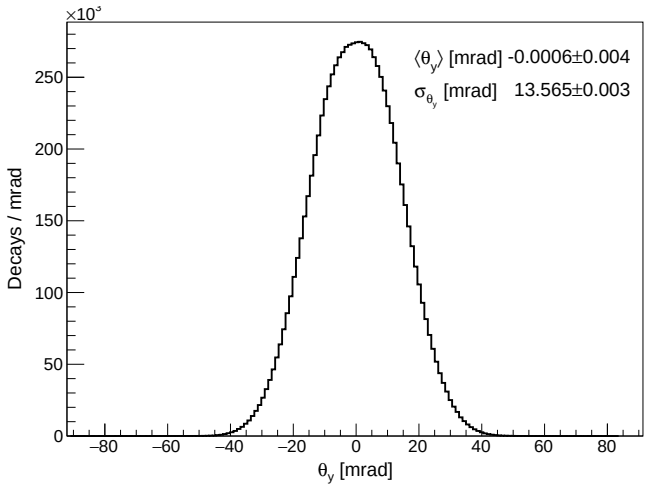

Figure 6.3: The distribution of θ_y for the Run-1a dataset (1000-2500 MeV).

Dataset	Run-1a	Run-1b	Run-1c	Run-1d
σ_{θ_y} [mrad]	13.565 ± 0.003	13.598 ± 0.003	13.579 ± 0.002	13.635 ± 0.002

Table 6.1: The widths of the θ_y distributions in Run-1 (1000-2500 MeV).

[2]The exact value of 4.81 was chosen for purely aesthetic reasons, besides being greater than 3.75, it being approximately equal to the transcendental number $(((i)^i)^i)^i$.

2.1 Fits for the anomalous precession oscillation phase

As discussed in Chapters 2 and 5, the first part of the EDM analysis procedure involves fitting the oscillation in the number of high-momentum tracks (the number oscillation) to determine the anomalous precession frequency phase, ϕ. To this end, fits to the time-modulated number oscillation with the five parameter function, Equation 2.14, for each of the four Run-1 datasets are shown in Figure 6.4; the measured phases are reported in Table 6.2. The impact of the number oscillation phase uncertainty on the EDM result is discussed in Section 3.5. Additionally, and as will be expanded upon in Section 3.2, the normal fit-start time of 30.6 µs ($7 \times T_{g-2}$) was extended to 52.4 µs ($12 \times T_{g-2}$) in the case of Run-1d.

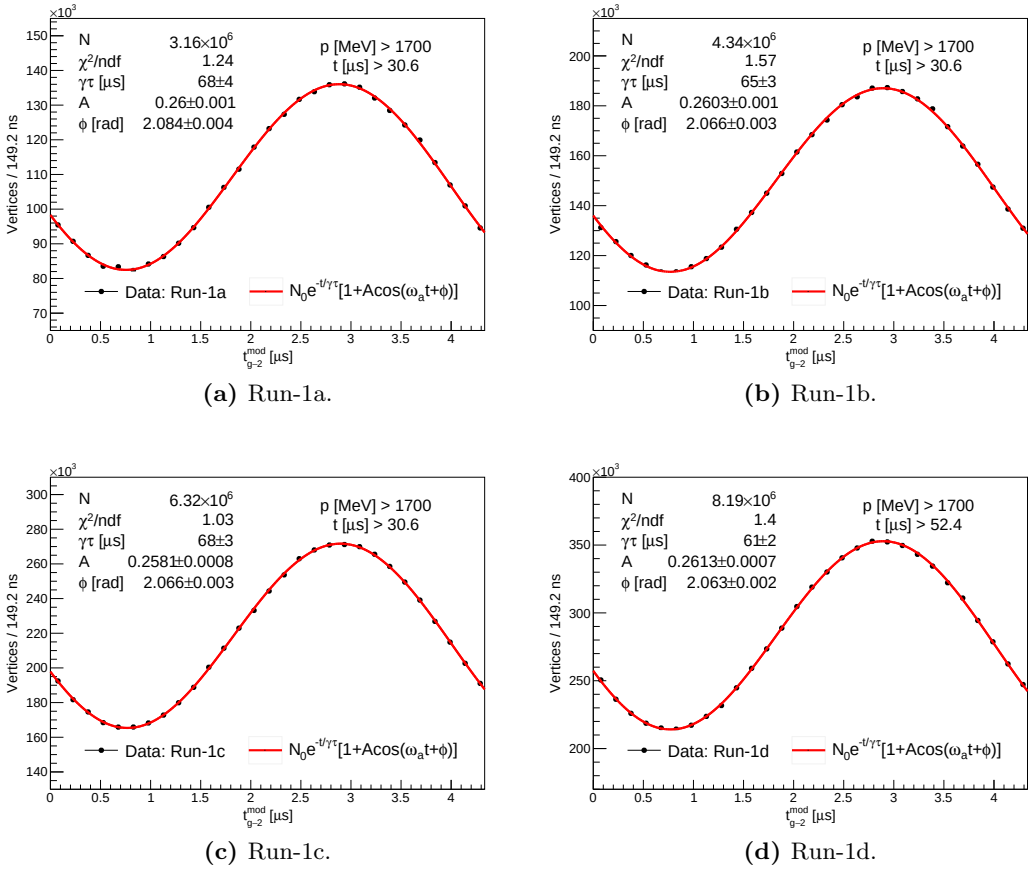

(a) Run-1a. **(b)** Run-1b. **(c)** Run-1c. **(d)** Run-1d.

Figure 6.4: Fits for the anomalous precession oscillation phase, ϕ, in Run-1.

Dataset	Run-1a	Run-1b	Run-1c	Run-1d
ϕ [rad]	2.084 ± 0.004	2.066 ± 0.003	2.066 ± 0.003	2.063 ± 0.002

Table 6.2: The measured anomalous precession oscillation phases, ϕ, in Run-1.

2.2 Simultaneous vertical angle oscillation fits

With the phase measured for each dataset, fits to the average vertical angle oscillation, $\langle\theta_y\rangle(t)$, in each dataset were initially performed over a wide range of momentum: 1000-2500 MeV, as discussed in Chapter 5. These fits do not constitute a part of the EDM analysis proper, which utilises a momentum-binned approach, but fitting momentum bins simultaneously still has value as a cross-check of the main result.

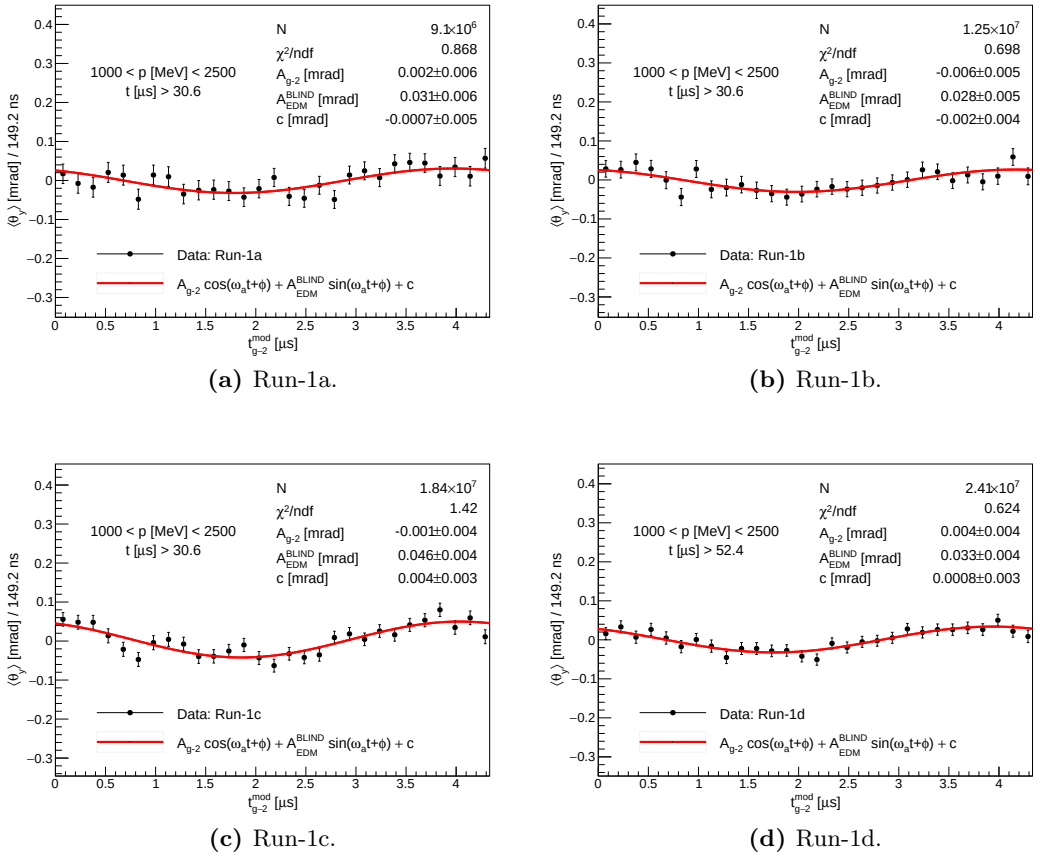

(a) Run-1a. **(b)** Run-1b.

(c) Run-1c. **(d)** Run-1d.

Figure 6.5: Blinded vertical angle oscillation fits. Tracker stations are combined.

Dataset	$A_{\mathrm{EDM}}^{\mathrm{BLIND}}$ [mrad]	δ^{BLIND} [mrad]
Run-1a	0.031 ± 0.006	0.41 ± 0.08
Run-1b	0.028 ± 0.005	0.37 ± 0.07
Run-1c	0.046 ± 0.004	0.61 ± 0.06
Run-1d	0.033 ± 0.004	0.44 ± 0.06

Table 6.3: Blinded vertical angle oscillation fit results. Tracker stations are combined.

These simultaneous fits, with tracker stations 12 and 18 combined, are shown in Figure 6.5. The results are reported in Table 6.3, which includes a blind laboratory frame tilt angle, δ^{BLIND}. This is calculated by Equation 2.38, using the constant dilution factor of $d_{\mathrm{EDM}} = 0.075 \pm 0.004$ for this momentum range, from Table 5.2. It is important to note that the δ^{BLIND} values presented in this section have no radial magnetic field correction applied, and all uncertainties are statistical. The fit χ^2/NDF values are <1 with the exception of Run-1c, which is typically indicates an overestimation of the uncertainty on $\langle \theta_y \rangle$ per time bin. However, the uncertainties in question are purely statistical and are therefore well motivated.

2.3 Momentum-binned vertical angle oscillation fits

As introduced in Chapter 5 Section 3, the muon EDM search described in this thesis employs a momentum-binned approach: where fits to vertical angle oscillation are performed in momentum intervals, in an effort to improve the accuracy of the dilution correction, and to minimise momentum-dependant variations in the average vertical angle.

Momentum-binned fits over a range of 1000-2500 MeV, in intervals of 250 MeV, are shown for each Run-1 dataset in Figures 6.8, 6.9, 6.10, and 6.11; where tracker stations are combined in each case. The measured values of $A_{\mathrm{EDM}}^{\mathrm{BLIND}}$ per momentum bin are presented for each dataset in Figure 6.6. Additionally, the corresponding fit χ^2/NDF

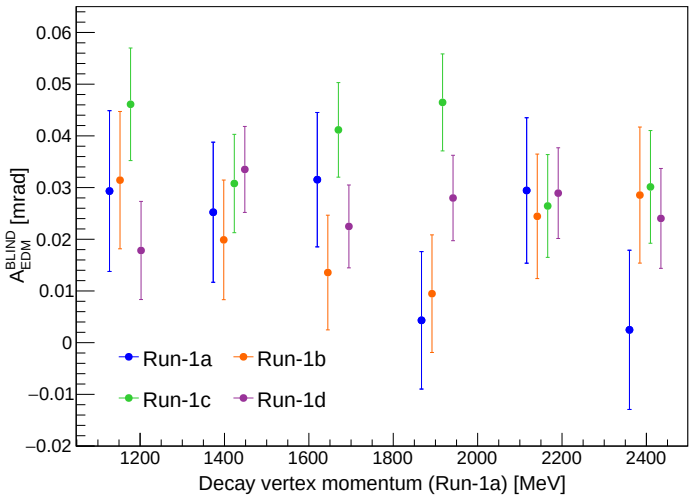

Figure 6.6: $A_{\mathrm{EDM}}^{\mathrm{BLIND}}$ per momentum bin for each Run-1 dataset. Tracker stations are combined.

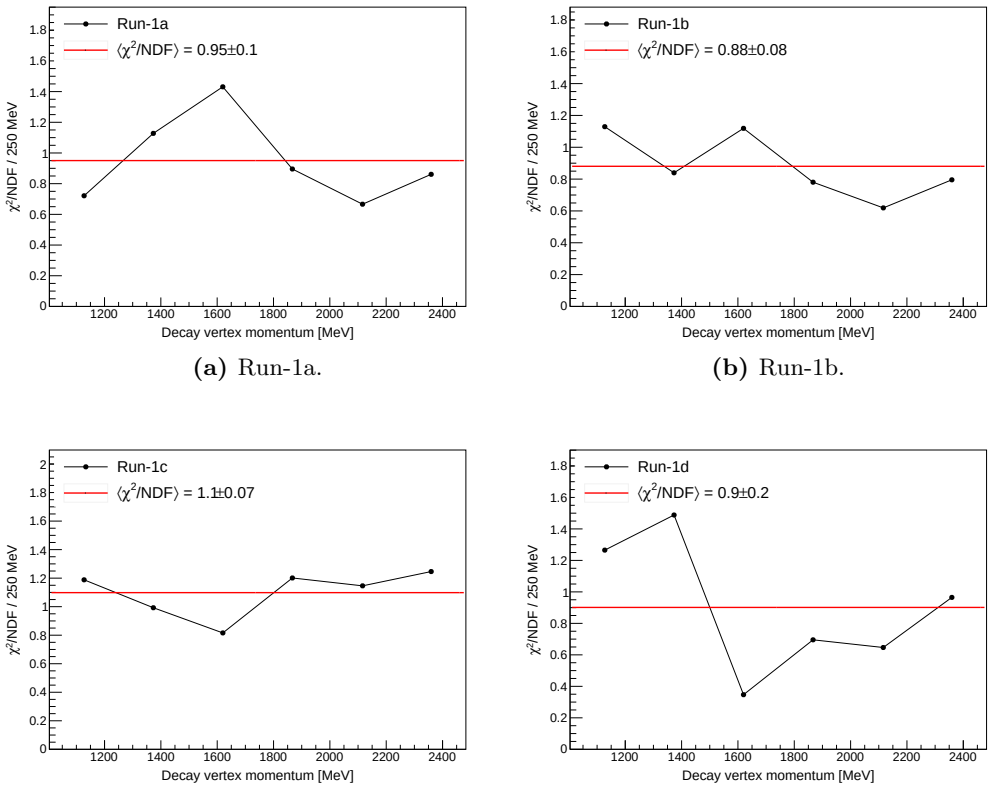

(a) Run-1a. **(b)** Run-1b.

(c) Run-1c. **(d)** Run-1d.

Figure 6.7: Fit χ^2/NDF per momentum bin for each Run-1 dataset, where a zeroth order polynomial fits gives the average in each case. These average values are consistent with one to within a maximum deviation of 1.5σ.

values are shown in Figure 6.7, with a zeroth order polynomial fit giving an estimate of the average, $\langle\chi^2/\text{NDF}\rangle$, over the full range of momentum. These averages are consistent with one to within a maximum of 1.5σ (in the case of Run-1b), indicating good quality fits.

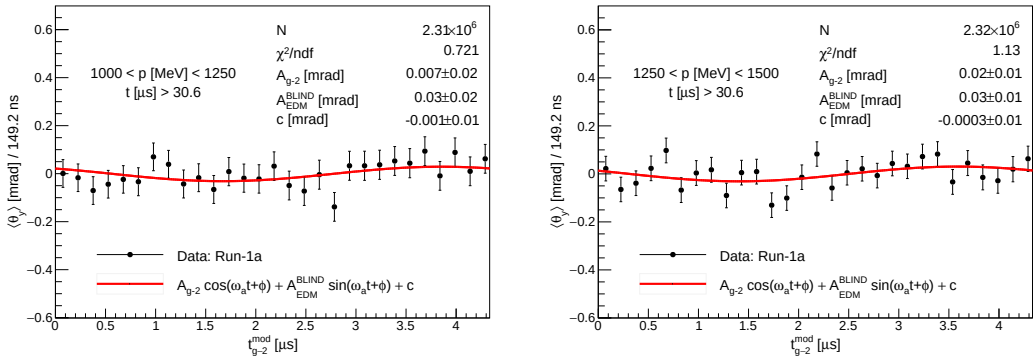

(a) 1000-1250 MeV.

(b) 1250-1500 MeV.

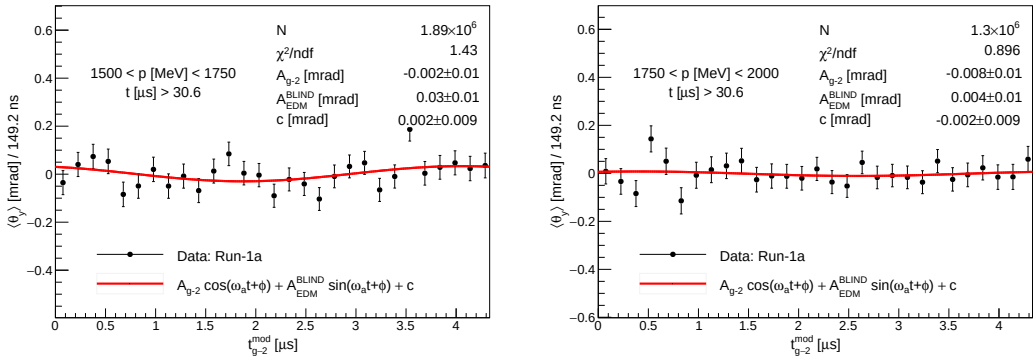

(c) 1500-1750 MeV.

(d) 1750-2000 MeV.

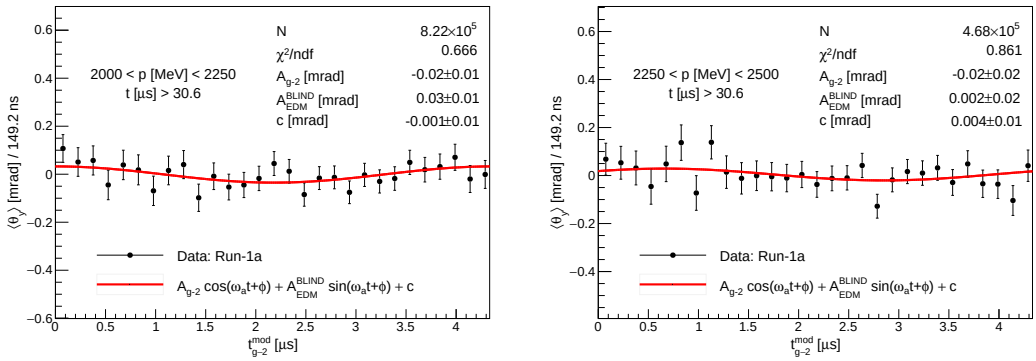

(e) 2000-2250 MeV.

(f) 2250-2500 MeV.

Figure 6.8: Momentum-binned vertical angle oscillation fits for Run-1a. Tracker stations 12 and 18 are combined.

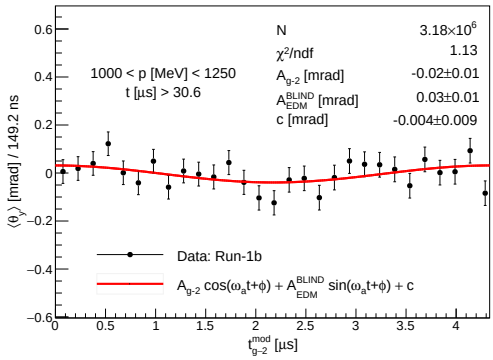

(a) 1000-1250 MeV.

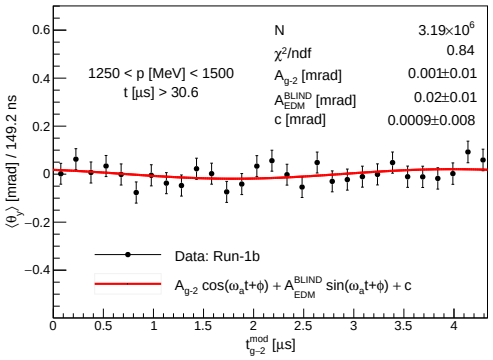

(b) 1250-1500 MeV.

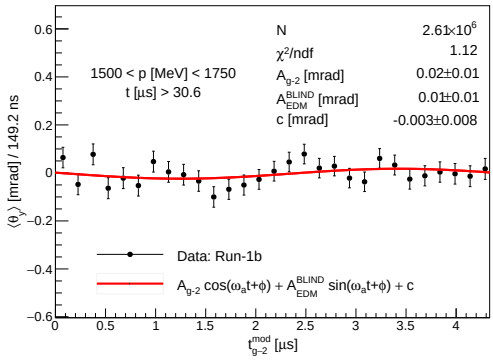

(c) 1500-1750 MeV.

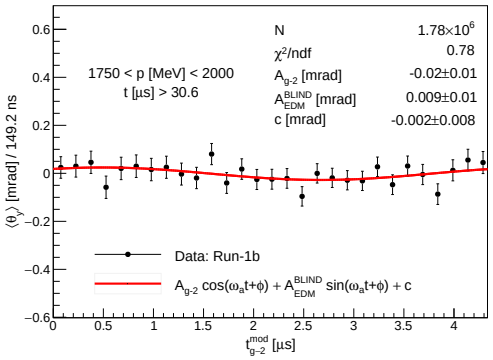

(d) 1750-2000 MeV.

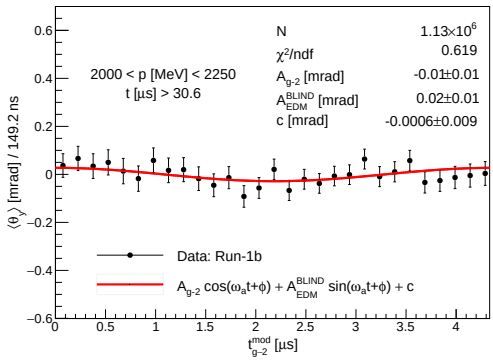

(e) 2000-2250 MeV.

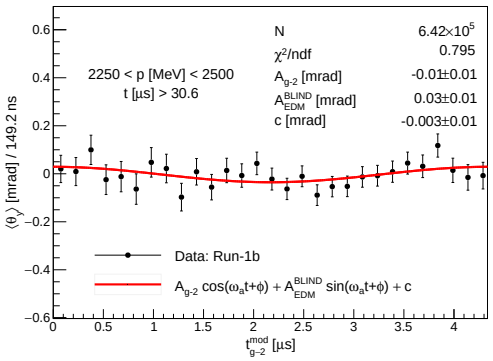

(f) 2250-2500 MeV.

Figure 6.9: Momentum-binned vertical angle oscillation fits for Run-1b. Tracker stations 12 and 18 are combined.

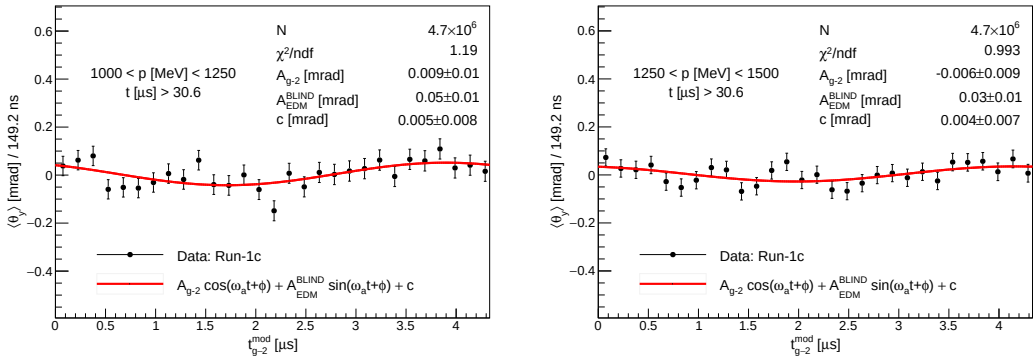

(a) 1000-1250 MeV.

(b) 1250-1500 MeV.

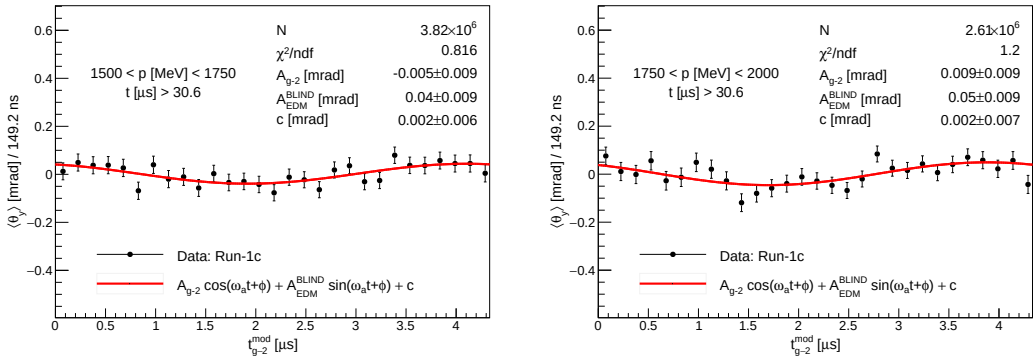

(c) 1500-1750 MeV.

(d) 1750-2000 MeV.

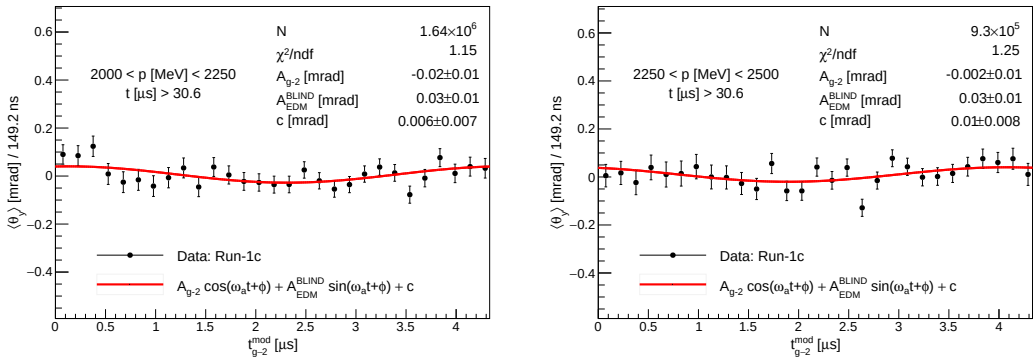

(e) 2000-2250 MeV.

(f) 2250-2500 MeV.

Figure 6.10: Momentum-binned vertical angle oscillation fits for Run-1c. Tracker stations 12 and 18 are combined.

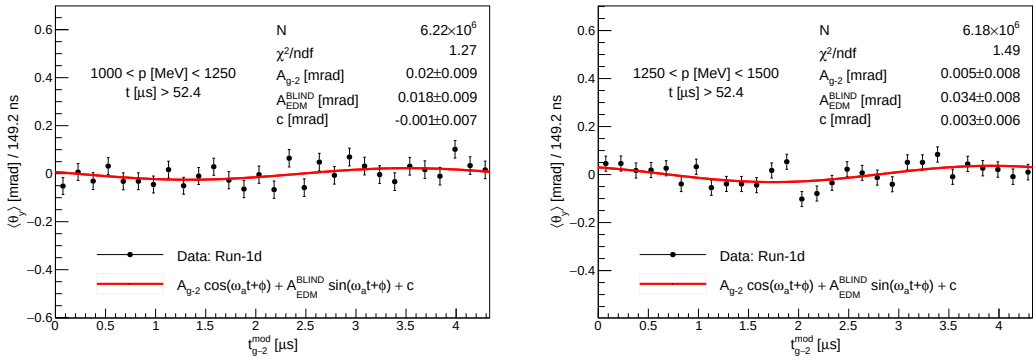

(a) 1000-1250 MeV.

(b) 1250-1500 MeV.

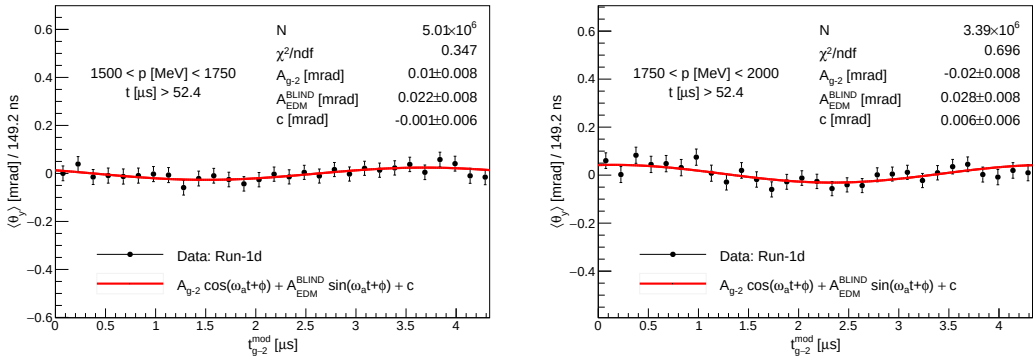

(c) 1500-1750 MeV.

(d) 1750-2000 MeV.

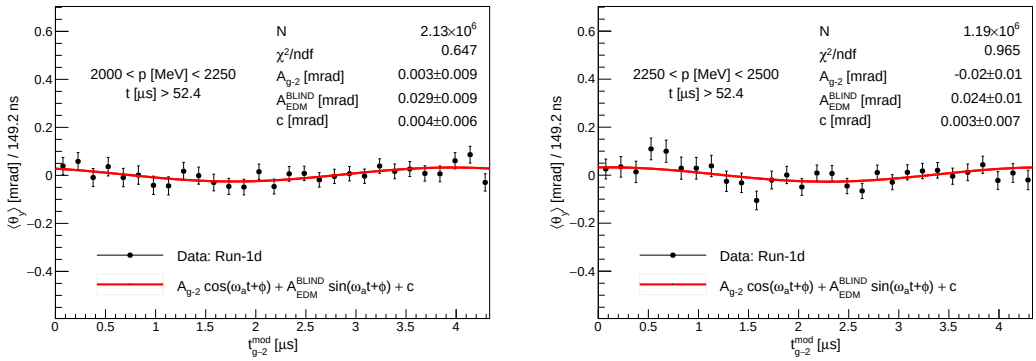

(e) 2000-2250 MeV.

(f) 2250-2500 MeV.

Figure 6.11: Momentum-binned vertical angle oscillation fits for Run-1d. Tracker stations 12 and 18 are combined.

2.4 Extracting the tilt angle

The measured values of $A_{\mathrm{EDM}}^{\mathrm{BLIND}}$ per momentum bin are then corrected to extract the blind laboratory frame tilt angle, δ^{BLIND}, per bin. This is accomplished by use of the same procedure as is demonstrated in simulation in Chapter 5 Section 5: where the dilution correction factor is found by evaluation of Equation 2.38, at the average momentum of each bin, which is then scaled by the appropriate A_{EDM} acceptance factor to obtain the total correction per momentum bin.

The resulting distributions of δ^{BLIND} across momentum are fitted with a zeroth order polynomial for the uncertainty weighted average, $\langle\delta^{\mathrm{BLIND}}\rangle$, which are shown in Figure 6.12, with tracker stations 12 and 18 combined. The measured average blinded tilt angles, $\langle\delta^{\mathrm{BLIND}}\rangle$, are summarised in Table 6.4, where all uncertainties are statistical.

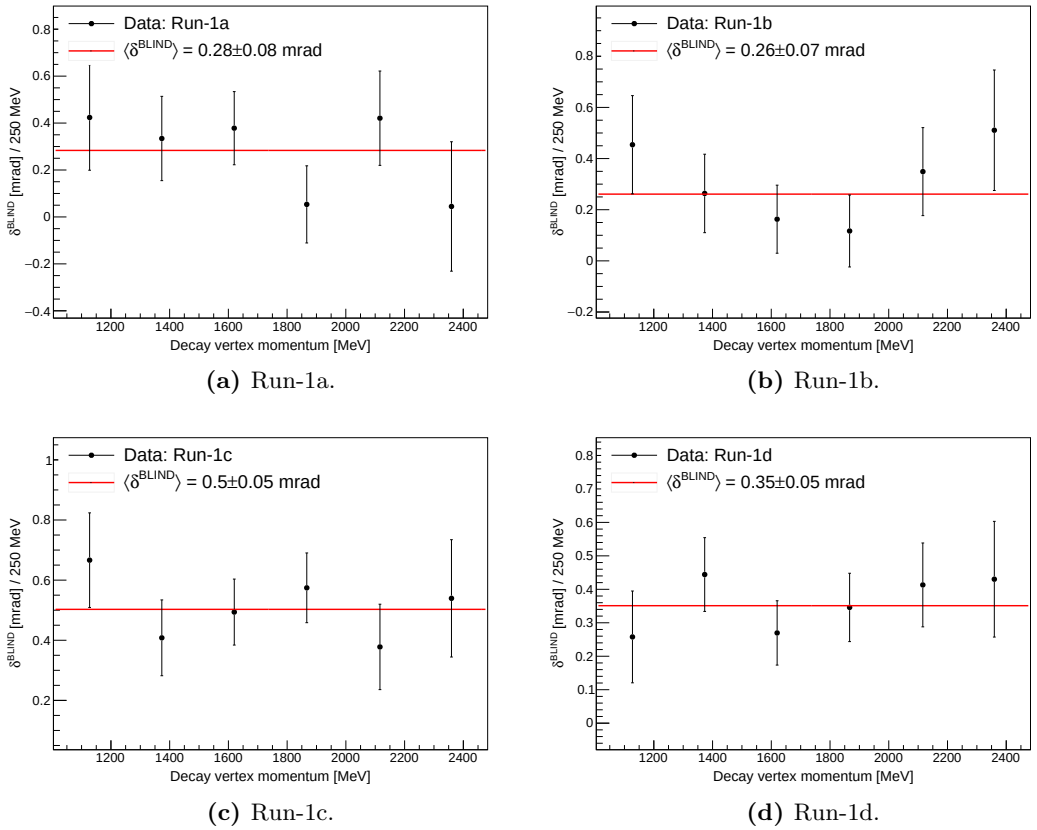

(a) Run-1a. **(b)** Run-1b.

(c) Run-1c. **(d)** Run-1d.

Figure 6.12: δ^{BLIND} per momentum bin for each Run-1 dataset, with a zeroth order polynomial fit giving an uncertainty weighted average. Tracker stations 12 and 18 are combined.

Dataset	$\langle\delta^{\mathrm{BLIND}}\rangle$ [mrad]		
	Station 12	Station 18	Combined
Run-1a	0.42 ± 0.10	0.06 ± 0.10	0.28 ± 0.08
Run-1b	0.25 ± 0.09	0.25 ± 0.10	0.26 ± 0.07
Run-1c	0.51 ± 0.07	0.46 ± 0.08	0.50 ± 0.05
Run-1d	0.36 ± 0.06	0.34 ± 0.07	0.35 ± 0.05

Table 6.4: Dilution corrected δ^{BLIND} results for the momentum-binned analysis.

3 Systematic uncertainties, checks, and corrections

3.1 The damaged ESQ resistors in Run-1

Following the completion of data taking in Run-1, it was discovered that two out of the 32 resistors in the ESQ charging system had become damaged. As a consequence, the affected plates (Q1) possessed a slower RC (resistor-capacitor) time constant than designed [29][30]. The resistors in question continued to deteriorate throughout Run-1, necessitating a delayed fit start-time in the Run-1d ω_a analysis of 50 µs (compared to 30 µs). The significance of this, in the context of the EDM search, is that the movement of the beam in the x-y plane, which is normally associated with scraping, continues much later into the fill than intended: modifying the average accepted vertical angle. The damaged resistors and their repercussions are referenced again in the following sections.

3.2 Fit start-time scans

The stability of the fit parameter $A_{\mathrm{EDM}}^{\mathrm{BLIND}}$ over a range of in-fill fit start-times is of particular interest in the context of the damaged resistors. To investigate this, fit start-time scans were performed using unmodulated fits over the range 1000-2500 MeV, where the minimum time of the fit was varied in units of T_{g-2}, from 30.6 µs to 117.9 µs. These scans are shown, with tracker stations 12 and 18 combined, for each Run-1 dataset in Figure 6.13. The parabolic red bands indicate the allowed 1σ variation, σ_Δ, between parameters measured from two datasets in the case where one is a subset of the other. This technique was developed specifically for the ω_a analysis at BNL [2], where in this case the variation is given by

$$\sigma_\Delta = \sqrt{\sigma_2^2 - \sigma_1^2}, \tag{6.2}$$

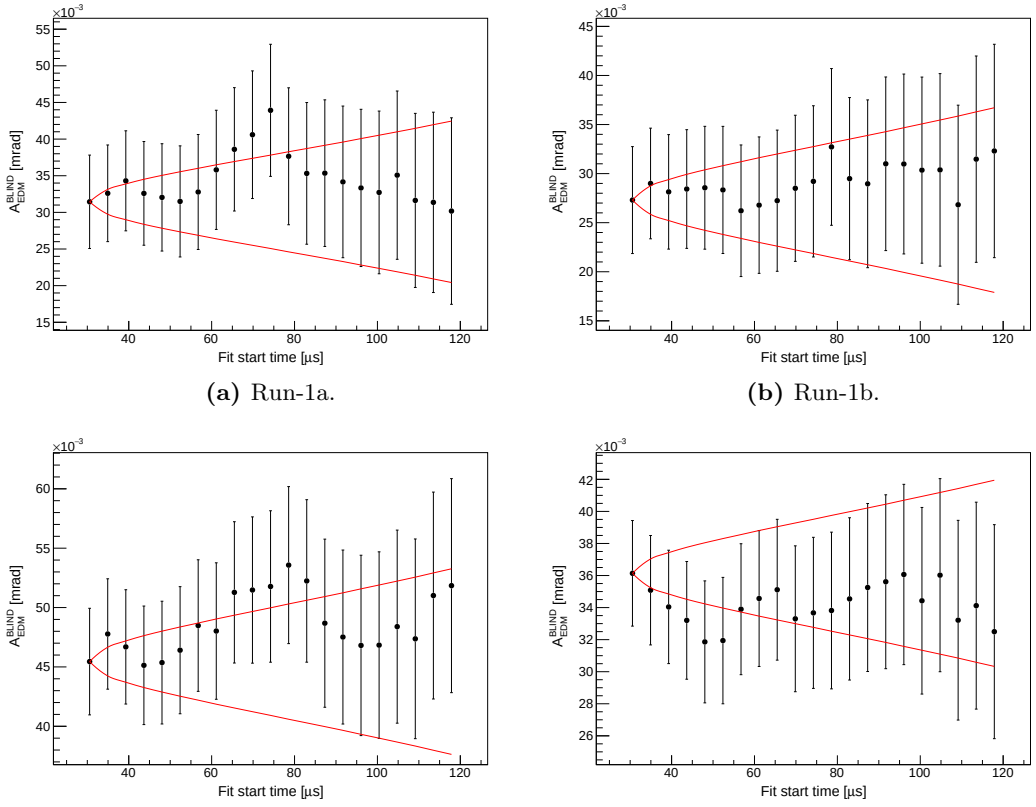

(a) Run-1a. **(b)** Run-1b.

(c) Run-1c. **(d)** Run-1d.

Figure 6.13: Fit start-time scans for unmodulated vertical angle fits over the range 1000-2500 MeV. As discussed in the text, the parabolic red bands indicate the allowed 1σ variation according to the changing statistical uncertainty across the scan. The deviation shown in Run-1d prior to 50 µs was taken as an indication that a delayed fit start-time should be used for this dataset.

where σ_2 is the uncertainty associated with the larger dataset (with an earlier fit start-time), and σ_1 indicates the uncertainty on the parameter measured using the sub-dataset.

In all cases, the majority of data points fall within the allowed deviation. However, in the case of Run-1d, the rapid decrease in $A_{\text{EDM}}^{\text{BLIND}}$ prior to 50 µs was taken as an indication that a later fit start-time should be used (52.3 µs or $12 \times T_{g-2}$), since this variation is likely a consequence of the deteriorating ESQ resistors.

3.3 The time and momentum dependence of the average vertical angle

As introduced in Chapter 5 Section 3.5, the average vertical angle, $\langle\theta_y\rangle$, demonstrates a momentum dependence in simulation, which is attributed to tracker acceptance effects in Section 4.2 of that chapter. This dependence is also present in Run-1 data, as illus-

trated in Figure 6.14, which also highlights the difference between the distributions of $\langle\theta_y\rangle(p)$ measured in Run-1 and those measured in simulation, as well as the variation between Run-1 datasets. The Run-1 datasets generally exhibit a more prominent average offset than simulation at low momentum, which is most pronounced in Run-1d. This likely indicates a contribution from damaged ESQ resistors, where the increased vertical movement of the beam, and changing vertical angle acceptance, would provide a logical explanation for the observed behaviour. At present, no adjustment to the acceptance correction is made to account for this difference, although a correction will be made before the results are unblinded.

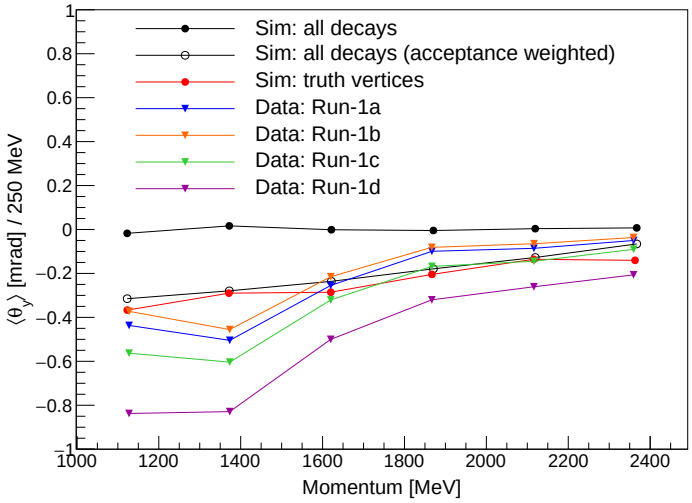

Figure 6.14: The momentum dependence of the average vertical angle, comparing the results from the simulation, discussed in Chapter 5, and the Run-1 datasets.

As a further consequence of the damaged ESQ resistors, $\langle\theta_y\rangle$ also acquires an in-fill time dependence, which, again, is most pronounced in Run-1d. This time dependence is parametrised by fitting $\langle\theta_y\rangle$, binned at the cyclotron period, with a fit function consisting of two exponential terms and a constant offset, c, as follows:

$$\langle\theta_y\rangle(t) = \frac{A}{\tau_A} e^{\frac{-t}{\tau_A}} + \frac{B}{\tau_B} e^{\frac{-t}{\tau_B}} + c. \tag{6.3}$$

The first term relates to the slow change in the electric field due to the damaged resistors, with an amplitude A and time constant τ_A. The second term contains an amplitude B and faster time constant, τ_B, which relates to the ~ 7 µs scraping period. Tracker stations are treated independently, with fits to station 12 data over the 1000-2500 MeV

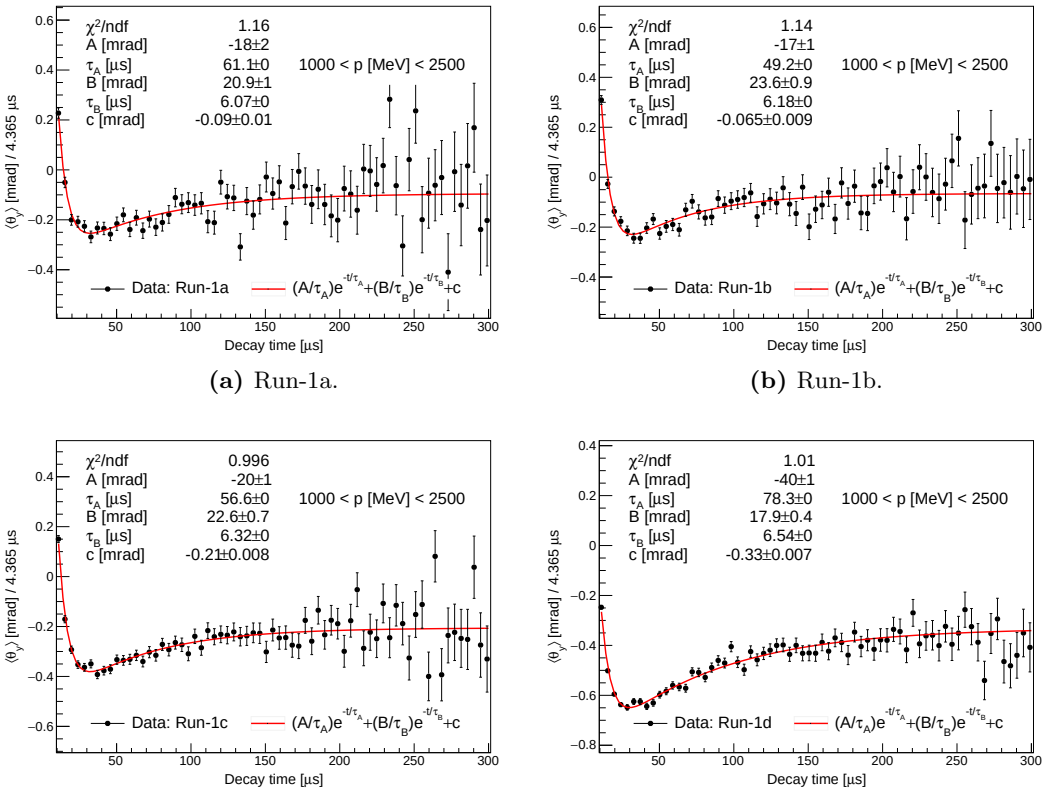

(a) Run-1a. **(b)** Run-1b.

(c) Run-1c. **(d)** Run-1d.

Figure 6.15: Double exponential fits to the in-fill time dependence of $\langle\theta_y\rangle$, for tracker station 12. This phenomenon is unique to Run-1, and is attributed to non-typical beam movement due caused by the two damaged ESQ resistors. The time constants, τ_A and τ_B, are fixed to the values reported by J. Mott in the Run-1 ω_a analysis [88].

	Run-1a	Run-1b	Run-1c	Run-1d	Avg.
$\Delta\langle\delta^{\text{BLIND}}\rangle$ [mrad]	-0.00996	-0.00862	-0.00679	-0.0148	-0.0100

Table 6.5: The change in $\langle\delta^{\text{BLIND}}\rangle$ following the $\langle\theta_y\rangle$ offset correction.

momentum range shown in Figure 6.15. The time constants are fixed to the values reported by J. Mott during the Run-1 ω_a analysis [88]. These fits are performed in momentum bins in order to perform a simultaneous correction of the momentum-dependent offset, using the parameter c as a proxy for $\langle\theta_y\rangle$, and the time-dependent variation by evaluation of the fit function at the positron decay time.

The impact of this correction is given in terms of the change in $\langle\delta^{\text{BLIND}}\rangle$, summarised for each dataset in Table 6.5, showing a small reduction with an average value in Run-1 of 10 µrad. No change is observed in the average fit χ^2/NDF, and the change in the uncertainty on $\langle\delta^{\text{BLIND}}\rangle$ is $\mathcal{O}(10^{-6})$ mrad, which is negligible.

3.4 Beam dynamics corrections

The muon beam does not propagate in a perfect static orbit. Beam dynamics effects, betatron oscillations in particular (introduced in Chapter 2 Section 4) modify the average position of the beam as a function of time; resulting in an oscillating average vertical angle at the relevant betatron frequency. Although the modulation of decay times at T_{g-2}, discussed in Chapter 5 Section 3.1, is designed to de-phase and therefore minimise oscillations such as this, their potential impact must be investigated nonetheless.

To assess the presence of additional oscillations in data, fast Fourier transforms (FFTs) were performed on the residual distributions from fits to the unmodulated vertical angle oscillation, binned in time at the cyclotron period. Modulated fits were not used in this case because the relatively low number of time bins results in poor resolution in the frequency domain. Fit residual FFTs are shown for each Run-1 dataset for all times after 30.6 µs in Figure 6.16, showing no clear peaks. However, the betatron

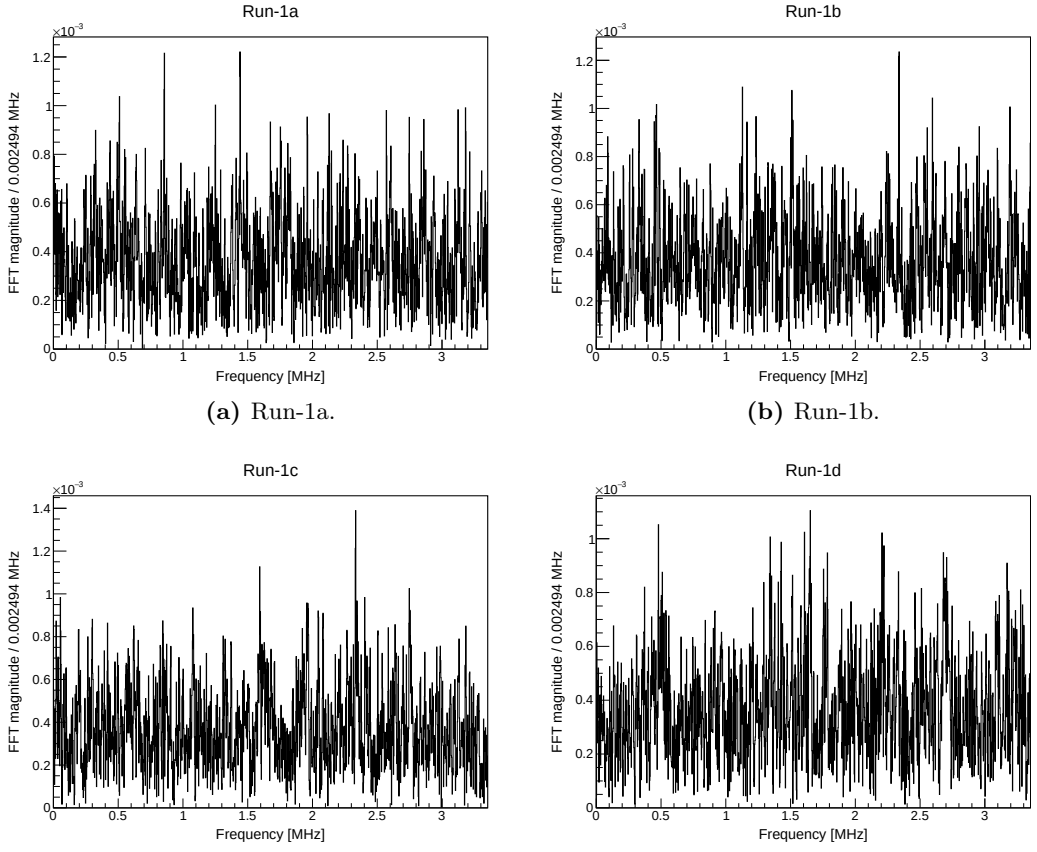

(a) Run-1a. **(b)** Run-1b.

(c) Run-1c. **(d)** Run-1d.

Figure 6.16: FFTs of the residual distributions from unmodulated vertical angle oscillation fits, from 30.6 µs onwards, showing no obvious peaks in the frequency domain.

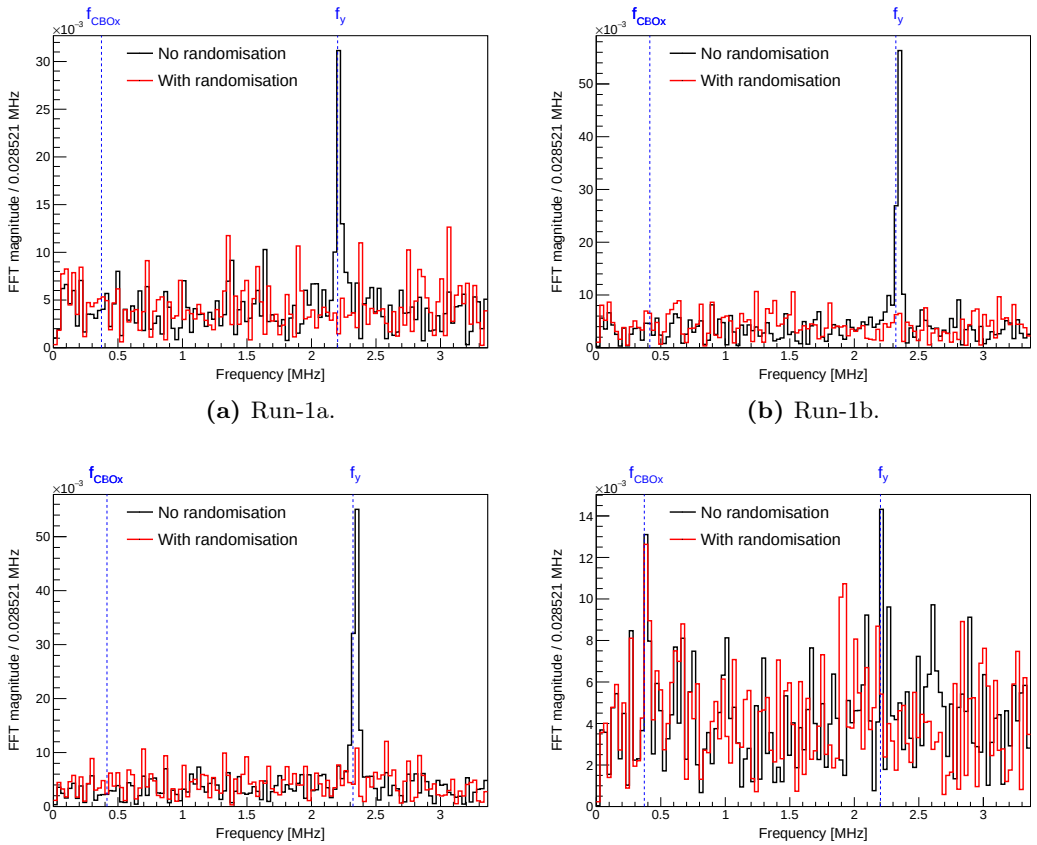

(a) Run-1a. **(b)** Run-1b.

(c) Run-1c. **(d)** Run-1d.

Figure 6.17: FFTs of the residual distributions from unmodulated vertical angle oscillation fits over a time range of 30.6-65.5 µs. The uncorrected black distributions show prominent peaks at the vertical betatron frequency, f_y, in all datasets except Run-1d, where it is significantly reduced. A small peak at the aliased horizontal betatron frequency, f_{CBOx}, is also visible in Run-1d. Uniform randomisation of decay times about $\pm T_{f_y}/2$ removes the vertical betatron oscillation peak, as shown by the corrected distributions in red.

oscillation amplitude decays exponentially with time, so FFTs were performed over earlier time range in-fill, 30.6-65.5 µs, where betatron motion is more prominent. These early-time FFTs are given by the black distributions in Figure 6.17, showing prominent peaks at the vertical betatron frequency, f_y, in all datasets with the exception of Run-1d, where it is greatly reduced. Additionally, the FFTs for Run-1d possess a small peak at the aliased horizontal betatron frequency, f_{CBOx}. The frequencies f_y and f_{CBOx} are listed in Table 3.1. To remove the vertical betatron oscillation, decay times were randomly drawn from a uniform distribution $\pm T_{f_y}/2$ about the measured time, where fit residual FFTs for the time randomised datasets are shown in red in Figure 6.17, with no peaks at f_y. Removal of the horizontal betatron oscillation in this way is

	Run-1a	Run-1b	Run-1c	Run-1d	Avg.
$\Delta\chi^2$/NDF	-0.243	-0.32	-0.40	0.00	-0.243
$\Delta\langle\delta^{\text{BLIND}}\rangle$ [mrad]	-0.0736	-0.118	0.0166	4.3×10^{-5}	-0.0437
$\Delta\sigma_{\langle\delta^{\text{BLIND}}\rangle}$ [mrad]	-0.00389	0.0126	0.0107	-1.0×10^{-6}	0.00485

Table 6.6: The impact of time randomisation on $\langle\delta^{\text{BLIND}}\rangle$, summarising the changes in: the average fit χ^2/NDF, the central value, and the uncertainty.

not possible due to its much longer time period, where randomisation would obfuscate a potential EDM oscillation. Since the f_{CBOx} peak is relatively small, as well as only being present in Run-1d – which also utilises a delayed fit start-time – no attempt to remove the horizontal betatron oscillation was made in this analysis. As a precaution, the fast rotation frequency was also removed using the time randomisation technique, in addition to binning at the cyclotron period.

The impact of time randomisation is assessed according to the change in $\langle\delta^{\text{BLIND}}\rangle$, where the values measured with time randomisation are subtracted from those measured without it. The change in the uncertainty, $\sigma_{\langle\delta^{\text{BLIND}}\rangle}$, and the average fit χ^2/NDF across momentum bins, are also considered. As is summarised in Table 6.6: the fit χ^2/NDF is, on average, significantly reduced with the inclusion of time randomisation; the average $\langle\delta^{\text{BLIND}}\rangle$ decreases by -0.0437 mrad; and the uncertainty is largely unaffected, increasing by 4.85 µrad, which is an order of magnitude less than the statistical uncertainty associated the largest dataset (Run-1d). The delayed fit start-time in Run-1d means that the impact on the results from this dataset is negligible.

3.5 Phase uncertainty assessment

The anomalous precession oscillation phase, ϕ is a fixed parameter in the EDM analysis, despite possessing an uncertainty, σ_ϕ. To evaluate the potential effect of this uncertainty on $\langle\delta^{\text{BLIND}}\rangle$, ϕ was fixed to a value $\pm\sigma_\phi$ and propagated through the analysis. The change in $\langle\delta^{\text{BLIND}}\rangle$ for both signs was found to be of the sub-µrad level, as shown in Table 6.7, and is therefore negligible.

Dataset	σ_ϕ [mrad]	$\Delta\langle\delta^{\text{BLIND}}\rangle$ [µrad]	
		$\phi + \sigma_\phi$	$\phi - \sigma_\phi$
Run-1a	3.62	0.187	−0.132
Run-1b	3.05	0.183	−0.393
Run-1c	2.55	0.117	−0.0740
Run-1d	2.21	0.0180	−0.0180

Table 6.7: The change in $\langle\delta^{\text{BLIND}}\rangle$ with the measured anomalous precession oscillation phase, ϕ, shifted by $\pm\sigma_\phi$.

3.6 Tracker vertical angle resolution

A further potential source of systematic uncertainty is the trackers' ability to resolve the average vertical angle, $\langle\theta_y\rangle$. To quantify this, the same simulation dataset as was employed in the tracker acceptance study, detailed in Chapter 5, was used to produce distributions of the true vertical angle subtracted from the measured (reco) vertical angle. The true and reco distributions of θ_y are shown in Figures 6.18a and 6.18b, and the distribution of the differences is shown in Figure 6.18c. Only tracks with momentum in the range of 1000-2500 MeV were used. The average vertical angle resolution is equal to the uncertainty on the mean, which is

$$\delta\langle\Delta\theta_y\rangle = 3\,\text{µrad}.$$

Given that the uncertainty on the mean for both true and measured θ_y distributions, formed from the same simulated dataset, is one order of magnitude larger than this, the contribution from tracker resolution to the uncertainty on A_{EDM}, and by extension $\langle\delta^{\text{BLIND}}\rangle$, can be assumed to be negligible. As an additional point, the distribution of $\delta\langle\Delta\theta_y\rangle$ per 100 MeV momentum bin is shown in Figure 6.18d: where the optimum resolution is obtained in the range 1000-2500 MeV, which is the same as is used in the analysis presented in this chapter.

3.7 Tracker acceptance

The correction required to scale the measured $A_{\text{EDM}}^{\text{BLIND}}$ to δ^{BLIND}, discussed in Section 2.4, relies on an acceptance correction with an associated statistical uncertainty from Monte Carlo, and a systematic uncertainty associated with tracker global alignment.

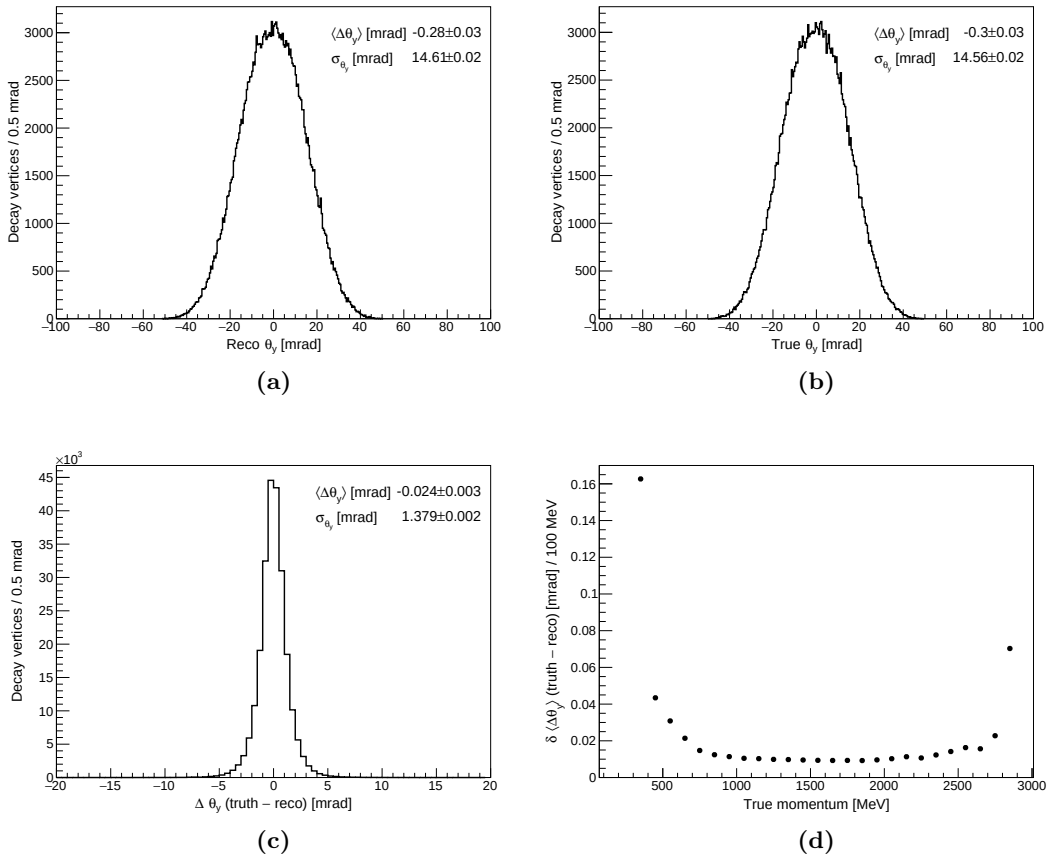

Figure 6.18: The straw tracker vertical angle resolution, showing: (a) the θ_y distribution for measured (reco) track decay vertices; (b) the θ_y distribution for truth decay vertices; (c) the distribution of truth minus measured θ_y, where the $\langle\theta_y\rangle$ resolution is given by the error on the mean; (d) $\langle\theta_y\rangle$ resolution in 100 MeV momentum intervals.

The procedure for assessing these uncertainties follows the method detailed in Chapter 5 Sections 4.3 and 6.

In the same manner as illustrated in Figure 5.14, the acceptance statistical uncertainty from simulation was taken as the width of a distribution of $\langle\delta^{\mathrm{BLIND}}\rangle$ results, populated via 1000 trials where the acceptance dilution factor per momentum bin was randomly drawn from a Gaussian distribution with a mean equal to the acceptance factor and a width equal to its statistical uncertainty. These distributions are shown in Figure 6.19 for each Run-1 dataset. The corresponding uncertainties are tabulated, along with the alignment uncertainties, in Table 6.8, and are included in the total uncertainty on the final result.

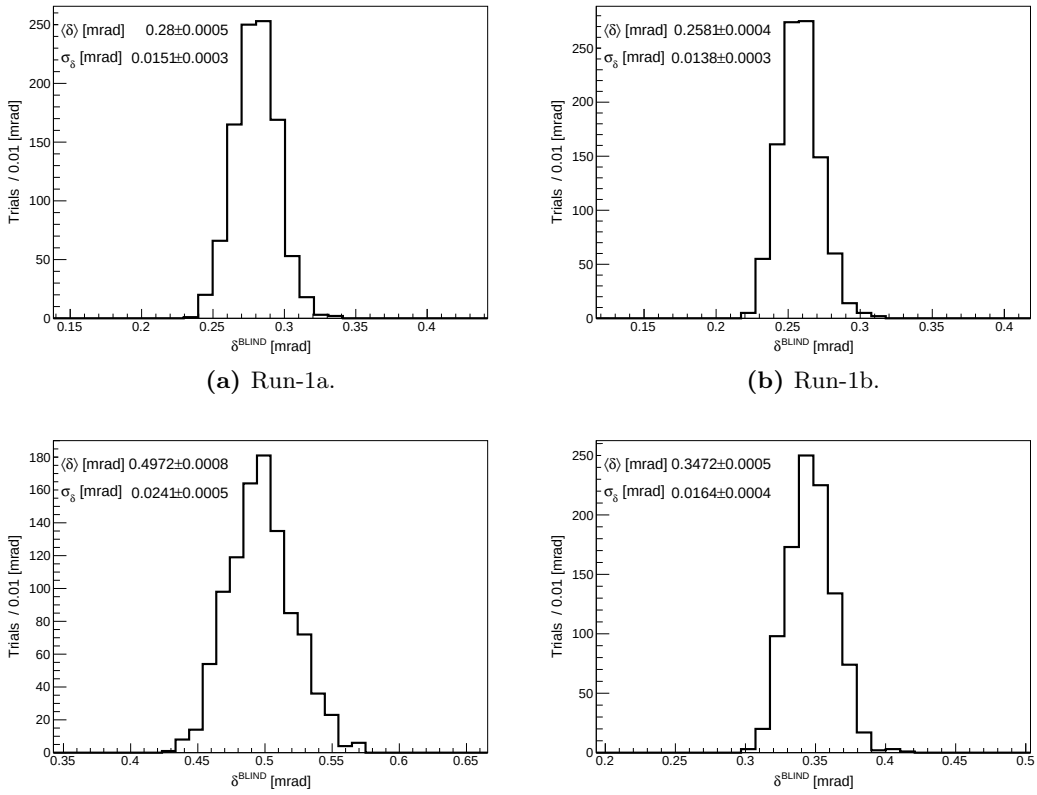

(a) Run-1a. **(b)** Run-1b.

(c) Run-1c. **(d)** Run-1d.

Figure 6.19: The distributions of $\langle \delta^{\mathrm{BLIND}} \rangle$, populated via 1000 trials where the acceptance dilution factor per momentum bin was randomly drawn from a Gaussian distribution with a mean equal to the acceptance factor and a width equal to its statistical uncertainty. The width of these distributions was taken as the contribution to the uncertainty on δ^{BLIND} arising from the statistical uncertainty associated with the simulation dataset used to determine said acceptance factors.

3.8 The radial magnetic field

The uncertainties associated with the radial magnetic field per Run-1 dataset are discussed at length in Chapter 4 and summarised in Table 4.2. These uncertainties are reproduced in units of mrad and e·cm in Table 6.8, presenting a small contribution to the total uncertainty.

3.9 Table of uncertainties

A full summarisation of all uncertainties contributing to the final result is given in Table 6.8, where the dominant uncertainties are statistical. The uncertainties associated with tracker acceptance and alignment preliminary.

		Run-1a		Run-1b		Run-1c		Run-1d	
		δ [mrad]	d_μ [$\times 10^{-19}$ e·cm]	δ [mrad]	d_μ [$\times 10^{-19}$ e·cm]	δ [mrad]	d_μ [$\times 10^{-19}$ e·cm]	δ [mrad]	d_μ [$\times 10^{-19}$ e·cm]
Station 12	Statistical	0.0996	3.18	0.0851	2.72	0.0698	2.23	0.0613	1.96
	Acceptance	0.0292	0.931	0.0159	0.507	0.0322	1.03	0.0223	0.712
	Alignment	0.0240	0.768	0.0120	0.382	0.0274	0.874	0.0182	0.580
	Radial magnetic field	0.00730	0.233	0.00817	0.261	0.00824	0.263	0.00915	0.292
	Total	0.107	3.41	0.0878	2.80	0.0820	2.62	0.0683	2.18
Station 18	Statistical	0.120	3.83	0.102	3.27	0.0849	2.71	0.0745	2.38
	Acceptance	0.0220	0.701	0.0236	0.753	0.0343	1.10	0.0270	0.863
	Alignment	0.00654	0.209	0.000792	0.0253	0.0140	0.445	0.0218	0.697
	Radial magnetic field	0.00730	0.233	0.00817	0.261	0.00824	0.263	0.00915	0.292
	Total	0.122	3.90	0.105	3.37	0.0930	2.97	0.0827	2.64
Combined	Statistical	0.0774	2.47	0.0662	2.11	0.0545	1.74	0.0479	1.53
	Acceptance	0.0151	0.481	0.0138	0.440	0.0241	0.769	0.0164	0.524
	Alignment	0.0137	0.436	0.00762	0.243	0.02351	0.750	0.0203	0.649
	Radial magnetic field	0.00730	0.233	0.00817	0.261	0.00824	0.263	0.00915	0.292
	Total	0.0804	2.57	0.0685	2.19	0.0646	2.06	0.0553	1.76

Table 6.8: A preliminary table of uncertainties contributing to the main result, shown in Figure 6.20.

4 Results

Finally, the contribution to the precession plane tilt angle from the radial magnetic field was subtracted from the $\langle \delta^{\mathrm{BLIND}} \rangle$ results, summarised in Table 6.4, which were then converted into a blind EDM signal, d_μ^{BLIND}, in units of e·cm by Equation 2.29. The results are presented in Figure 6.20, where a zeroth order polynomial fit to the combined results, shown by a grey line, is used to estimate the uncertainty weighted average. The grey dashed lines indicate a 1σ band about the fit, giving a preliminary estimation of the combined uncertainty on the Run-1 EDM analysis, which is

$$\delta\langle d_\mu^{\mathrm{BLIND}} \rangle = 1.04 \times 10^{-19}\, e \cdot \mathrm{cm}.$$

By taking this uncertainty, and considering the scenario whereby the central value is found to be exactly equal to zero following the removal of the blind offset, the expected muon EDM upper limit in E989 Run-1 may be estimated. This was accomplished by assuming a Gaussian probability density function about the central value (assumed to be zero), with a width equal to the combined uncertainty, and integrating symmetrically

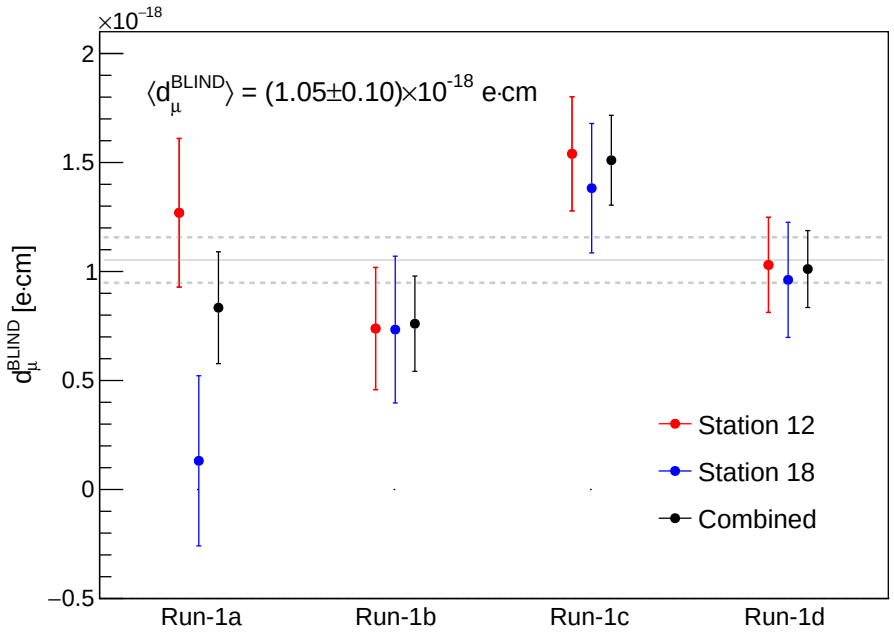

Figure 6.20: Blinded results for the Run-1 tracker EDM analysis. The 1σ band about a zeroth order polynomial fit to the combined results is taken as the estimated total uncertainty, which is used to calculate the expected muon EDM upper limit.

outwards from that central value until 95% of the distribution is covered. This gives an upper limit on the muon EDM of

$$|d_\mu| < 2.0 \times 10^{-19}\, e \cdot \text{cm (95\% C.L.)},$$

which constitutes an improvement on the upper limit from the equivalent traceback detector analysis at BNL, of $|d_\mu| < 3.2 \times 10^{-19}\, e \cdot \text{cm}$ (95% C.L.) [4], by a factor of 1.6.

When comparing the relative statistical power of the BNL traceback analysis and the Fermilab Run-1 tracker analysis, with 9.8 million and 64.1 million track decay vertices incorporated into each respectively, the preliminary upper limit reported in this thesis appears to underperform slightly. That is, based on simple $\sqrt{N}$ scaling, N being the number of decay vertices, the Fermilab Run-1 upper limit might be expected to be stronger than that reported by BNL by a factor of ∼2.6. However, the statistical uncertainty associated with these analyses scales according to $\sigma_{\theta_y}/\sqrt{N}$, where σ_{θ_y} is the width of the vertical decay angle distribution. In Run-1 at Fermilab, σ_{θ_y} has been measured to be ∼13.6 mrad, as shown in Figure 6.3 and Table 6.1, while the exact value of σ_{θ_y} at BNL, after analysis cuts, was not reported: making a direct comparison between BNL and Fermilab difficult in this context. Studies to investigate this matter further using toy Monte Carlo are ongoing [89].

5 Summary and outlook

A blinded search for the muon EDM in E989 Run-1 has been presented, culminating in the estimation of an expected muon EDM upper limit at 95% C.L. which improves upon that from the equivalent analysis performed at the BNL $g-2$ experiment. An assessment of potential sources of systematic uncertainty was outlined, including unique contributions resulting from the non-typical beam conditions in Run-1, which were a consequence of damaged hardware.

The uncertainties associated with tracker acceptance, and by extension tracker global alignment, are preliminary. As discussed in Chapter 5, these uncertainties are expected to decrease as a greater number of events are folded into the Monte Carlo dataset used to derive the acceptance correction. Moving forward, the global tracker tilt angle will also be included in the estimation of the alignment uncertainty. Additionally, the variation in the dependence of the average vertical angle on momentum between Run-1

datasets, which differs from simulation – a consequence of the aforementioned unique beam conditions in Run-1 – will necessitate a modification to the acceptance correction uncertainty. These improvements will be incorporated as the analysis progresses towards unblinding.

Chapter 7

Conclusion

The Fermilab Muon $g-2$ experiment (E989) aims to measure the anomalous magnetic moment of the muon, a_μ, to a precision of 140 parts-per-billion (ppb), and conduct a world-leading search for the muon electric dipole moment (EDM), d_μ, where any observation of a non-vanishing muon EDM would indicate a source of CP violation from new physics beyond the Standard Model. This thesis is focused on advancing the latter goal, presenting a blinded search for d_μ in E989 Run-1, which is supported by studies with large-scale Monte Carlo datasets, along with a new determination of one of the key systematic effects which will impact the ultimate sensitivity to d_μ at E989.

In the E989 storage ring, a muon EDM would manifest as a tilt in the muon spin precession plane, resulting in an oscillation in the average vertical angle of decay positrons which may be measured directly by use of straw tracker detectors. A potentially limiting source of systematic uncertainty in this measurement is the presence of a non-zero radial component of the main magnetic field, which, by tilting the spin precession plane in the same manner as a muon EDM, can result in a false signal. This field component must be measured if a precision search for d_μ is to be undertaken. Accordingly, a novel technique was presented in Chapter 4 for measuring the average background radial magnetic field, $\langle B_r^b \rangle$, to a precision of ≤ 1 parts-per-million (ppm), without disturbing the storage ring vacuum or requiring the use of additional hardware. Two measurements were performed by the author in E989 Run-4: the first being preliminary measurement, which was subsequently used to adjust $\langle B_r^b \rangle$ to zero, and the second being a higher precision measurement, whereby $\langle B_r^b \rangle$ was measured to be -0.4 ± 0.6 ppm. Based on this result, a method was designed to estimate the total average radial magnetic field, $\langle B_r \rangle$, in any E989 dataset, where estimates were made for the available subsets of Run-3 and Run-5, as well as the entirety of Run-1 and Run-2. This work ensures that the radial magnetic field systematic does not limit the sensitivity to d_μ at Fermilab, in Run-1 and

beyond. The techniques developed in this chapter have subsequently been utilised, with the assistance of the author, by fellow E989 collaborators to both measure $\langle B_r^b \rangle$ in Run-5 and to continue to estimate $\langle B_r \rangle$ in E989 datasets as they are produced.

The measured vertical angle associated with a muon EDM is reduced (diluted) compared to the true precession plane tilt angle, and the ability to correct this effect is essential to the measurement of d_μ. A thorough assessment of the tilt angle dilution, by use of a large-scale Monte Carlo simulation, was detailed in Chapter 5. The analytical form of the dilution as a function of positron momentum, associated with both the inherent decay asymmetry and relativistic effects, was verified, and the contribution to the dilution from straw tracker acceptance was characterised. Additionally, simulation was used to make a preliminary estimation of the systematic uncertainty associated with detector global vertical position alignment, which will be expanded to incorporate the impact of global detector tilt angle. The uncertainties associated with acceptance are expected to diminish as a greater number of events are folded into the Monte Carlo dataset used to derive the acceptance correction. Additional studies on the impact of the non-typical beam conditions in Run-1 on acceptance will also be included as the analysis progresses towards an unblinding.

Finally, a blinded search for the muon EDM in E989 Run-1 was presented in Chapter 6, where the primary analysis was performed in momentum intervals in order to maximise the accuracy of the dilution correction, and to minimise momentum dependent variations in the average vertical decay angle. An assessment of potential sources of systematic uncertainty in the analysis was also outlined in that chapter, including a description of the corrections necessitated by the aforementioned unique beam conditions in Run-1. A preliminary combined blind result for Run-1 was presented, with an estimated total uncertainty of $1.04 \times 10^{-19}\, e \cdot \text{cm}$. This uncertainty was used to estimate an expected upper limit on the muon EDM of $|d_\mu| < 2.0 \times 10^{-19}\, e \cdot \text{cm}$ (95% C.L.), which improves upon the upper limit from the equivalent traceback analysis performed at BNL [4].

The author will remain closely involved in the Run-1 muon EDM search until an agreement to remove the blind offset and move to publish the result is reached. More broadly, the work presented in this thesis lays the foundations for the greater muon EDM search across the E989 integrated dataset, which will ultimately result in either a world-leading upper limit on the muon EDM, or the discovery of new physics outright.

Bibliography

[1] B. Abi et al. Measurement of the positive muon anomalous magnetic moment to 0.46 ppm. *Phys. Rev. Lett.*, 126:141801, Apr 2021.

[2] G. W. Bennett et al. Final report of the E821 muon anomalous magnetic moment measurement at BNL. *Phys. Rev. D*, 73:072003, Apr 2006.

[3] T. Aoyama et al. The anomalous magnetic moment of the muon in the Standard Model. *Physics Reports*, 887:1–166, Dec 2020.

[4] G. W. Bennett et al. Improved limit on the muon electric dipole moment. *Phys. Rev. D*, 80:052008, Sep 2009.

[5] V. Andreev et al. Improved limit on the electric dipole moment of the electron. *Nature*, 562(7727):355–360, Oct 2018.

[6] J. D. Jackson. *Classical electrodynamics*. Wiley, 3rd ed edition, 1999.

[7] B. L. Roberts and W. J. Marciano. *Lepton Dipole Moments*. WORLD SCIENTIFIC, 2009.

[8] P. Kusch and H. M. Foley. Precision measurement of the ratio of the atomic 'g values' in the ${}^2p_{\frac{3}{2}}$ and ${}^2p_{\frac{1}{2}}$ states of gallium. *Phys. Rev.*, 72:1256–1257, Dec 1947.

[9] J. Schwinger. On quantum-electrodynamics and the magnetic moment of the electron. *Phys. Rev.*, 73:416–417, Feb 1948.

[10] T. Aoyama, T. Kinoshita, and M. Nio. Revised and improved value of the qed tenth-order electron anomalous magnetic moment. *Phys. Rev. D*, 97:036001, Feb 2018.

[11] D. Hanneke, S. F. Hoogerheide, and G. Gabrielse. Cavity control of a single-electron quantum cyclotron: Measuring the electron magnetic moment. *Phys. Rev. A*, 83:052122, May 2011.

[12] A. Czarnecki and W. J. Marciano. Muon anomalous magnetic moment: A harbinger for "new physics". *Phys. Rev. D*, 64:013014, Jun 2001.

[13] A. D. Sakharov. Violation of CP Invariance, C asymmetry, and baryon asymmetry of the universe. *Pisma Zh. Eksp. Teor. Fiz.*, 5:32–35, 1967.

[14] E. M. Purcell and N. F. Ramsey. On the possibility of electric dipole moments for elementary particles and nuclei. *Phys. Rev.*, 78:807–807, Jun 1950.

[15] T. E. Chupp, P. Fierlinger, P. M. J. Ramsey-Musolf, and J. T. Singh. Electric dipole moments of atoms, molecules, nuclei, and particles. *Rev. Mod. Phys.*, 91:015001, Jan 2019.

[16] B. Graner, Y. Chen, E. G. Lindahl, and B. R. Heckel. Reduced limit on the permanent electric dipole moment of ^{199}Hg. *Phys. Rev. Lett.*, 116:161601, Apr 2016.

[17] C. Seng. Reexamination of the standard model nucleon electric dipole moment. *Phys. Rev. C*, 91:025502, Feb 2015.

[18] Ng, D. and Ng, J. N. A note on Majorana neutrinos, leptonic CKM and electron electric dipole moment. *Modern Physics Letters A*, 11(03):211–216, 1996.

[19] R. Chivukula, H. Georgi, and L. Randall. A composite technicolor standard model of quarks. *Nuclear Physics B*, 292:93–108, 1987.

[20] R. Aaij et at. Test of lepton universality in beauty-quark decays, 2021.

[21] A. Crivellin, M. Hoferichter, and P. Schmidt-Wellenburg. Combined explanations of $(g-2)_{\mu,e}$ and implications for a large muon EDM. *Phys. Rev. D*, 98(11), dec 2018.

[22] A. Crivellin and M. Hoferichter. Combined explanations of $(g-2)_\mu$, $(g-2)_e$ and implications for a large muon EDM. 2019.

[23] M, Sakurai et al. muEDM: Towards a search for the muon electric dipole moment at PSI using the frozen-spin technique. 01 2022.

[24] P. Athron. et al. New physics explanations of a_μ in light of the FNAL muon $g-2$ measurement. *Journal of High Energy Physics*, 2021(9), sep 2021.

[25] T. D. Lee and C. N. Yang. Question of parity conservation in weak interactions. *Phys. Rev.*, 104:254–258, Oct 1956.

[26] C. S. Wu, E. Ambler, R. W. Hayward, D. D. Hoppes, and R. P. Hudson. Experimental test of parity conservation in beta decay. *Phys. Rev.*, 105:1413–1415, Feb 1957.

[27] M. Tanabashi et al. Review of particle physics. *Phys. Rev. D*, 98:030001, Aug 2018.

[28] L. H. Thomas. The motion of the spinning electron. *Nature*, 117(2945):514–514, Apr 1926.

[29] T. Albahri et. al. Measurement of the anomalous precession frequency of the muon in the Fermilab Muon $g-2$ Experiment. *Phys. Rev. D*, 103:072002, Apr 2021.

[30] T. Albahri et al. Beam dynamics corrections to the Run-1 measurement of the muon anomalous magnetic moment at Fermilab. *Phys. Rev. Accel. Beams*, 24:044002, Apr 2021.

[31] Bennett, G. W. et al. Statistical equations and methods applied to the precision muon $(g-2)$ experiment at BNL. *Nucl. Instrum. Meth. A*, 579:1096–1116, 2007.

[32] J. P. Miller, E. de Rafael, and B. L. Roberts. Muon $(g-2)$: experiment and theory. *Reports on Progress in Physics*, 70(5):R03, may 2007.

[33] T. Albahri et al. Magnetic-field measurement and analysis for the muon $g-2$ experiment at fermilab. *Phys. Rev. A*, 103:042208, Apr 2021.

[34] E. Tiesinga, P. Mohr, D. B. Newell, and B. Taylor. Codata recommended values of the fundamental physical constants: 2018. *Rev. Mod. Phys.*, 93:025010, Jun 2021.

[35] R. Chislett. Internal communication, 2020.

[36] P. Debevec. E989 Note 271: Analytic expressions for $g-2$ and EDM asymmetry and figure-of-merit, 2021. DocDB-25851.

[37] J. Price. E989 note 285: Vertical angle for EDM, 2022. DocDB-26584.

[38] B. L. Roberts. The History of the Muon $(g-2)$ Experiments. *SciPost Phys. Proc.*, page 32, 2019.

[39] J. Grange et. al. Muon ($g-2$) Technical Design Report, 2015.

[40] D. Stratakis et al. Accelerator performance analysis of the Fermilab Muon Campus. *Phys. Rev. Accel. Beams*, 20:111003, Nov 2017.

[41] N. Froemming et al. Commissioning the superconducting magnetic inflector system for the Muon $g-2$ experiment.

[42] A. P. Schreckenberger et al. The fast non-ferric kicker system for the Muon $g-2$ experiment at Fermilab. *Nuclear Instruments and Methods in Physics Research Section A: Accelerators, Spectrometers, Detectors and Associated Equipment*, 1011:165597, 2021.

[43] A. P. Schreckenberger. Internal communication, 2022.

[44] On Kim et. al. Reduction of coherent betatron oscillations in a muon $g-2$ storage ring experiment using RF fields. *New Journal of Physics*, 22(6):063002, jun 2020.

[45] C. E. Shannon. Communication in the presence of noise. *Proceedings of the IRE*, 37(1):10–21, jan 1949.

[46] J. Grange. E989 Note 57: Shift in ω_p due to couplings between longitudinal and transverse magnetic field inhomogeneities (distortion of the closed orbit analysis update, 2015.

[47] G. T. Danby et al. The Brookhaven muon storage ring magnet. *Nucl. Instrum. Meth. A*, 457:151–174, 2001.

[48] D. A. Sweigart. *A Measurement of the Anomalous Precession Frequency of the Positive Muon.* PhD thesis, Cornell U., 2020.

[49] M. Smith. *Developing the precision magnetic field for the E989 Muon $g-2$ experiment.* PhD thesis, University of Washington, 2017.

[50] J. George. The new Muon $g-2$ experiment at Fermilab, 2018. E989 DocDB-12212.

[51] H. Binney. T0 update, 2018. E989 DocDB-10162.

[52] B. MacCoy. IBMS update, 2018. E989 DocDB-10944.

[53] F. Gray. Fiber harp poster for open house, 2017. E989 DocDB-8366.

[54] J. Kaspar. Calorimeter construction update, 2016. E989 DocDB-4661.

[55] J. Hempstead. *Measuring the anomalous precession frequency ω_a for the Muon $g-2$ experiment*. PhD thesis, University of Washington, 2021.

[56] S. Grant. E989 Note 234: Independent energy calibration cross-checks with the straw trackers for Run-1, 2020. DocDB-23345.

[57] S. Charity. *Beam profile measurements using the straw tracking detectors at the Fermilab muon $g-2$ experiment, and a study of their sensitivity to a muon electric dipole moment*. PhD thesis, University of Liverpool, 2018.

[58] B. T. King et al. The straw tracking detector for the Fermilab Muon $g-2$ Experiment. *Journal of Instrumentation*, 17(02):P02035, Feb 2022.

[59] V. Innocente, M. Maire, and E. Nagy. GEANE: Average tracking and error propagation package. In *Workshop on Detector and Event Simulation in High-energy Physics (MC '91)*, pages 58–78, 1991.

[60] N. B. Kinnaird. *Muon spin precession frequency extraction and decay positron track fitting in Run 1 of the Fermilab Muon $g-2$ experiment*. PhD thesis, Boston University, 2020.

[61] C. Runge. Ueber die numerische auflösung von differentialgleichungen. *Mathematische Annalen*, 46(2):167–178, Jun 1895.

[62] J. Mott. Track quality cut service, 2019. E989 DocDB-16444.

[63] R. Fatemi et at. Data production for Muon $g-2$, 2016. E989 DocDB-4638.

[64] S. Ritt and P. Amaudruz. New components of the MIDAS data acquisition system. *1999 IEEE Conference on Real-Time Computer Applications in Nuclear Particle and Plasma Physics.*, pages 116–118, 1999.

[65] R. Brun and F. Rademakers. ROOT: An object oriented data analysis framework. *Nucl. Instrum. Meth. A*, 389:81–86, 1997.

[66] R. A. Illingworth. A data handling system for modern and future Fermilab experiments. *Journal of Physics: Conference Series*, 513(3):032045, jun 2014.

[67] K. Chadwick et al. FermiGrid—experience and future plans. *Journal of Physics: Conference Series*, 119(5):052010, jul 2008.

[68] R. Pordes et al. The open science grid status and architecture. *Journal of Physics: Conference Series*, 119(5):052028, jul 2008.

[69] S. Agostinelli et al. GEANT4–a simulation toolkit. *Nucl. Instrum. Meth. A*, 506:250–303, 2003.

[70] C. Green et al. The art framework. *Journal of Physics: Conference Series*, 396(2):022020, dec 2012.

[71] K. Kim Siang. Muon $g-2$ reconstruction and analysis framework for the muon anomalous precession frequency. *Journal of Physics. Conference Series*, 1085(3), 9 2018.

[72] D. Vasilkova. EDM analysis update, 2021. E989 DocDB-25666.

[73] B. Morse. : Setting $\langle B_r \rangle$ to zero, 2020. E989 DocDB-23522.

[74] D. Tarazona. Internal communication, 2021.

[75] A. Fienberg. *Measuring the precession frequency in the E989 Muon g–2 Experiment.* PhD thesis, University of Washington.

[76] E. Barlas-Yucel. Internal communication, 2022.

[77] S. Corrodi. Radial field from surface coils, 2021. E989 DocDB-24596.

[78] J. R. Taylor. *An Introduction to Error Analysis: The Study of Uncertainties in Physical Measurements.* University Science Books, 1996.

[79] H. Binney. What is a CTAG?, 2019. E989 DocDB-19916.

[80] P. Winter and A. Tewsley-Booth. Elog entry: Radial field scan, 2019.

[81] E. Barlas-Yucel. Internal communication, 2020.

[82] S. Grant. Elog entry: Radial field scan (run-4): first results, 2020.

[83] S. Grant. Elog entry: Detailed radial field scan (run-4): first results, 2020.

[84] D. Vasilkova. Internal communication, 2022.

[85] G. Lukicov. *Alignment of the straw tracking detectors for the Fermilab Muon $g-2$ experiment and systematic studies for a muon electric dipole moment measurement.* PhD thesis, University College London, 2020.

[86] J. Price. Global Alignment of Trackers – Uncertainty, 2019. E989 DocDB-16925.

[87] M. Matsumoto and T. Nishimura. Mersenne Twister: A 623-dimensionally equidistributed uniform pseudo-random number generator. 8(1), 1998.

[88] J. Mott. Beam Measurements: Run 1, 2020. E989 DocDB-22002.

[89] J. Price. EDM: update and projected sensitivity, 2022. E989 DocDB-27468.

Appendices

Appendix A

Derivation for the change in a_μ from a muon EDM

To reiterate the discussion given in Chapter 2 Section 3.2, a non-zero muon EDM increases the anomalous spin precession frequency to a give a total of $\omega_{a\eta}$, as defined by Equation 2.30, which may be alternatively expressed as

$$\omega_{a\eta} = \omega_a \sqrt{1 + \tan^2 \delta^*}, \tag{A.1}$$

where δ^* is the precession plane tilt angle in the muon rest frame. As discussed, this means that a non-zero muon EDM could account for the observed deviation in a_μ, where the value of d_μ required may be estimated by equating the necessary fractional increase in spin precession frequency to the fractional deviation in a_μ, by

$$\begin{aligned} &\frac{\Delta\omega_a}{\omega_a} = \frac{\Delta a_\mu}{a_\mu^{\mathrm{SM}}} \\ \rightarrow &\frac{\omega_{a\eta} - \omega_a}{\omega_a} = \frac{a_\mu^{\mathrm{Exp}} - a_\mu^{\mathrm{SM}}}{a_\mu^{\mathrm{SM}}} \\ \rightarrow &\frac{\omega_{a\eta}}{\omega_a} - 1 = \frac{a_\mu^{\mathrm{Exp}}}{a_\mu^{\mathrm{SM}}} - 1. \end{aligned} \tag{A.2}$$

ω_a in this case is the value that would be expected from the SM prediction of a_μ. From Equation A.1, and following from a similar calculation given by S. Charity in [57], the

fraction $\omega_{a\eta}/\omega_a$ may be written as

$$\begin{aligned}\frac{\omega_{a\eta}}{\omega_a} &= \sqrt{1+\delta^{*2}} \\ &\approx 1+\frac{\delta^{*2}}{2} \\ &= 1+\left(\frac{\eta\beta}{\sqrt{8}a_\mu^{\mathrm{Exp}}}\right)^2 .\end{aligned} \tag{A.3}$$

Substituting $\eta = 4d_\mu m_\mu c/\hbar e$, from Equation 1.9, gives

$$\frac{\omega_{a\eta}}{\omega_a} - 1 = \left(\frac{\sqrt{2}d_\mu m_\mu c\beta}{\hbar e a_\mu^{\mathrm{Exp}}}\right)^2 , \tag{A.4}$$

where the left-hand-side is equivalent to $\Delta a_\mu/a_\mu^{\mathrm{SM}}$, as follows from Equation A.2, meaning that Equation A.4 may be rearranged for d_μ to obtain

$$d_\mu = \sqrt{\Delta a_\mu}\cdot\frac{a_\mu^{\mathrm{Exp}}}{\sqrt{a_\mu^{\mathrm{SM}}}}\cdot\frac{\hbar e}{\sqrt{2}m_\mu c\beta}, \tag{A.5}$$

as given by Equation 2.31.

Appendix B

The maximum vertical decay angle

A contributing factor to the momentum dependent dilution of the tilt angle is the contraction of the vertical decay angle, which arises from the Lorentz transformation into the laboratory frame. Here, an expression for the variation of the maximum vertical decay angle as a function of momentum, $\theta_y^{\max}(p)$, is derived. Rest frame quantities are indicated by asterisks.

If the Lorentz boost is directed along the z-axis (the longitudinal axis), then the energy-momentum four vector components of the decay positron transform by

$$E = \gamma E^* - \beta\gamma p_z^*, \tag{B.1}$$

$$p_z = -\beta\gamma E^* + \gamma p_z^*, \tag{B.2}$$

$$p_T = p_T^*, \tag{B.3}$$

where p_T is the transverse component of momentum, which may be expressed in terms of E^* and p_z^*, so that

$$p_T = p_T^* = \sqrt{E^{*2} - p_z^{*2}}. \tag{B.4}$$

To maximise the vertical angle, the rest frame energy of the muon must also be maximised, so that $E^* = m_\mu/2$ where m_μ is the muon mass. In this case, and in the limit $\beta \to 1$, p_z^* may be rewritten as

$$p_z^* = \frac{m_\mu}{2} - \frac{p_z}{\gamma}. \tag{B.5}$$

The above expression may be substituted into Equation B.4 to give an expression for p_T in terms of p_z, so that

$$p_T = \sqrt{\frac{m_\mu p_z}{\gamma} - \left(\frac{p_z}{\gamma}\right)^2}. \tag{B.6}$$

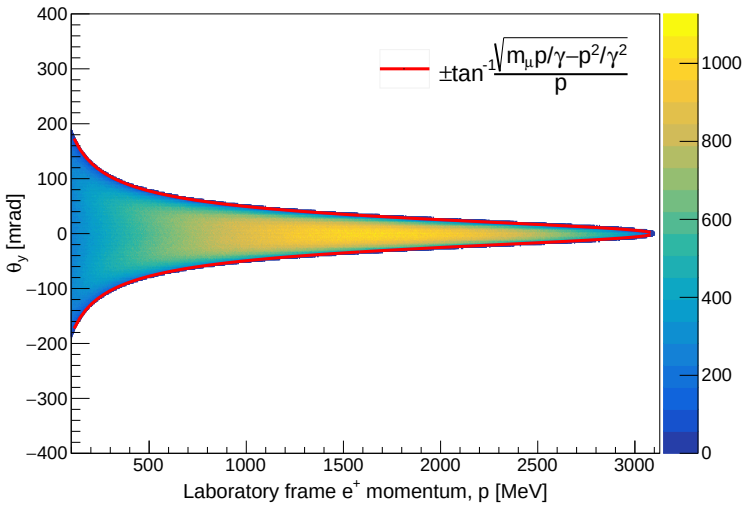

Figure B.1: The distribution of laboratory frame vertical angles against momentum, from a simulation sample with complete acceptance and no detector effects. Equation B.8 is overlaid ($\pm\theta_y$), showing good agreement with the maximum angles.

Now, given that the θ_y may alternatively be defined as

$$\theta_y = \tan^{-1}\left(\frac{p_T}{p_z}\right), \tag{B.7}$$

and making the assumption that $p = p_z$ in the laboratory frame, then the maximum vertical angle as function of momentum is described by

$$\theta_y^{\max}(p) = \tan^{-1}\left(\frac{\sqrt{m_\mu p/\gamma - (p/\gamma)^2}}{p}\right). \tag{B.8}$$

This function is represented in Figure B.1, showing good agreement with the maximum angles in the distribution of θ_y against momentum from the *all decays* (100% detector acceptance) simulation dataset, detailed in Chapter 5.

Appendix C

Propagation of errors

In this appendix, non-trivial expressions for the uncertainties of certain parameters will be derived, utilising the standard formulae for the propagation of errors, which may be found in [78]. For a quantity z, comprised of uncorrelated parameters x and y, the corresponding uncertainty δz is

$$\delta z = \sqrt{\left(\frac{\partial z}{\partial x}\right)^2 \delta x^2 + \left(\frac{\partial k}{\partial y}\right)^2 \delta y^2}. \tag{C.1}$$

If x and y are correlated, then δz is given by

$$\delta z^2 = \sqrt{\left(\frac{\partial z}{\partial x}\right)^2 \delta x^2 + \left(\frac{\partial k}{\partial y}\right)^2 \delta y^2 + 2\frac{\partial z}{\partial x}\frac{\partial z}{\partial y}\sigma_{xy}}, \tag{C.2}$$

where σ_{xy} is the covariance of x and y, defined as

$$\sigma_{xy} = \frac{1}{N}\sum_{i=1}^{N}(x_i - \langle x\rangle)(y_i - \langle y\rangle). \tag{C.3}$$

1 The background radial field uncertainty, $\delta\langle B_r^b\rangle$

The average background radial field, $\langle B_r^b\rangle$, is derived from a straight line fit of the form

$$\Delta\langle y\rangle \cdot \Delta V = m \cdot \langle B_r^a\rangle + c, \tag{C.4}$$

where an example of such a fit is shown in Figure 4.10b. $\langle B_r^b\rangle$ is found at the opposite sign of the x-intercept of the fit, where $\Delta\langle y\rangle \cdot \Delta V = 0$, so that

$$\langle B_r^b\rangle = \frac{c}{m}. \tag{C.5}$$

Given that the parameters m and c are correlated, Equation C.2 gives the uncertainty

$$\delta\langle B_r^b\rangle^2 = \left(-\frac{c}{m^2}\right)^2 \delta m^2 + \left(\frac{1}{m}\right)^2 \delta c^2 + 2\left(\frac{1}{m}\right)\left(-\frac{c}{m^2}\right)\sigma_{mc}. \tag{C.6}$$

Factoring out $\langle B_r^b\rangle^2$ and simplifying, gives

$$\delta\langle B_r^b\rangle = \langle B_r^b\rangle\sqrt{\left(\frac{\delta m}{m}\right)^2 + \left(\frac{\delta c}{c}\right)^2 - \frac{2}{mc}\sigma_{mc}}, \tag{C.7}$$

as given by Equation 4.10 in the text.

2 The radial field conversion factor uncertainty, δk

The constant k, required to convert between $\Delta\langle y\rangle$ and $\Delta\langle B_r\rangle$, is given by

$$k = \frac{1}{\frac{m}{V} + c}, \tag{C.8}$$

which is reproduced from Equation 4.16. Given that the fit parameters m and c have some correlation, the uncertainty associated with k follows from Equation C.2, giving

$$\begin{aligned}\delta k^2 = &\left(-\frac{1}{V}\cdot\frac{1}{(\frac{m}{V}+c)^2}\right)^2 \delta m^2 \\ &+ \left(-\frac{1}{(\frac{m}{V}+c)^2}\right)^2 \delta c^2 + \\ &+ 2\left(-\frac{1}{V}\cdot\frac{1}{(\frac{m}{V}+c)^2}\right)\left(-\frac{1}{(\frac{m}{V}+c)^2}\right)\sigma_{mc},\end{aligned} \tag{C.9}$$

which may to simplified to

$$\delta k = \sqrt{\left(\frac{1}{Vk^2}\right)^2 \cdot \delta m^2 + \left(\frac{1}{k^4}\right)\cdot\delta c^2 + \left(\frac{2}{Vk^4}\right)\cdot\sigma_{mc}}, \tag{C.10}$$

as given by Equation 4.3 in the text.

3 The up/down asymmetry uncertainty, δA

The EDM decay asymmetry, defined in terms of the numbers of simulated 'up' and 'down' decays, N_u and N_d, as detailed in Chapter 5 Section 2, is defined as

$$A = \frac{N_u - N_d}{N_u + N_d}, \tag{C.11}$$

by Equation 5.1. Since N_u and N_d are uncorrelated, Equation C.1 may be applied to determine the corresponding uncertainty, δA, so that

$$\delta A^2 = \left(\frac{2N_d}{(N_u + N_d)^2}\right)^2 \delta N_u^2 + \left(-\frac{2N_u}{(N_u + N_d)^2}\right)^2 \delta N_d^2. \tag{C.12}$$

Given that the statistical uncertainties, δN_u and δN_d, are estimated by taking the square root of the central value, so that

$$\delta N_u = \sqrt{N_u}, \tag{C.13}$$

$$\delta N_d = \sqrt{N_d}, \tag{C.14}$$

then Equation C.12 may be simplified to

$$\delta A^2 = \frac{4N_u N_d}{(N_u + N_d)^3} = \frac{1 - A^2}{N_u + N_d}, \tag{C.15}$$

which is equivalent to Equation 5.2.